学位論文

Muon Spin Relaxation Measurements of Singlet Ground-State Materials

〔一重項基底状態物質のミュオンスピン緩和測定〕

小嶋健児

学位論文

Muon Spin Relaxation Measurements of
Singlet Ground-State Materials

〔一重項基底状態物質のミュオンスピン緩和測定〕

平成７年１２月博士（理学）申請

東京大学大学院理学系研究科
物理学専攻

小嶋　健児

論文の内容の要旨

論文題目　一重項基底状態物質のミュオンスピン緩和測定

氏名　小嶋 健児

私は、学位論文のための研究として、スピン梯子物質（$Sr_{n-1}Cu_{n+1}O_{2n}$; n=3, 5）、ハルデン物質（$(Y_{2-x}Ca_x)Ba(Ni_{1-y}Mg_y)O_5$）及び、スピンパイエルス物質（$((Cu_{1-x}Zn_x)(Ge_{1-y}Si_y)O_3$）の、主にミュオンスピン緩和法（$\mu$ S R）による研究をおこなった［1,2,3,4］。これらの系は、反強磁性的相互作用を持つスピン系であるにもかかわらず、特定の格子構造（２本足スピン梯子［5］）や、スピンの値（S＝１；ハルデン系［6］）、格子の周期的歪み（スピンパイエルス系［7］）のために、Neel 的な反強磁性秩序が抑制されて、スピン一重項が基本となった基底状態（一重項基底状態）を持つと考えられている系である（図１）。

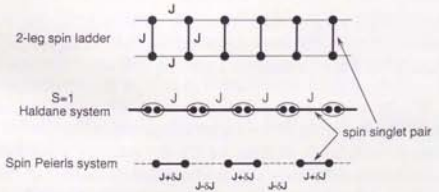

図１：一重項基底状態の概念図。これら３種のスピン系は、スピン一重項対（アレイ型の太線）が基本となった基底状態を持つ。

これら一重項基底状態の一般的な磁気的特徴のひとつとして、「基底状態における内部磁場の欠如」があげられる。この特徴を実験的に検証するためには、スピン緩和を用いた局所磁場プローブ法が有効であるが、μＳＲは、そのような種々の測定手法の中で、微小・希薄なモーメントに対して最も高感度な手法である［8］。さらに、以上の物質に非磁性原子（Mg^{2+}→Ni^{2+}、Zn^{2+}→Cu^{2+}）や正電荷（Ca^{2+}→Y^{3+}）をドープすると一重項基底状態から不対スピンを作り出すことができるが、この博士論文研究では、これらドーピングに伴う不対スピンのダイナミックスをμＳＲ法で調べた。

スピン梯子物質（$Sr_{n+1}Cu_{n+1}O_{2n}$）

この物質は、これまでのところ、梯子の幅を決める Cu 原子の数（‘足’の数）が２と３の物が合成できている（各々 n=3, 5 に対応）［9］。我々は、その両方のμＳＲ測定をおこない、「３本足梯子」は、約５２Ｋでスピンが秩序化する一方、「２本足梯子」は２０ｍＫまで常磁性的にふるまうことを発見した（図２）。理論的には、スピン梯子系の基底状態は、梯子の足の数が偶数の時だけ一重項基底状態であると予想されているため［5］、我々のμＳＲ測定の結果は、この予想を支持している。また、３本足梯子系の秩序温度（５２Ｋ）は、同じ Sr(Ca)-Cu-O からなる二次元正方格子系のネール温度（$Ca_{0.86}Sr_{0.14}CuO_2$：５４０Ｋ）と一次元チェイン系のネール温度（Sr_2CuO_3：５Ｋ）の中間であることが明らかになったが、これは、梯子構造が、二次元と一次元の間の次元性を持つことを反映していると考えられる。これらの結果は、論文［1］にまとめられている。

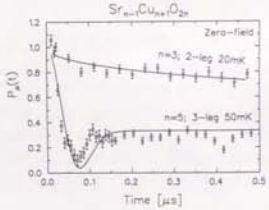

図２：スピン梯子物質のμＳＲスペクトル。「３本足梯子系」$Sr_2Cu_3O_5$ では、スピン秩序化に伴う静的内部磁場が観測されたが、「２本足梯子」$Sr_2Cu_3O_6$ はｍＫ領域まで常磁性的にふるまう。

ハルデン系と非磁性原子／正電荷ドープ（$(Y_{2-x}Ca_x)Ba(Ni_{1-y}Mg_y)O_5$）

ハルデン系とは、Ｓ＝１スピンの一次元チェインで、隣同士のスピンが反強磁性的相互作用を持つ系である。この系の基底状態は、F. D. M. Haldane が最初に指摘したように、多数のスピン一重項からなると考えられている［6］。最近、ハルデン系のモデル物質として、無機物質の Y_2BaNiO_5 が発見された［10］。この系の利点は、非磁性原子（Mg）をスピンサイト（Ni）にドープして、チェインを切ることのできる点と、Y^{3+} サイトに Ca^{2+} をドープして、系に正電荷をドープできる点である。我々は、まず、何もドープしていない系のμＳＲ測定をおこない、１００ｍＫまで、磁気秩序が現れないことを確かめた。この結果は、非磁性的基底状態の予想を支持している。また、非磁性原子（Mg）をドープして、チェインを切った系 $Y_2Ba(Ni_{1-y}Mg_y)O_5$ も、２０ｍＫまで磁気秩序を示さず、一重項基底状態を保つらしいことが明らかになった（図３）。

正電荷をドープしたハルデン物質 $(Y_{2-x}Ca_x)BaNiO_5$ では、帯磁率にスピングラス的カスプと冷却過程による履歴が現れる（図３）。我々は、μＳＲで、このカスプ温度以下のスピン揺らぎを調べ、その結果、ｍＫ温度領域まで、奇妙なスピン揺らぎが残ることが明らかになった。このスピン揺らぎによるミュオンスピン緩和関数は、従来の久保－鳥谷部理論では説明の付かない磁場依存性を示し、この系のスピン揺らぎが、従来仮定されているマルコフ過程からほど遠いことを示唆している。同様の奇妙なスピン揺らぎは、フラストレートしたカゴメ格子系（$SrCr_8Ga_4O_{19}$）のμＳＲでも観測されており［11］、両者の基底状態の類似性が注目される。これらの結果の大部分は、論文［2,3］にまとめられている。

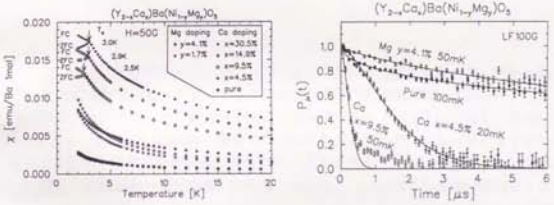

図３：ハルデン物質の帯磁率とμＳＲスペクトル。純な系と非磁性原子ドープした系は非磁性基底状態を保つが、正電荷ドープした系は、帯磁率のスピングラス的カスプに対応して、ミュオンスピン緩和がはやくなる。

スピンパイエルス系と非磁性原子ドープ（$((Cu_{1-x}Zn_x)(Ge_{1-y}Si_y)O_3$）

スピンパイエルス系とは、Ｓ＝1/2 一次元スピンチェインで、スピン－格子結合のため、有限温度 T_{SP} 以下で、格子が二倍周期に歪み、それと同時にスピン一重項対が、互いに近づいたスピン間で形成される系である。近年、$CuGeO_3$ という無機モデル物質が発見され［12］、スピンサイト（Zn^{2+}→Cu^{2+}）や、側鎖（Si→Ge）へのドーピングの影響が調べられるようになった。この博士論文研究では、まず、$CuGeO_3$ が非磁性基底状態を持つことを、μＳＲで２０ｍＫまで確認した。さらに、側鎖にドープした系（$Cu(Ge_{1-y}Si_y)O_3$; y=0.02）では、内部磁場によるミュオンスピンの Larmor 歳差運動が観測され、Cu スピンの Neel 秩序を支持する結果となった。スピンサイトに Zn をドープした系（$(Cu_{1-x}Zn_x)GeO_3$）では、Zn 濃度揺らぎに伴う内部磁場のマクロスコピックな分布のため、ミュオンスピンの Larmor 回転は観測できなかったが、Neel 温度以下で静的な内部磁場によるミュオンスピン緩和が観測された。その緩和率は、Neel 温度 T_N を最高にする Zn 濃度（x～0.04）で最大値を取ることが明らかになり、‘Zn オーバードープ領域’（x>0.04；［12］）では秩序化するモーメントの長さが縮

むことが示唆された。

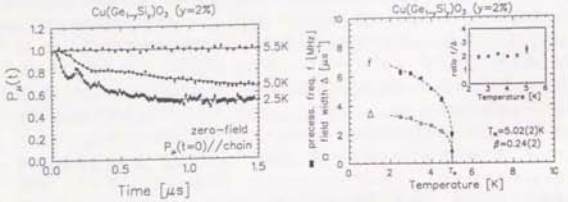

図4：側鎖にSi ドープしたスピンパイエルス物質の零磁場μSRスペクトルと内部磁場の温度変化。Cu モーメントの Neel 秩序による、ミュオンスピン回転が観測された。温度変化の図中の破線はべき則 $\sim(T_c-T)^{\beta}$ による解析。

まとめ

本博士論文研究でのμSR測定によって、上記3種の一重項基底状態物質（$Sr_2Cu_3O_5$、Y_2BaNiO_5 及び、$CuGeO_3$）は、非磁性の基底状態を実現していることが明らかになった。これらの系はみな、常磁性的でゆっくりしたミュオン緩和を引き起こす。ところが、非磁性原子をスピンサイトにドープした場合の応答は、ハルデン物質（$Y_2Ba(Ni_{1-y}Mg_y)O_5$）とスピンパイエルス物質（$(Cu_{1-y}Zn_y)GeO_3$）で、定性的に異なる。前者は非磁性基底状態を保つ一方、後者はモーメントの静的秩序化を示した。この応答の違いは、基底状態の構造の違い（図1）を反映しているのかもしれない。

本博士論文研究を通じて、最も新しい現象は、正電荷ドープしたハルデン物質（$(Y_{2-x}Ca_x)BaNiO_5$）で観測された、奇妙なスピン揺らぎである。このスピン揺らぎは、mK領域でも残る上、通常のマルコフ過程に基づくスピン緩和理論では説明できず、その理解は、将来の課題として残されている。

参考文献

[1] K. Kojima *et al*, Phys. Rev. Lett. 74 (1995) 2812.

[2] K. Kojima *et al*, Phys. Rev. Lett. 74 (1995) 3471.

[3] K. Kojima *et al*, J. of Mag. Mag. Matrs. 140-144 (1995) 1657 (ICM94 proceedings).

[4] K. Kojima *et al*, unpublished.

[5] T. M. Rice *et al*, Europhys. Lett. 23 (1993) 445;
S. Gopalan *et al*, Phys. Rev. B49 (1994) 8901.

[6] F. D. M. Haldane, Phys. Lett. 93A (1983) 464; Phys. Rev. Lett. 50 (1983) 1153.

[7] H. M. McConnell and R. J. Lynden-Bell, J. Chem. Phys. 36 (1963) 2393;
D. D. Thomas and H. Keller and H. M. McConnell, J. Chem. Phys. 39 (1962) 2321;
D. B. Chesnut, J. Chem. Phys. 46 (1966) 4677.

[8] R. S. Hayano *et al*, Phys. Rev. B20 (1979) 850;
Y. J. Uemura *et al*, Phys. Rev. B31 (1985) 546.

[9] M. Azuma *et al*, Phys. Rev. Lett. 73 (1994) 3463.

[10] D. J. Buttrey *et al*, J. of Solid State Chem. 88 (1990) 291.

[11] Y. J. Uemura *et al*, Phys. Rev. Lett. 73 (1994) 3306.

[12] M. Hase *et al*, Phys. Rev. Lett. 70 (1993) 3651;
M. Hase *et al*, Phys. rev. Lett. 71 (1993) 4059.

MUON SPIN RELAXATION MEASUREMENTS OF SINGLET GROUND-STATE MATERIALS

KENJI KOJIMA*

Abstract

This thesis reports experimental investigations of three types of spin systems, namely, (1) spin-ladder materials $Sr_{n-1}Cu_{n+1}O_{2n}$, (2) a Haldane material Y_2BaNiO_5 and (3) a spin-Peierls compound $CuGeO_3$. The common feature of these spin systems is the absence of conventional Néel order due to quantum mechanical effects; the ground state structures are characterized by singlet-pair formations of spins, as introduced in Chapter 1. In this thesis, the muon spin relaxation (μSR) method is the main experimental technique. Therefore in Chapter 2, the μSR technique is introduced, followed by a brief introduction to spin relaxation theories in solids (Chapter 3). Most of the content of these two chapters is important for the understanding of the subsequent chapters, in which the experimental results are presented.

In Chapter 4, the magnetism of the spin-ladder materials $Sr_{n-1}Cu_{n+1}O_{2n}$ is discussed. With the μSR technique, it was found that magnetic behavior of these spin ladder cuprates strongly depends on the width of the ladder. The μSR spectra from the ladder materials provide a good experimental example of the spin relaxation theories introduced in Chapter 3. The content of this chapter has been published as Ref. [1].

Chapter 5 presents the μSR results of a Haldane material Y_2BaNiO_5. A related vacancy-doped system, $Y_2Ba(Ni_{1-y}Mg_y)O_5$, and charge-doped system, $(Y_{2-x}Ca_x)BaNiO_5$, were also investigated. It was found that vacancy doping and charge doping lead to completely different ground states. In the charge-doped compounds especially, unconventional spin dynamics were observed in the milli-Kelvin regime. Most of the results in this chapter have been published in Ref. [2, 3].

In Chapter 6, μSR results of an inorganic spin-Peierls material $CuGeO_3$ and two types of doped compounds $[(Cu_{1-x}Zn_x)GeO_3$ and $Cu(Ge_{1-y}Si_y)O_3]$ are reported. It was found that these two types of doping result in a magnetically ordered state; it was clearly Néel order in the Si-doped system.

Concluding remarks are given in the last chapter, Chapter 7.

SUBMITTED IN PARTIAL FULFILLMENT OF THE
REQUIREMENTS FOR THE DEGREE
OF DOCTOR OF SCIENCE
IN THE GRADUATE SCHOOL OF SCIENCE

THE UNIVERSITY OF TOKYO

DECEMBER, 1995

*e-mail address: kenji@reg.triumf.ca

Contents

†The contents of these chapters have been published as Ref. [1, 2, 3].

††Unpublished work under collaboration.

‡The authors original work, *unpublished*.

1 General introduction

1.1 Antiferromagnetic spin systems without Néel order

It has been believed that a macroscopic spin system with an antiferromagnetic interaction would freeze at a Néel temperature, which is comparable to the magnitude of the interaction (J). But recently, several theoretical situations have been proposed, in which an antiferromagnetic spin system prefers a many-body *singlet ground state*, rather than the Néel state. These situations include low dimensionality and/or geometrical frustration of the spins, so that the conventional Néel order is suppressed. Amazingly, several materials have been discovered which may realize the theoretical situations. In this thesis, I will report experimental results of three such spin systems, namely, (1) the spin-ladder system $Sr_{n-1}Cu_{n+1}O_{2n}$, (2) Haldane compound Y_2BaNiO_5 and (3) the spin-Peierls system $CuGeO_3$. Although the detailed structures of the ground states differ among these spin systems, they share one important concept for a general understanding of the many-body singlet ground states; it is the singlet pair formation of two spins.

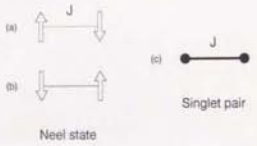

Figure 1:
(a, b) The Néel state and (c) the singlet pair state for a two S=1/2 spin system.

Suppose two S=1/2 spins interact with an antiferromagnetic coupling (J):

$$\begin{aligned}\mathcal{H} &= JS_1 \cdot S_2 \\ &= J(S_1^z S_2^z + S_1^x S_2^x + S_1^y S_2^y) \\ &= J\left(S_1^z S_2^z + \frac{1}{2}(S_1^+ S_2^- + S_1^- S_2^+)\right) \qquad (1)\end{aligned}$$

In classical mechanics, the ground state of this two-spin system is the Néel state, in which the two spins point in opposite directions (Fig.1a, b). In quantum mechanics, spin-flips caused by the xy terms of the Hamiltonian (eq.1) prevent the Néel state from serving as an eigenstate of the Hamiltonian. After a simple calculation, one finds that the spin singlet pair $(|\uparrow\downarrow\rangle - |\downarrow\uparrow\rangle)/\sqrt{2}$ is the quantum mechanical ground state of this system (Fig.1c).

The singlet pair state is a mixed state of the two Néel states and does not have a classical counterpart. Still, this state is often realized in localized two electron systems, such as valence bonds in molecules. One characteristic feature of the singlet pair is that the magnetic dipolar field from each spin is exactly canceled; in other words, there is no magnetic field induced around a singlet pair. This is the main reason why most molecules do not show magnetism. In macroscopic localized spin systems, singlet pair formation becomes difficult, because a spin on a lattice has at least two nearest neighbors. Since the singlet pair is a state for just two S=1/2 spins, one spin on the lattice must select one specific partner from the equivalent neighboring spins, which is difficult in translationally symmetric systems. Consequently, most macroscopic spin systems with an antiferromagnetic interaction exhibit Néel order.

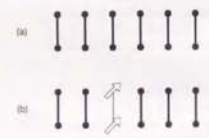

Figure 2:
(a) An example of a trivial spin-gap system: local singlet pairs without any correlations. (b) The first excited state.

As shown in the next section, some macroscopic spin systems still prefer a ground state based on the singlet pair formations of the spins. Some of these unconventional spin systems are characterized by an energy gap between the ground state and the magnetic excited states. Since this energy gap originates from the spin degrees of freedom, it is often called a 'spin gap'. The existence/absence of the spin gap is probably related to how well the singlet pairs are localized. For example, a crystal made up of many uncorrelated singlet pairs (Fig.2a) is a trivial example of a spin-gap system; the energy excitation spectrum of this system will have a gap, which corresponds to the singlet-triplet excitation of a singlet pair (Fig.2b). Another example, the S=1/2 spin-chain with an antiferromagnetic Heisenberg interaction is a non-trivial gap-less system. The ground state of this system is a many-body singlet [11], which is approximately expressed as the superposition of *every* possible singlet pairing on the chain [12]. This ground state, which is known as the Resonating Valence Bond (RVB) state, has completely delocalized singlet pairs, and the excitation to the triplet state becomes gap-less [13]. In this thesis, materials with a

spin gap, namely, the spin systems with relatively well localized singlet pairs, are investigated.

1.1.1 An overview of singlet ground state systems

Spin Peierls system

Historically, the 'spin Peierls' system was the first macroscopic system proposed to have a spin gap [14, 15, 16]. It consists of an S=1/2 antiferromagnetic spin chain with a spin-lattice coupling. If the lattice is soft in the chain direction, and the chains are magnetically well separated from each other [17, 18], a periodic deformation (dimerization) of the lattice takes place at a finite temperature T_{SP} (Fig.3a→b). The lattice dimerization alternatively enhances $[J(1+\delta)]$ or reduces $[J(1-\delta)]$ the antiferromagnetic interactions, and brings about singlet pair formations on the enhanced exchange links (Fig.3b).

Figure 3:
(a) An S=1/2 spin chain with an uniform antiferromagnetic interaction J. (b) The lattice dimerized state below the spin Peierls transition temperature T_{SP}.

The ground state structure of the spin-Peierls system is a stacking of singlet pairs along the chain. The ground state is non-magnetic, because each singlet pair produces no magnetic field. Since the singlet pairs are well localized, there is a finite energy gap between the ground state and the excited states. This system is studied in Chapter 6.

Spin ladder system

If one changes the stacking orientation of the singlet pairs from that of the spin Peierls state, the ground state of the smallest 'spin ladder' system is obtained [19]. The spin ladder system is an S=1/2 antiferromagnetic square lattice with finite width and infinite length (Fig.4a). The ground state of this system depends on the lattice width, namely, the number of 'legs' in the ladder. If the number of the legs is *even*, the ground state becomes non-magnetic with a finite energy gap to the excited states [20, 21]; if it is *odd*, the energy gap collapses [21]. For the 2-leg ladder system, the non-magnetic ground state can be visualized as shown in Fig.4b; it is a stacking of singlet pairs on the rungs. The finite energy gap of this system originates from the localization of these singlet pairs. In the 3-leg ladder system, the localized pair formation on the rungs becomes impossible, and hence the energy gap collapses. These systems are discussed in Chapter 4.

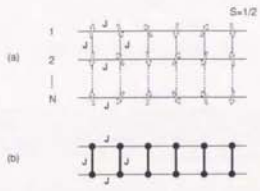

Figure 4:
(a) The N-leg spin ladder structure and (b) a schematic ground state of the 2-leg spin ladder system.

Haldane systems

The two systems introduced above have a geometrical reason for two specific spins to form a singlet pair. In the next system, the S=1 antiferromagnetic spin chain, the value of the spin (integer) makes it possible to form singlet pairs.

In 1983, F. D. M. Haldane conjectured that in the Heisenberg model, antiferromagnetic chains of *integer* spins would show a finite energy gap between the singlet ground state and the triplet first excited state. He also claimed that the spin correlation of the ground state quickly decays as an exponential function of distance [22, 23]. These two features propose that the integer-spin Heisenberg model has a highly disordered ground state, which is far from the Néel state. Haldane's predictions were surprising, because the same Heisenberg model, with S=1/2 spins, is gap-less and has a power-law decay of the correlation function [11].

In 1987, an intuitive picture for the Haldane's ground state was proposed, with an exactly soluble S=1 spin Hamiltonian [24, 25]:

$$\mathcal{H} = \sum_{i=-\infty}^{\infty} \left(\boldsymbol{S}_i \cdot \boldsymbol{S}_{i+1} + \frac{1}{3}(\boldsymbol{S}_i \cdot \boldsymbol{S}_{i+1})^2\right) \qquad (2)$$

which adds a biquadratic term to the Heisenberg model. The ground state of this Hamiltonian (Valence Bond Solid state; Fig.5b) was mathematically proved to have a spin-gap and an exponentially decaying correlation function [24, 25, 26, 27]. The model without the biquadratic term (Heisenberg model) is believed to have

a similar ground state structure to that of the Valence Bond Solid state. See Chapter 5 for more about the Haldane systems.

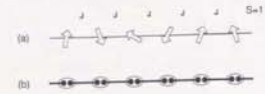

Figure 5:
(a) An S=1 spin chain. (b) A schematic view of the Valence Bond Solid (VBS) state, which is based on many singlet pairs. The circle at each site represents the projection of two S=1/2 spins to one S=1.

1.1.2 The idea of the measurements in this thesis

The three spin systems introduced above (spin Peierls, even-leg-number spin-ladder and the Haldane system) are characterized by (1) a non-magnetic ground state and (2) a finite energy gap between the ground state and the first excited state. Up to now, numerous experiments have been performed to detect the energy gap in model materials of these spin gap systems, and some of these have successfully found the gap.

The experiments presented in this thesis investigate other feature of the spin gap systems: *the absence of an internal magnetic field in the ground state*. As the main experimental technique, I have utilized the Positive Muon Spin Rotation/Relaxation (μSR) technique [6, 7, 28], which is the most sensitive microscopic probe currently available for small and/or dilute magnetic moments. For example, it is straight forward for the μSR technique to detect the nuclear dipolar fields which originate from nuclear magnetic moments as small as $\sim 10^{-3}\mu_B$ (μ_B denotes the electron Bohr magneton) [6]. The high sensitivity to dilute moments is seen in investigations of dilute spin glass alloys [7]; static moments as dilute as ~0.1% are easy to investigate with the μSR technique. These two experiments have shown that μSR is the most sensitive probe to confirm the absence/presence of magnetic order in a spin system.

Another favorable feature of μSR is that one may investigate spin fluctuations around the muon with the help of spin relaxation theories in solids. In some of the spin gap materials, non-magnetic ion and/or charge doping to the system has been performed, and it was found that the doping induces moments from the sea of singlet pairs. This thesis presents μSR measurements of these doped systems as well, in order to clarify the fluctuations of the induced moments.

The structure of this thesis is as follows: the following two chapters (Chapter 2 and 3) introduce the μSR technique and the spin relaxation theories, which are necessary to understand the experimental results. The subsequent three chapters are devoted to spin-ladder materials $Sr_{n-1}Cu_{n+1}O_{2n}$ (Chapter 4), a Haldane material Y_2BaNiO_5 (Chapter 5) and a spin-Peierls material $CuGeO_3$ (Chapter 6). Concluding remarks are given in Chapter 7.

2 The muon spin rotation/relaxation (μSR) technique

2.1 The basics

The μSR technique is based on the two properties of muons:

(a) muons are 100% spin-polarized, when produced from the $\pi\mu$ decay:

$$\pi^+ \rightarrow \mu^+ + \nu_\mu \qquad (3)$$

(b) muons decay into one positron and two neutrinos with a lifetime of τ_μ=2.2μs:

$$\mu^+ \rightarrow e^+ + \nu_e + \bar{\nu}_\mu \qquad (4)$$

The feature (a) results from the 'parity violation' of the weak decays, namely, the fact that only left-handed neutrinos exist. As shown in Fig.6, the muon from the $\pi\mu$ decay has to be spin-polarized, in order to conserve the total spin zero of the pion.

Figure 6:
Schematic view of the $\pi\mu$ decay. The muon is spin polarized, because pion has spin 0 and neutrino is spin-polarized.

The feature (b) yields an asymmetric angular distribution of the decay-positrons relative to the muon spin direction. The angular distribution of decay positrons depends on their kinetic energy, which ranges from 0 to $E_{max}\approx m_\mu c^2/2$=53 MeV. The angular distribution is expressed as [29]:

$$dN = \frac{1 + a(\epsilon)\cos\theta}{4\pi} d\Omega \times \rho(\epsilon) d\epsilon \qquad (5)$$

where

$$a(\epsilon) = (2\epsilon - 1)/(3 - 2\epsilon) \qquad (6)$$
$$\rho(\epsilon) = 2(3 - 2\epsilon)\epsilon^2 \qquad (7)$$

and $\epsilon = E/E_{max}$ is the normalized positron energy, θ is the angle of positron emission measured from the muon spin direction, and $d\Omega$ is a small solid angle. After integrating the positron energy, the angular distribution behaves as shown in Fig.7.

The basic idea of the μSR technique follows the next three steps:

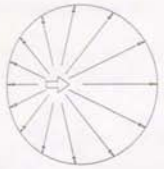

Figure 7:
Angular distribution of the positron after integrating over its energy. The radial distance represents the relative probability that a positron is emitted in a given direction.

(1) a muon is implanted in the sample with its spin polarized.

(2) the muon spin changes its direction because of the magnetic environment around.

(3) the muon decays into a positron and two neutrinos. The muon spin polarization at the time of the decay is reconstructed by measuring the positron directions for many incident muons.

Detection of positrons

To reconstruct the muon spin direction, it is convenient to have two positron counters which are placed symmetrically with respect to the sample (muon) position, as shown in Fig.8.

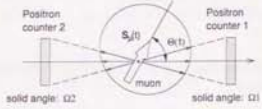

Figure 8:
A positron counter configuration to reconstruct muon spin polarization.

We define the muon spin polarization along the counter axis as $P_\mu(t) = \cos\Theta(t)$, where $\Theta(t)$ is the time evolution of the muon spin angle relative to the counter axis (see Fig.8). The positron count rate of each counter $N_i(t)$ (i=1,2) is found by integrating the positron angular distribution of this tilted muon spin

over the counter solid angle and positron energy. The answer becomes:

$$N_1(t) = N_1^0 \exp(-t/\tau_\mu)(1 + A_1 P_\mu(t)) \quad (8)$$
$$N_2(t) = N_2^0 \exp(-t/\tau_\mu)(1 - A_2 P_\mu(t)) \quad (9)$$

where

$$N_i^0 = \frac{\Omega_i}{4\pi} \times \int_0^1 \rho(\epsilon)\eta(\epsilon)d\epsilon \quad (10)$$

$$A_i = \frac{\int_0^1 a(\epsilon)\rho(\epsilon)\eta(\epsilon)d\epsilon}{\int_0^1 \rho(\epsilon)\eta(\epsilon)d\epsilon} \times \frac{1}{\Omega_i}\int_{\Omega_i} |\cos\theta| d\Omega \quad (11)$$

Here, $\tau_\mu (= 2.2\,\mu s)$ is the muon lifetime, $\eta(\epsilon)$ is the detection efficiency of the positron counters and Ω_i is the solid angle of the counter i (=1,2). A_i is called the asymmetry of the individual counters, which is typically 0.2~0.3 in a conventional μSR setup.

The muon spin polarization $P_\mu(t)$, which is the information one would like to obtain from the μSR technique, is calculated by taking the *corrected asymmetry* (eq.12), which is essentially the count difference of the two counters normalized by the total count:

$$A_1 P_\mu(t) = \frac{\alpha N_1(t) - N_2(t)}{\alpha\beta N_1(t) + N_2(t)} \quad (12)$$

where the parameter $\alpha \equiv N_2^0/N_1^0 = \Omega_2/\Omega_1$ (= 1; ideally) corrects the deviation of the solid angles between the two counters, and $\beta \equiv A_2/A_1$ (= 1; ideally) corrects the difference of the counter asymmetries.

In Fig.9, an example of the positron counts $[N_1(t)]$ and the corrected asymmetry $[A_1 P_\mu(t)]$ is shown. A Larmor precession of the muon spin is seen, as an external magnetic field perpendicular to the initial muon spin direction was applied during this measurement.

The next section presents more details of the experimental setup which is required for the μSR measurements.

2.2 Experimental setup for the μSR technique

In order to perform μSR measurements, one has to visit a facility which produces many muons. Currently, there are five such 'meson factories' available in the world (see Table 1). The heart of these facilities is a particle accelerator which provides a particle beam with an kinetic energy of a few hundred mega electron volts (MeV). For this high energy regime, there are two types of accelerators available, namely, the cyclotron and the synchrotron. The time structure of the muon beam reflects the accelerator type of the facility and it determines the details of the μSR setup.

In the synchrotron-based facilities (KEK and RAL), muons come in a pulse, with a spread of ~50 ns and a pulse-to-pulse interval of ~20 ms. Since the muon arrival time ($t = 0$) is known from the timing signal of the synchrotron, μSR measurements are performed by taking the time spectra of decay positrons relative to the muon pulse. The timing resolution of this 'pulse-μSR' method is limited by the muon pulse-width (~50 ns), but the experimental time window is virtually infinite ($\sim 20\ \text{ms} \gg \tau_\mu = 2.2\ \mu s$). The long experimental time window makes this method convenient for measurements of slow muon spin relaxation. The pulse-μSR method is also convenient to introduce extreme conditions, such as high-magnetic fields [30] and optical radiations [31, 32], using a pulse magnets/lasers synchronized to the muon pulse.

The cyclotron-based facilities (TRIUMF and PSI) provide a continuous muon beam. As a result, one needs a muon counter on the beam path right before the sample, so that one knows a muon arrival time ($t = 0$). The timing resolution of this 'continuous-beam' μSR method is theoretically infinitesimally small; with carefully tuned electronics and small counters, sub-nanosecond resolution ($\Delta t < 1$ ns) may be achieved [33]. The experimental time window is typically ~12 μs, which is limited by the random background and the pile-up of second muon arrival (see section 2.2.3).

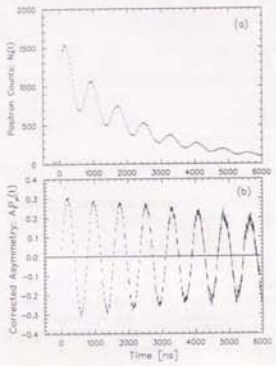

Figure 9:
(a) A typical time spectrum of one positron counter. (b) The corrected asymmetry (Eq.12) of the same measurement.

Since all the data in this thesis were obtained at TRIUMF, I will explain more details of the continuous-beam μSR method in the following sections.

Table 1: Muon facilities in the world

Name (location)	Accelerator	Muons/cm^2/sec (pulse width)
PSI (Switzerland)	cyclotron	~ 3×10^5 (DC)
TRIUMF (Canada)	cyclotron	~ 2×10^6 (DC)
LAMPF (U.S.A)	synchrotron	~ 1×10^6 (0.7ms)
RAL (U.K.)	synchrotron	~ 1×10^5 (100ns)
KEK (Japan)	synchrotron	~ 3×10^4 (50ns)

2.2.1 Production of a muon beam

The heart of TRIUMF (TRI-Universities Meson Facility) is a 520 MeV H^- cyclotron with a high beam-intensity (140μA). An accelerated proton beam is lead to a production target made of Graphite or Beryllium. Proton hit the target-nuclei and create pions via nuclear reactions.

To obtain muons, one must wait for the pions to decay, which typically takes 26 ns (pion lifetime). To obtain positive muons (μ^+), one can stop positive pions (π^+) in the production target and wait for their decay, because the positive charge of the pions prevent them from being absorbed into the surrounding nuclei. These stopped positive pions produce positive muons which are fully polarized anti-parallel to their momenta (see Fig.6). These muons are called the 'surface muons', because they are emitted from the surface of the production target. Surface muons have (1) high spin-polarization (~100%), (2) low momentum (29.8 MeV/c~170 mg/cm^2 as the stopping range), and (3) small beam image (a few centimeters in diameter). These features are all favorable for μSR measurements. The muon channels M13, M15 and M20 at TRIUMF are designed to deliver surface muons.

Fig.10 shows a schematic view of the M15 muon channel at TRIUMF. Four dipole magnets (B1-B4) on the beamline bend the beam and select the momentum of the muons. Quadrupole magnets (QAQB, Q1-Q17) focus the muon beam. The DC-separators (SEPARATOR1 and 2) provide crossed electric and magnetic fields perpendicular to the beamline (see the inset of Fig.10). This apparatus eliminates positrons from the muon beam by setting the field ratio (E/B) to the muon velocity (v_μ). Secondly, this apparatus can rotate muon spins away from the momentum direction, by applying higher E and B fields. All of the surface muon channels at TRIUMF are equipped with at least one DC-separator; M20 and M15 have the capability to rotate the muon spins by 90°.

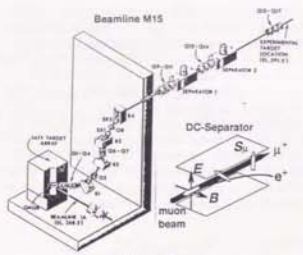

Figure 10:
A schematic view of the M15 beam line at TRIUMF.

2.2.2 μSR spectrometer

The muon beam is tightly collimated to the sample size at the end of the beam pipe, which is sealed with a thin Kapton or mylar window. Muons pass through the beam window and reach the spectrometer: a complex of a cryostat, particle counters and magnets. Fig.11 shows a schematic top-view of a typical μSR spectrometer.

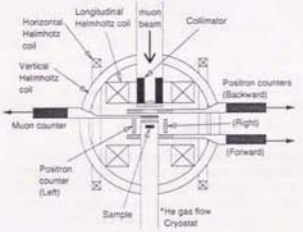

Figure 11:
A top-view of a typical μSR spectrometer, which is an assembly of particle counters, magnets and a cryostat.

Particle counters

The particle counters used in conventional μSR measurements are usually plastic scintillator (dark gray in Fig.11) attached to a photo-tube (black) through a light-guide; the photo-tube gives an electrical pulse

when a charged particle (μ^+ or e^+) passes through the scintillator. The muon counter, which is placed between the beam window and the sample, provides the muon arrival signal ($t = 0$). The scintillator of the muon counter is thin (thickness ~0.25 mm) so that it doesn't prevent muons from reaching the sample. The positron counters (Backward, Forward, Left and Right counters) are placed symmetrically with respect to the sample position, so that the muon spin polarization can be reconstructed as described in section 2.1. The scintillators for the positron counters are relatively thick (~1 cm) to have a good detection efficiency for the relativistic decay positrons (momentum ~50 MeV/c).

Magnets

A μSR spectrometer is usually equipped with three pairs of Helmholtz coils: one longitudinal ($\boldsymbol{H}$ ‖beamline), one vertical and one horizontal pair. These three magnets makes it possible to null the magnetic field at the sample position for zero-field (ZF) μSR measurements. The longitudinal magnet is also used to apply higher external magnetic field during the measurements.

Cryostats

For the μSR measurements of this thesis, two types of cryostats were employed: a ^{4}He gas flow cryostat and a dilution refrigerator. In the ^{4}He gas flow cryostat, the samples were suspended close to the end of a sample chamber, which is a tube ($\phi \sim 7.5\,\mathrm{cm} \times L \sim 50\,\mathrm{cm}$) with a sealed beam window at the sample position. The chamber has a ^{4}He-diffuser close to the sample position, which is connected to a ^{4}He dewar through a capillary with a needle valve. The diffuser provided gaseous ^{4}He to the sample chamber. The cooling power was roughly controlled with the needle valve. The other end of the sample chamber is connected to a rotary vacuum pump. By reducing the pressure in the sample chamber, the cryostat can reach ~1.8 K. There are two heaters equipped in this cryostat: one at the diffuser, and the other at the sample position. The diffuser heater finely tuned the cooling power, and determined the temperature of the ^{4}He gas flowing to the sample chamber. The sample heater was connected to a temperature controller (Lakeshore DRC-92C) and stabilized the temperature at the sample position. For temperature reading and control, a carbon glass register and a platinum thermometer (or a GaAlAs diode for the full temperature range) were used at the sample position and at the diffuser.

The dilution refrigerator we used (Oxford 400) is a conventional closed-cycle refrigerator, circulating the ^{3}He/^{4}He mixture. The sample was attached to a sample holder, which was screwed onto the mixing chamber. Since the samples were in vacuum, the cooling power for the sample depends on the thermal conduction. To maximize the thermal conduction, Apiezon grease or GE varnish was applied between the sample and the sample holder. The cooling power was controlled by the circulation rate of the ^{3}He/^{4}He mixture, while the temperature was controlled using a heater on the mixing chamber. The mixing chamber was equipped with a carbon resistor for temperature reading; the base temperature of the refrigerator was typically 20 mK. The dilution refrigerator shares a ^{4}He dewar with a superconducting Helmholtz coil which supplied a field parallel to the beam axis at the sample position.

Table 2 summarizes the features of the three spectrometers currently available at TRIUMF. Most of the data presented in this thesis have been obtained using the OMNI and the DR spectrometers, often in combination.

Table 2: The μSR spectrometers at TRIUMF.

Name	Cryostat (temperature range)	Longitudinal Magnets (H_{max})
DR	Dilution Refrigerator (20 mK~20 K)	Superconducting Helmholtz (60 kG)
OMNI	^{4}He flow cryostat (1.8 K~300 K)	Normal Helmholtz coil (3.5 kG)
HELIOS	^{4}He flow cryostat (3 K~300 K)	Superconducting Solenoid (70 kG)

2.2.3 Electronics and data handling

The signals from the muon/positron counters are shaped to a logical pulse using the CFD (Constant Fraction Discriminator), which is commonly used in nuclear experiments. The logical pulses are handled by the circuits shown in Fig.12, in order to take the time spectrum of the μe decay. The main scheme of the electronics follows the thick solid lines; the 'muon signal' starts the stopwatch called TDC (Time to Digital Converter) and one of the "positron signals' stops it. The elapsed time between these two events is stored in the histogram memory, along with the information of which positron counter gave the stop signal. The histogram memory is read by the data-taking VAX-computer typically every 5 minutes.

The circuit is equipped with 'pile-up rejection' logic (thin solid line in Fig.12), which is necessary for μSR measurements using a continuous beam, as at TRIUMF. This circuit rejects situations where more than two muons reside in the apparatus within the experimental time window; in this situation, there is no way of knowing which muon decays to a given positron, and therefore, the data must be thrown away. The gate generator with the dashed lines determines the time range of interest for the measurements (~12 μs). This

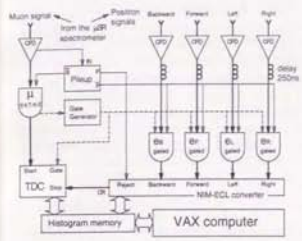

Figure 12:
A block diagram of the logical circuit for a μSR measurement.

time range is usually set ~500 ns shorter than the time window for the pileup rejection.

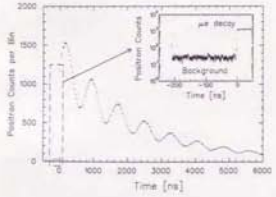

Figure 13:
A typical time spectrum of one positron counter. The inset shows the same spectrum at the early time range.

Using the electronics described as above, as well as the muon-beam and the spectrometer, one obtains the time spectrum of the μe decay, as shown in Fig.13. There is, however, random background overlapping the spectrum, an inevitable feature of continuous-beam experiments. Usually, one assumes that the background is time independent, and estimates its level from the spectrum at the t<0 range (the inset of Fig.13). The estimated background is evenly subtracted from the measured spectrum. The existence of the background sets the technical upper-limit of the experimental time range (~12 μs) available for the continuous-beam μSR method.

After subtracting the background, one calculates the corrected asymmetry (eq.12), and obtains the time evolution of the muon spin polarization, as shown in Fig.9b.

2.2.4 Counter/muon spin geometries

In general, there are two types of spin relaxation defined: the T_1 and the T_2 relaxation [34]. In μSR measurements, the meaning of these two spin relaxation becomes intuitive, because the muon spin is polarized at $t = 0$.

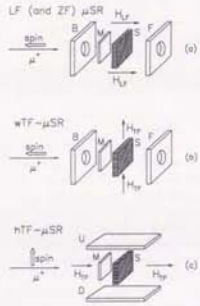

Figure 14:
(a) Longitudinal field (LF) and Zero field (ZF) μSR. (b) Weak transverse field (wTF) μSR. (c) high transverse field (hTF) μSR.

The T_1 relaxation is defined as the relaxation of the spin component *parallel* to the external magnetic field [34]. In order to measure the T_1 relaxation with μSR, one uses the configuration shown in Fig.14a, because the muon spin is parallel to the beam axis by default (see Fig.6).

With the same counter configuration (Fig.14b), it is also possible to measure T_2 relaxation, which is the relaxation of the spin components *perpendicular* to the external field [34]. In this counter geometry, there is a certain upper limit for the transverse field H_{TF} (~200 G for surface muons), because the muon trajectory curves in the magnetic field, and in the worst case, it misses the sample. For T_2 relaxation measurements in higher fields, the 'Left-Right' (or 'Up-Down') configuration has to be employed (Fig.14c). The measurement with this configuration requires a good DC-separator on the beamline, which is capable of rotating

the muon spin perpendicular to the beam (see inset of Fig.10).

One benefit to the μSR method is that measurements in *zero* magnetic field are possible. This condition yields the highest sensitivity to small internal magnetic fields. To understand the spin relaxation in the zero-field, the spin relaxation theories developed for the Nuclear Magnetic Resonance (NMR) method become inadequate, because those theories assume the existence of an external magnetic field. The next chapter introduces spin relaxation theories which are applicable to this zero-field condition.

3 Spin relaxation theories

3.1 Gaussian Kubo-Toyabe theory [4, 5, 6]

A conventional spin relaxation theory in zero and low external fields (Kubo-Toyabe theory [4, 5, 6]) begins with the assumption that there are no fluctuations in the spin system. In this static situation, each muon detects a local field ($\boldsymbol{H}_{\rm loc}$) which causes Larmor precession of the muon spin (Fig.15). The time evolution of the muon spin in the static local field behaves as:

$$S_\mu(t;\boldsymbol{H}_{\rm loc}) = \cos^2\theta + \sin^2\theta\cos\gamma_\mu|\boldsymbol{H}_{\rm loc}|t \quad (13)$$

where θ is the angle between the static local field ($\boldsymbol{H}_{\rm loc}$) and the initial muon spin direction ($\boldsymbol{S}_\mu(t=0)$), and γ_μ is the gyromagnetic ratio of the muon spin ($=2\pi\times 13.554$ kHz/G). Hereafter, the z-axis is defined to be the direction of the initial muon spin polarization.

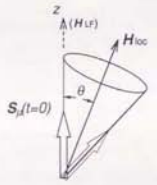

Figure 15:
Larmor precession of a muon spin in a static local field $H_{\rm loc}$.

When the local field has a distribution $\rho(\boldsymbol{H})$, the muon spin relaxation observed is the ensemble average of the individual muon spin precession:

$$P_\mu(t) = \int d\boldsymbol{H}\rho(\boldsymbol{H})S_\mu(t;\boldsymbol{H}) \quad (14)$$

If the field distribution is isotropic, or the measurement is done on a polycrystalline specimen, one can integrate the angular part:

$$\begin{aligned} P_\mu(t) &= \int_0^{2\pi} d\phi \int_{-1}^{1} d\cos\theta \int_0^\infty H^2 dH \rho(H) \\ &\quad \times (\cos^2\theta + \sin^2\theta\cos\gamma_\mu Ht) \\ &= \frac{1}{3} + \frac{2}{3}\int_0^\infty 4\pi H^2\rho(H)\cos\gamma_\mu Ht dH \end{aligned} \quad (15)$$

The first term (*1/3-component*) originates from the fraction of the local field which is parallel to the initial muon spin polarization. This term is an important signature of static relaxation, because its existence doesn't depend on the shape of the field distribution. The second term (*2/3-component*) is the Fourier transform of the field distribution, and hence, contains all information about $\rho(H)$.

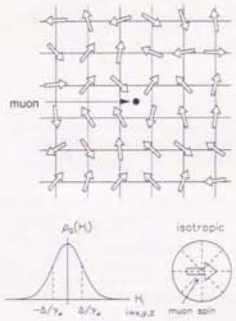

Figure 16:
Randomly oriented dense spin system. The local field is well approximated with an isotropic Gaussian distribution.

In a randomly oriented frozen spin system, with a static moment at every lattice point (Fig.16), the dipolar field at a muon site is well approximated by an isotropic Gaussian distribution:

$$\rho_{\rm G}(H_i) = \frac{\gamma_\mu}{\sqrt{2\pi}\Delta}\exp\left(-\frac{\gamma_\mu^2 H_i^2}{2\Delta^2}\right),\ i=x,y,z \quad (16)$$

$$\rho_{\rm G}(|\boldsymbol{H}|) = \left(\frac{\gamma_\mu}{\sqrt{2\pi}\Delta}\right)^3\exp\left(-\frac{\gamma_\mu^2|\boldsymbol{H}|^2}{2\Delta^2}\right) \quad (17)$$

where Δ is the width of the Gaussian distribution. The corresponding muon spin relaxation is derived by performing the integral:

$$\begin{aligned} G^{\rm GKT}(t;\Delta) &= \frac{1}{3} + \frac{2}{3}\int_0^\infty 4\pi H^2\rho_{\rm G}(H)\cos\gamma_\mu Ht dH \\ &= \frac{1}{3} + \frac{2}{3}(1-(\Delta t)^2)\exp\left(-\frac{1}{2}(\Delta t)^2\right) \end{aligned} \quad (18)$$

This result, known as the 'static Gaussian Kubo-Toyabe function' in zero-field, was first derived by R. Kubo and T. Toyabe in 1966 [4, 5].

As shown later in this chapter, it is important to investigate the muon spin relaxation in a 'longitudinal field', which is the external magnetic field applied parallel to the initial muon spin polarization ($H_{\rm LF}$; see Fig.15). The static Gaussian Kubo-Toyabe function in longitudinal fields is expressed as [6]:

$$\begin{aligned} &G^{\rm GKT}(t;\Delta,H_{\rm LF}) \\ &= \int d\boldsymbol{H}\rho_{\rm G}(H-zH_{\rm LF})S_\mu(t;\boldsymbol{H}) \\ &= 1 - 2\left(\frac{\Delta}{\gamma_\mu H_{\rm LF}}\right)^2(1-e^{-\Delta^2t^2/2}\cos\gamma_\mu H_{\rm LF}t) \\ &\quad +2\left(\frac{\Delta}{\gamma_\mu H_{\rm LF}}\right)^3\Delta\int_0^t e^{-\Delta^2\tau^2/2}\sin\gamma_\mu H_{\rm LF}\tau d\tau \end{aligned} \quad (19)$$

In Fig.17, the static Gaussian Kubo-Toyabe function $G^{\rm GKT}(t;\Delta,H_{\rm LF})$ is shown for various longitudinal fields. In zero magnetic field, the function first decays as a Gaussian and then comes back up to the non-relaxing 1/3-component. With a longitudinal field applied, the amplitude of the flat component increases, because the fraction of the field which is parallel to the initial muon spin polarization increases. In static relaxation, the magnitude of the longitudinal field which decouples the relaxation is comparable to the field distribution width ($H_{\rm LF}\sim\Delta/\gamma_\mu$). The distribution width can also be extracted from the Gaussian decay-rate at early times before the recovery.

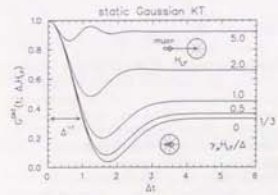

Figure 17:
The muon spin relaxation in the randomly oriented frozen dense spin system: static Gaussian Kubo-Toyabe function $G^{\rm GKT}(t;\Delta,H_{\rm LF})$. The circle in the figure represents the isotropic random field distribution, which is centered at zero in zero external field; if the longitudinal field ($H_{\rm LF}$) is applied, the random field is centered at $H_{\rm LF}$.

Experimentally, the Gaussian Kubo-Toyabe behavior of the muon spin relaxation, as well as its longitudinal field dependence, is typically observed in substances with nuclear magnetic moments, such as MnSi [6] and copper [35].

Effect of spin fluctuations [36, 6]

In the framework of the Kubo-Toyabe theory, the effects of field fluctuations have been taken into account with the 'strong collision model' [36, 6]. This model assumes that (1) fluctuations occur suddenly, and that (2) every time the local field fluctuates, the muon forgets the previous local field information. Hereafter, the field fluctuation rate (ν) is defined as the Markoffian fluctuation rate, namely, the exponential decay rate of the autocorrelation function of the local fields:

$$\frac{< \boldsymbol{H}_{\rm loc}(0) \cdot \boldsymbol{H}_{\rm loc}(t) >}{< |\boldsymbol{H}_{\rm loc}(0)|^2 >} = \exp(-\nu t) \qquad (20)$$

The strong collision model generally calculates the dynamical muon spin relaxation $G^{\rm D}(t;\nu)$ from the original static relaxation function $G(t)$ as follows:

$$\begin{aligned} & G^{\rm D}(t;\nu) \\ &= e^{-\nu t} G(t) \\ &+ e^{-\nu t} \nu \int_0^t dt' G(t-t') G(t') \\ &+ e^{-\nu t} \nu^2 \int_0^t dt' \int_0^{t'} dt'' G(t-t') G(t'-t'') G(t'') \\ &+ \cdots \end{aligned} \qquad (21)$$

The terms of this series account for the muons which experienced $0, 1, 2, \cdots$ field fluctuations in the time interval of $0 \sim t$.

Fig.18 shows the dynamical Gaussian Kubo-Toyabe function in zero-field for various fluctuation rates (ν). In the slow fluctuation regime ($\nu/\Delta \lesssim 0.1$), the fluctuation induces slow relaxation of the 1/3-component. The asymptotic behavior of this relaxation has been obtained as $\sim 1/3 \exp(-2\nu t/3)$ [6]. In the intermediate fluctuation regime ($0.1 \lesssim \nu/\Delta \lesssim 2$), the relaxation has a Gaussian behavior in the beginning, but loses the 1/3-component. Hence, the existence/absence of the 1/3-component is a clue which distinguishes static/dynamic relaxation.

In the fast fluctuation regime ($\nu/\Delta \gtrsim 10$), the relaxation is approximated by an exponential function [7, 37]:

$$G^{\rm DGKT}(t;\Delta, H_{\rm LF}, \nu) \approx \exp(-\lambda t) \qquad (22)$$

where the relaxation rate is:

$$\lambda = \frac{2\Delta^2 \nu}{\nu^2 + (\gamma_\mu H_{\rm LF})^2} \qquad (23)$$

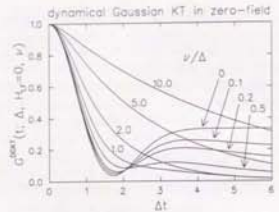

Figure 18:
The zero-field muon spin relaxation in the fluctuating Gaussian local field (dynamical Gaussian Kubo-Toyabe function $G^{\rm DGKT}(t;\Delta, H_{\rm LF}, \nu)$).

In this fast fluctuation regime, the relaxation rate (λ) decreases with faster fluctuation rates. This phenomenon is known as the 'motional narrowing' of the T_1 relaxation rate. The longitudinal field dependence of the relaxation rate (λ) is consistent with that of the T_1 relaxation theory [34], which has been developed for nuclear magnetic resonance (NMR).

3.2 Lorentzian theory [7]

The Gaussian Kubo-Toyabe theory introduced above is based on Gaussian local field distribution, which is often realized in dense spin systems. In *dilute* spin systems, such as dilute spin glass alloys, it is known that the dipolar fields from the local moments take a more Lorentzian distribution [38]:

$$\rho_{\rm L}(H_i) = \left(\frac{\gamma_\mu}{\pi}\right)^3 \frac{a}{a^2 + \gamma_\mu^2 H_i^2}, \quad i = x, y, z \qquad (24)$$

$$\rho_{\rm L}(|\boldsymbol{H}|) = \frac{\gamma_\mu^3}{\pi^2} \frac{a}{(a^2 + \gamma_\mu^2 |\boldsymbol{H}|^2)^2} \qquad (25)$$

where a is the width of the Lorentzian field distribution. The origin of the Lorentzian distribution is the large variety of the muon sites relative to the local moments (see Fig.19). Since some muons locate relatively far from the local moments (site A of Fig.19), and some close (site B of Fig.19), the local field distribution has a sharper peak around zero (from site A's) and a broader tail (from site B's) than the Gaussian field distribution.

The Lorentzian distribution width (a) is a calculable quantity, if one knows the concentration of the dilute moments (c) and the hypothetical Gaussian width for the $c = 1$ dense spin system ($\Delta_{100\%}$). In the low concentration regime ($c \lesssim 5\%$), the Lorentzian width

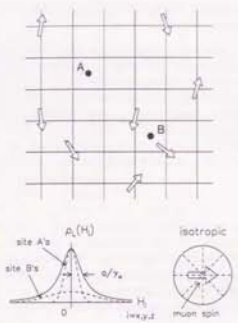

Figure 19:
A dilute spin system. The local field takes an isotropic Lorentzian distribution.

is expressed [7] as:

$$a = \sqrt{\pi/2}\, c\Delta_{100\%} \qquad (26)$$

The static muon spin relaxation for the Lorentzian field distribution has been obtained [39] as:

$$\begin{aligned} & G^{\rm L}(t;a) \\ &= \frac{1}{3} + \frac{2}{3}\int_0^\infty 4\pi H^2 \rho_{\rm L}(H) \cos\gamma_\mu H t dH \\ &= \frac{1}{3} + \frac{2}{3}(1-at)\exp(-at) \end{aligned} \qquad (27)$$

for zero-field, and in the presence of a longitudinal field ($H_{\rm LF}$) [7]:

$$\begin{aligned} & G^{\rm L}(t;a,H_{\rm LF}) \\ &= 1 - \frac{a}{\gamma_\mu H_{\rm LF}} j_1(\gamma_\mu H_{\rm LF} t)\exp(-at) \\ &- \left(\frac{a}{\gamma_\mu H_{\rm LF}}\right)^2 (j_0(\gamma_\mu H_{\rm LF} t)\exp(-at) - 1) \\ &- \left(1 + \left(\frac{a}{\gamma_\mu H_{\rm LF}}\right)^2\right) a \int_0^t j_0(\gamma_\mu H_{\rm LF}\tau)\exp(-a\tau) d\tau \end{aligned} \qquad (28)$$

where the $j_i(x)$ are spherical Bessel functions.

In Fig.20, the static Lorentzian relaxation function $G^{\rm L}(t;a,H_{\rm LF})$ is shown. In zero-field, the relaxation converges to 1/3 of the full amplitude, which is, again, the signature of static relaxation functions. The 'dip' at $at \sim 2$ is shallower and broader than that of the Gaussian Kubo-Toyabe function (Fig.17), reflecting the broadness of the Lorentzian distribution. The relaxation at early times shows an exponential decay, as the result of Fourier transform of the Lorentzian distribution.

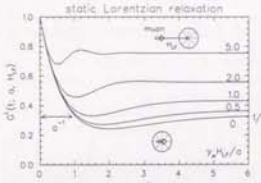

Figure 20:
The muon spin relaxation in the frozen dilute spin system: static Lorentzian Kubo-Toyabe function $G^{\rm L}(t;a,H_{\rm LF})$.

In the presence of field fluctuations, the Lorentzian relaxation function is modulated in a similar manner as the Gaussian Kubo-Toyabe function. Still, one must notice that the Lorentzian distribution results from many *inequivalent* muon sites. A particular muon, which resides at site A (Fig.19), never experiences the local field at site B during the field fluctuation processes. If one is not aware of this point, and applies the strong collision series (eq.21) to the static Lorentzian relaxation function $G^{\rm L}(t;a,H_{\rm LF})$, one obtains an unphysical result: the absence of motional narrowing in the fast fluctuation regime.

The proper treatment to dynamisize the Lorentzian relaxation function is as follows [7]:

(1) Decompose the Lorentzian field distribution to the sum of many Gaussian distributions, each of which represents the local field distribution at an individual muon site.

(2) Obtain the dynamical *Gaussian* Kubo-Toyabe function for each muon site. This treatment reflects the inequivalence of each muon site for the Lorentzian distribution.

(3) Add each contribution, to restore the Lorentzian field distribution.

This procedure has been formulated [7], using a weighting function $\rho_a(\Delta)$, which is the probability of finding a muon site (Gaussian field width: Δ) in a dilute spin system environment (Lorentzian field width:

a). The dynamical Lorentzian relaxation function is obtained:

$$G^{\mathrm{DL}}(t;a,H_{\mathrm{LF}},\nu) = \int_0^\infty G^{\mathrm{DGKT}}(t;\Delta,H_{\mathrm{LF}},\nu)\rho_a(\Delta)d\Delta \quad (29)$$

where,

$$\rho_a(\Delta) = \sqrt{\frac{2}{\pi}}\frac{a}{\Delta^2}\exp\left(-\frac{a^2}{2\Delta^2}\right) \quad (30)$$

This weighting function, by definition, converts a Gaussian distribution to a Lorentzian distribution:

$$\rho_{\mathrm{L}}(H_i) = \int_0^\infty \rho_{\mathrm{G}}(H_i)\rho_a(\Delta)d\Delta,\ i=x,y,z \quad (31)$$

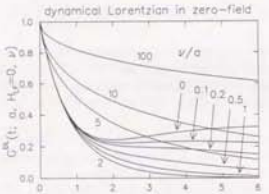

Figure 21:
The zero-field muon spin relaxation in a fluctuating dilute spin system: dynamical Lorentzian relaxation function $G^{\mathrm{DL}}(t;a,H_{\mathrm{LF}},\nu)$.

In Fig.21, the dynamical Lorentzian relaxation function in zero-field $G^{\mathrm{DL}}(t;a,H_{\mathrm{LF}}=0,\nu)$ is shown. The effect of the field fluctuations is similar to that of the Gaussian case: in the slow fluctuation regime, the 1/3-component suffers a slow relaxation as $\sim 1/3\exp(-2\nu t/3)$ [7], and in the fast fluctuation regime, motional narrowing is exhibited. For the Lorentzian distribution, the relaxation in the fast fluctuation regime is approximated by a square-root exponential function [7]:

$$G^{\mathrm{DL}}(t;a,H_{\mathrm{LF}},\nu) \approx \exp(-\sqrt{\lambda t}) \quad (32)$$

with the relaxation rate:

$$\lambda = \frac{4a^2\nu}{\nu^2+(\gamma_\mu H_{\mathrm{LF}})^2} \quad (33)$$

Experimentally, the Lorentzian relaxation function, as well as the square-root exponential behavior in the fast fluctuation regime, have been observed in dilute spin glass alloys [7], and the theory has been quite successful in dilute spin systems.

3.3 A minor correction to the Lorentzian theory[1]

In the previous section, the Lorentzian theory was introduced as a muon spin relaxation theory for dilute spin systems. This theory is based on the Lorentzian field distribution at the muon sites. Still, a truly Lorentzian distribution is unphysical, because some fraction of the muons must locate at an infinitesimally small distance from a magnetic ion, in order to realize the diverging second moment of the Lorentzian distribution $< H_{\mathrm{loc}}^2 > - < H_{\mathrm{loc}} >^2 \to \infty$. To restore the physicality of the local field distribution, it will be natural to introduce a large cut-off field (Δ_{max}) to the Lorentzian distribution. This idea is easily formulated in the Gaussian decomposed picture of the Lorentzian distribution (eq.29,30), which has been introduced to obtain the dynamical Lorentzian relaxation function $G^{\mathrm{DL}}(t;a,H_{\mathrm{LF}},\nu)$.

In this picture, a weighting function $\rho_a(\Delta)$ was introduced to sum up the contributions from every muon sites (see eq.29). In real spin systems, the upper bound of the site-sum integral should be replaced by a cut-off field Δ_{max}:

$$\int_0^\infty d\Delta\rho_a(\Delta) \to \int_0^{\Delta_{\mathrm{max}}} d\Delta\rho'_a(\Delta) \quad (34)$$

where $\rho'_a(\Delta)$ is normalized for the new upper bound Δ_{max}:

$$\rho'_a(\Delta) = \frac{\rho_a(\Delta)}{\int_0^{\Delta_{\mathrm{max}}}\rho_a(\Delta)d\Delta} \quad (35)$$

The physical meaning of the cut-off field Δ_{max} is the largest possible Gaussian field width for the dilute spin system considered. This quantity may be of the same order of magnitude as the hypothetical Gaussian width ($\Delta_{100\%}$), which is expected when all the lattice points are filled up with moments. Since the relation between $\Delta_{100\%}$ and the Lorentzian width (a) has been obtained (eq.26), Δ_{max} is estimated to be:

$$\Delta_{\mathrm{max}} \approx \Delta_{100\%} = \sqrt{\frac{2}{\pi}}\frac{a}{c} \quad (36)$$

where c is the dilute spin concentration and a is the Lorentzian width.

The most significant correction because of the cut-off field Δ_{max} appears in the fast fluctuation regime. In the traditional Lorentzian theory, the relaxation function in this regime is a square-root exponential function (eq.32). When the cut-off field is introduced, the relaxation at large fluctuation rates loses the fast front-end of the square-root exponential behavior, because the fast front-end originates from the T_1 relaxation of

[1]This section is based on the author's original work: K. Kojima, unpublished.

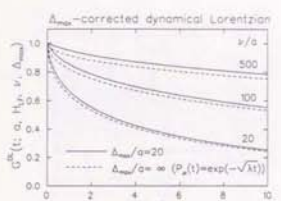

Figure 22:
Δ_{max}-corrected Lorentzian relaxation function for $\Delta_{\mathrm{max}}/a = 20$ (solid lines). The dotted lines are square-root exponential functions ($\exp(-\sqrt{\lambda t})$), which is realized in the ideal Lorentzian field distribution.

muons which locate at sites with large local fields. In Fig.22, the Δ_{max}-corrected dynamical Lorentzian functions $[G^{\mathrm{DL}}(t;a,H_{\mathrm{LF}},\nu,\Delta_{\mathrm{max}})]$ are compared with the square-root exponential functions of the ideal case.

The Δ_{max}-corrected dynamical Lorentzian function is well approximated by a 'stretched' exponential function, $\exp(-(\lambda t)^\beta)$; in Fig.23, the stretching power (β) is shown as a function of the normalized fluctuation rate (ν/a). At small fluctuation rates, the power converges to 1/2, as expected for the square-root exponential behavior, and in the large fluctuation limit, β approaches 1.

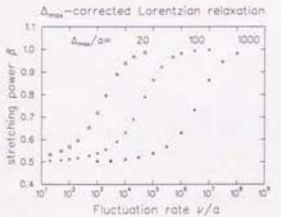

Figure 23:
Stretching power β derived from the stretched exponential function fit to the Δ_{max} corrected relaxation function.

Experimentally, muon spin relaxation in paramagnetic dilute spin systems often exhibits a stretched exponential behavior, with its power β approaching 1 at high temperatures [40]. The above mentioned cut-off field effect may explain at least part of the phenomena.

3.4 Summary of the Kubo-Toyabe theories

As a concluding remark concerning the zero/low-field spin relaxation theories, I will mention the importance of the longitudinal field measurements when using the μSR technique as a local magnetic probe. In Fig.24, the simulated muon spin relaxation in two different spin systems are shown. One is a dense spin system with fast fluctuations, and the other is a dilute spin system with slow fluctuations. In zero-field, the two systems presents almost identical exponential relaxation, and the two situations are indistinguishable. In longitudinal field measurements, however, these two systems become distinguishable. In the slowly fluctuating system, the relaxation is decoupled with relatively small longitudinal fields, which are comparable to the field distribution width (Fig.24b). In the fast fluctuating system (Fig.24a), decoupling requires much larger fields. These qualitatively different responses to the applied longitudinal fields allow one to experimentally distinguish between slow and fast fluctuations of the local fields.

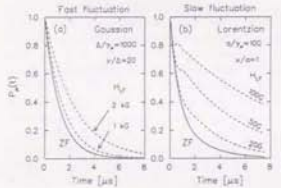

Figure 24:
(a) Muon spin relaxation in a fast fluctuating dense spin system: $G^{\mathrm{DGKT}}(t;\Delta,H_{\mathrm{LF}},\nu)$, and (b) in a slowly fluctuating dilute spin system: $G^{\mathrm{DL}}(t;a,H_{\mathrm{LF}},\nu)$. These two systems are distinguishable in longitudinal field measurements, but not in zero-field.

In the following chapter, the μSR technique is applied to a spin-ladder material, $Sr_{n-1}Cu_{n+1}O_{2n}$. The set of measurements presented there will exhibit how Kubo-Toyabe theories help us investigate the magnetism of this material.

4 Spin-ladder system†

This chapter reports our μSR measurements of the spin-ladder cuprates $Sr_{n-1}Cu_{n+1}O_{2n}$ (n=3, 5). The measurements have revealed contrasting magnetic behaviors between the '2-leg' (n=3) and the '3-leg' (n=5) spin-ladder materials, which qualitatively agree with the theoretical predictions. The results presented in this chapter, in addition, provide a good example of how μSR detects the existence/absence of magnetic order.

4.1 Introduction

The first discovery of a high-T_c superconductor in 1986 [41] initiated a surge of interest in new materials which have a higher superconducting transition temperature (T_c). As a result of vital experimental researches, various copper oxides, doped with charges, have been identified as a high-T_c superconductor. One remarkable structural similarity among these high-T_c cuprates is the existence of the CuO_2 planes, and there have been many theoretical studies trying to explain the superconductivity as a nature of the doped CuO_2 square lattice. Still, the problem of correlated electrons on the two-dimensional lattice is difficult, and no rigorous solution to the problem has been found.

For the one-dimensional chain system, on the other hand, quite a few things are known exactly. For example, the antiferromagnetic Heisenberg model of the S=1/2 spin-chain was exactly solved by H. A. Bethe in 1931 [11], and using a similar technique, the one dimensional Hubbard model, as well as the t–J model in special cases (J=0 and 2t) have also been solved [42, 43]. Considering these successes in one-dimensional systems, one approach to tackle the superconducting cuprates is to investigate the quasi one-dimensional lattices known as 'spin ladder' structures (Fig.25a), which are strips of square lattice with a finite width and infinite length.

Early theoretical works of the spin ladder system were numerical studies on isolated 2-leg spin ladders. For the Heisenberg model of a 2-leg spin ladder, a many-body singlet ground state was suggested, with a finite energy gap (spin-gap) to the excited states [20, 44]. The ground state structure is mainly composed of spin singlet pairs on the rungs, as shown in Fig.25b [20]. The hole doped 2-leg ladders have also been investigated theoretically, in relation to the superconductivity [45, 46, 47]. These works suggest that two doped holes will form a bound state so that the surrounding spins can remain spin singlet. The paired holes, which behave as hard-core bosons, were suggested to take a superconducting ground state [45, 46].

†Most of the content of this chapter has been published as K. Kojima *et al.*, Phys. Rev. Lett. **74**, 2812 (1995)

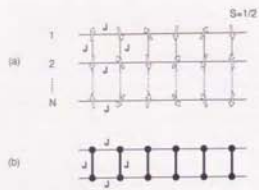

Figure 25:
(a) The N-leg spin ladder structure and (b) a schematic ground state of the 2-leg spin ladder system.

Behavior of wider spin-ladder systems was first emphasized by T. M. Rice *et al.* in 1993 [19]. In Ref. [19], the authors first pointed out that the homologous series of cuprate $Sr_{n-1}Cu_{n+1}O_{2n}$ should realize the N-leg ladder structure, and pointed out contrasting magnetic behavior between the even-number-leg ladders and the odd-number-leg ladders. The even-number-leg ladders were to manifest a spin-gap, while the odd-number-leg system should be gapless. This idea of alternating ground states has been supported by numerical simulations of the spin ladders up to 4-legs [48] and a mean-field calculation of the 2-leg and the 4-leg ladder systems [21].

4.2 Spin-ladder material $Sr_{n-1}Cu_{n+1}O_{2n}$

The spin-ladder material $Sr_{n-1}Cu_{n+1}O_{2n}$, which is synthesized under high pressure and high temperature [49, 50], takes the structure shown in Fig.26a. The lattice structure is composed of $(n+1)/2$-leg spin-ladders, namely, strips of CuO_2 square lattice which have $(n+1)/2$- Cu^{2+} ions across their width. Each Cu^{2+} ion has spin S=1/2 with antiferromagnetic couplings within a ladder (strength: J), both in the 'rung' and the 'leg' directions. In the two directions, the difference of the coupling strengths are presumably small, because the 180° Cu-O-Cu bond lengths are almost equal for both directions [49].

In this material, the neighboring ladders are displaced by half the lattice constant, leading to a small inter-ladder interaction. Since the 90° Cu-O-Cu bonds mediate the inter-ladder interaction, the interaction may be ferromagnetic ($-J'$; see Fig.26b). The magnitude of the inter-ladder interaction has been theoretically estimated as $J'/J \approx 0.1-0.2$ [19, 21]. The inter-ladder interaction brings about a geometrical frustration of the spins at the edge of the ladders, because of the triangular structure constituent of two ferromagnetic interactions ($-J'$) and one antiferromagnetic interaction (J) [19, 21].

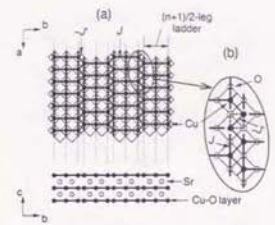

Figure 26:
(a) The 'spin ladder' structure of $Sr_{n-1}Cu_{n+1}O_{2n}$. Oxygen ions locate at each corner of the squares. The figure shows the 3-leg ladder structure (n=5). (b) A magnified ladder-edge. The dotted lines represent the 90° Cu-O-Cu bonds which mediate the ferromagnetic inter-ladder interaction ($-J'$).

Previous investigations of $Sr_{n-1}Cu_{n+1}O_{2n}$ have measured magnetic susceptibility (Fig.27; [51]) and ^{63}Cu-NMR (Fig.28; [52]). In the 2-leg ladder system (n=3), the temperature dependence of the susceptibility and the T_1 relaxation rate are well described by thermal excitations over a gap, which may correspond to the spin gap between the non-magnetic ground state and magnetic excited states. The magnitude of the gap has been reported as 420 K (susceptibility: [51]) and 680 K (^{63}Cu-NMR: [52]).

The 3-leg ladder system (n=5), in contrast, has a finite susceptibility in the $T \to 0$ limit, demonstrating that the ground state of this system can respond to the external magnetic field. Therefore, the ground state may exhibit magnetic order. In the 3-leg ladder system, the T_1 relaxation rate of ^{63}Cu nuclear moments was so large that it was hardly measurable with the conventional NMR technique. This result implies the existence of strong magnetic correlations in the 3-leg system [52].

As introduced in Chapter 2, continuous-beam muon spin relaxation (μSR) is a NMR-like local magnetic probe, but with a higher timing resolution ($\lesssim$1 ns) than typical NMR methods ($\sim$10 μs). Consequently, μSR is an adequate probe to study the 3-leg ladder system, in which the NMR relaxation rate was beyond its time resolution. Another advantage of μSR is its high sensitivity to small and/or dilute static moments. Using μSR one can best investigate the expected absence of static order in the 2-leg ladder system.

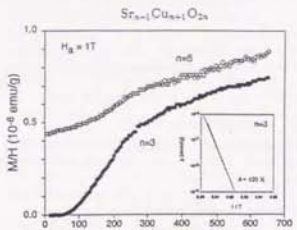

Figure 27:
Susceptibility of the spin ladder materials $Sr_{n-1}Cu_{n+1}O_{2n}$. Cite from Ref. [51].

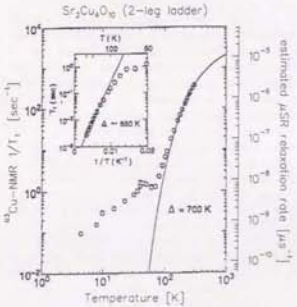

Figure 28:
Temperature dependence of the ^{63}Cu-NMR T_1 relaxation rate (cite from [52]). The right axis is an estimated muon spin relaxation rate for the same relaxation mechanism. (See the discussion later.)

For our μSR measurements, polycrystalline specimens of the spin ladder cuprates ($Sr_{n-1}Cu_{n+1}O_{2n}$; n=3, 5) were prepared at the Institute for Chemical Research, Kyoto University, using a cubic anvil-type

high pressure apparatus [53]. Powder X-ray analysis of our samples showed the stoichiometric ladder structure, except for small amounts (~10 Cu at.%) of a CuO impurity phase [51]. Since CuO is an antiferromagnet (T_N~230 K [54]), the impurity phase should not affect the muons which did not land within an impurity cluster. Therefore, in our μSR measurements ~90% of the signal amplitude comes from the pure ladder structure.

4.3 μSR measurements

We performed μSR measurements at M15 and M13 beamlines at TRIUMF, using the counter configurations for the LF/ZF-μSR measurements (Fig.14a). Detailed technical aspects of the μSR method have been described in Chapter 2.

4.3.1 The 3-leg ladder material (n=5)

Zero-field measurements

Fig.29a shows typical zero-field μSR spectra in the 3-leg ladder system. Below ~55 K, there observed muon spin relaxation, which suggests a magnetic order of the Cu moments. The signal amplitude was large enough to conclude that it comes from the ladder structure, rather than from the CuO impurity phase. The spectra below 45 K converge to 1/3 of the total amplitude; this '1/3-component' is a signature of static order in polycrystalline specimens (see section 3.1). The spectra below 30 K exhibited a 'dip' between the initial decay and the 1/3-component; the existence of such a dip is another signature of a static order. The solid line for the 50 mK data is a phenomenological fit with the Gaussian Kubo-Toyabe function, which is appropriate to randomly oriented, frozen dense spin systems (see section 3.1).

The spectra near the transition temperature (Fig.29a) behave as if there is a distribution of ordering temperatures: (1) the relaxation amplitude ($\propto$ ordered volume fraction) decreases as temperature increases and (2) the 'dip' in the spectra disappears above ~40 K, although the relaxation is static as shown by the decay to the 1/3-component. The absence of the dip in the static relaxation suggests a distribution of the field-widths (Δ), which would result from a distribution in the ordering temperatures. We analyzed the μSR spectra with a functional form of:

$$P_\mu(t) = f_{\rm para} + (1 - f_{\rm para}) G_{\rm static}(t;\Delta) \qquad (37)$$

where $f_{\rm para}$ is the paramagnetic volume fraction in the sample and $G_{\rm static}(t;\Delta)$ is the static Gaussian Kubo-Toyabe function at $T \leq 30$ K or a static Gaussian function $(1/3 + 2/3\exp(-(\Delta t)^2))$ at $T \geq 40$ K. The parameter Δ is the Gaussian field distribution width, which is proportional to the size of the ordered Cu moments. At

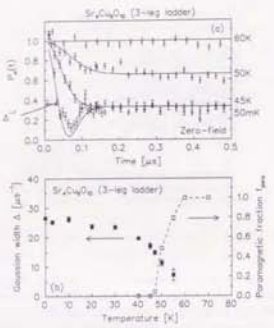

Figure 29:
a: Zero-field μSR spectra in the 3-leg ladder system. The solid lines are the fit with the model function, eq.(37). b: Temperature dependence of the Gaussian field-distribution width (Δ) and the paramagnetic volume fraction ($f_{\rm para}$). The broken line is a guide to the eye.

$T \geq 40$ K, Δ represents an 'average' of the field-widths at the muon sites. We show the temperature dependence of $f_{\rm para}$ and Δ in Fig.29b. The ordering temperature is around 52 K with a distribution of ± 5 K, as deduced from the temperature dependence of $f_{\rm para}$.

Longitudinal-field measurements

In Fig.30, we show μSR spectra from longitudinal field (LF) decoupling measurements, which investigate fluctuations of the internal fields (see section 3.4). The spectra in longitudinal fields clearly demonstrate the static nature of the muon relaxation, being consistent with the observation of the '1/3-component' and the 'dip' in the zero-field measurements. The recoveries of the muon spin polarization in LF's are well described by the static Gaussian Kubo-Toyabe theory (solid lines in Fig. 30), which seems to imply a random freezing of moments, rather than true Néel order. However, as a local probe, the μSR results can not exclude the possibility of long range spin correlations. When there is a distribution of T_N, the muon spin precession is sometimes smeared out because of the distribution in the local fields (See the discussion in Chapter 6 for an example.) Therefore, we just propose an existence of a *static order* at $T \sim 52$ K in the 3-leg ladder system.

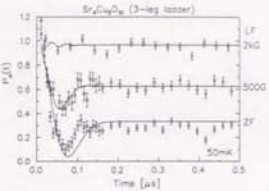

Figure 30:
Longitudinal field (LF) decoupling measurements of the 3-leg ladder system at 50 mK. The solid lines are the fit with static Kubo-Toyabe functions (eq.19).

Discussion

We compare in Table 3 the ordering temperatures of the Sr(Ca)-Cu-O series of compounds, which is a one-dimensional chain system for Sr_2CuO_3 [55], and a two-dimensional layer system for $Ca_{0.86}Sr_{0.14}CuO_2$ ($n \to \infty$ structure of the spin-ladder series) [56]. The ordering temperature of the 3-leg ladder system is between those of the chain system (Sr_2CuO_3) and the layer system ($Ca_{0.86}Sr_{0.14}CuO_2$). Suppression of T_N in the chain system has been explained as an effect of the low-dimensionality [55]; the intermediate ordering temperature for the 3-leg system is consistent with this idea, because the 3-leg ladder structure is the smallest extension of the one-dimensional chain toward two-dimensionality.

Table 3: Structure and magnetic behavior of Sr(Ca)-Cu-O compounds

compound	structure	magnetic order
Sr_2CuO_3	CuO chain (1D)	T_N~5 K[a]
$Sr_4Cu_6O_{10}$	3-leg ladder	T~52±5 K[b]
$Ca_{0.86}Sr_{0.14}CuO_2$	CuO_2 plain (2D)	T_N~540 K[c]

[a]Obtained by μSR [55].
[b]Obtained by μSR: this work [1].
[c]Obtained by neutron scattering [57] and μSR [55].

Another feature of the magnetic order in the 3-leg ladder system is the absence of critical slowing down of the Cu moments in the μSR time window (~ 10μs). In Fig.31, we show μSR spectra at long times. No enhancement of the relaxation rate was observed around the transition temperatures. This 'abrupt' onset of magnetic order has been observed in other one-dimensional systems, such as antiferromagnets Sr_2CuO_3 [55], Ca_2CuO_3 [58] and a spin-density-wave system $(TMTSF)_2$-PF_6 [59]. In these systems, the absence of critical slowing down have been explained as follows; in one-dimensional systems, the ordering temperature is determined by the small inter-chain interactions, and therefore, there may be preformed short-range ordered regions before the three-dimensional order takes place [60]. Then the ordering process is a phase-lockings of these short-range ordered regions, which do not involve a slowing down of the moments. The absence of the critical slowing down in the 3-leg ladder system may also reflect its low-dimensionality, if the 'phase-locking' picture of the magnetic order is relevant.

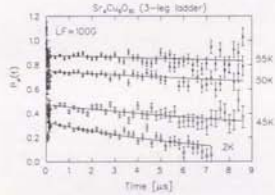

Figure 31:
LF=100 G μSR spectra around the transition temperatures.

4.3.2 The 2-leg ladder material (n=3)

Zero- and longitudinal-field measurements

The magnetic behavior of the 2-leg ladder system differs markedly from that of the 3-leg system. In Fig.32a, we show typical μSR spectra in the 2-leg ladder system. Note that Fig.32 has a horizontal scale about 10 times larger than that for Fig.29a and Fig.30. In the 2-leg system, weak relaxation below ~50 K was observed. However, from the longitudinal field (LF) measurements (Fig.32b), the source of this relaxation was found to be fluctuating rather than static internal fields. If the slow relaxation in the zero-field measurement were due to a static field distribution, the characteristic field distribution width would be $\delta H \sim 10$ G, as the relaxation rate suggests. In this case, the μSR spectrum would be flattened in a LF~100 G. As shown in Fig.32b, the relaxation persists up to LF~2 kG, proving that this slow relaxation is a T_1-like dynamical one (see section 3.4).

We analyzed the muon spin relaxation in the 2-leg ladder system using a square-root exponential function

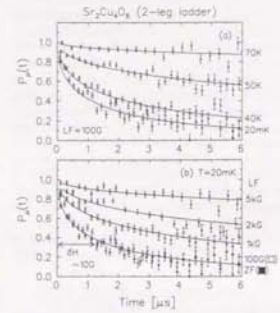

Figure 32:
a: LF=100 G μSR spectra in the 2-leg ladder system. b: Longitudinal field decoupling measurements at 20 mK. For both panels the solid lines are fits with a square-root exponential function. Note that the horizontal scale is ~10 times larger than that in Fig.29a and Fig.30.

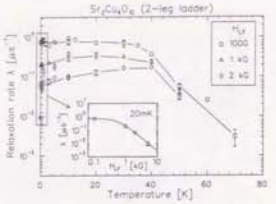

Figure 33:
Temperature dependence of muon spin relaxation rate (λ) in the 2-leg ladder system. The solid lines are guide to the eye. The inset is the longitudinal field dependence of the relaxation rate at 20 mK, with the fit to the T_1 relaxation theory (eq.33).

$(P_\mu(t)=\exp(-\sqrt{\lambda t}))$, which is appropriate for dilute fluctuating moments (see section 3.2). The temperature dependence of the relaxation rate (λ) is shown in Fig.33. The increase of λ down to ~40 K indicates a slowing down of field fluctuations. Still the field fluctuations persists down to the milli-Kelvin regime, as shown by the saturation of λ. This result indicates that there is no static order in the 2-leg ladder material, supporting the theoretical expectations for the non-magnetic ground state of this system.

Discussions

Comparing the temperature dependence of the muon T_1 relaxation rate (Fig.33) with that of ^{63}Cu-NMR (Fig.28), one question may arise: why the temperature dependence is *opposite* between μSR and NMR. In the NMR measurements, the T_1 relaxation increased at higher temperatures, as has been ascribed to the excitation over the spin gap, while in μSR, it decreased as shown in Fig.33. As discussed below, the qualitatively different temperature dependence of the T_1 relaxation rates may be attributed to the different scales of the experimental time windows.

The time window of the μSR method is typically $1\,\mathrm{ns} - 10\ \mu\mathrm{s}$, and for NMR, it is $100\ \mu\mathrm{s} - 10^3$ s. Therefore, in the paramagnetic fluctuation regime, NMR is more capable of detecting faster fluctuations than μSR. As has been shown by gap excitation type temperature dependence [52], the ^{63}Cu nuclear spin relaxation is most likely caused by magnetic excited states which produce fast field fluctuations. From a simple scaling argument below, these excited states do not cause fast enough muon spin relaxation detectable in the μSR time window.

The only difference between the muon spin relaxation and the ^{63}Cu nuclear spin relaxation is the gyromagnetic ratio of the probe spins (γ_μ and γ_{Cu}) and the electron-nuclear spin coupling strength, which reflects the probe spin site. From previous Knight-shift and susceptibility measurements, the hyperfine coupling parameter between a ^{63}Cu nuclear spin and electron moments has been obtained as [52]:

$$\begin{aligned} A_c &= -120\ [\mathrm{kOe}/\mu_B] \\ A_{ab} &= 48\ [\mathrm{kOe}/\mu_B] \end{aligned}$$

where the suffix (c and ab) indicates the crystalline orientation of the parameter. The coupling between a muon spin and the electron moments is probably a dipolar coupling, and its magnitude can be estimated from the static field-width of the ordered *3-leg* ladder system (Fig.29):

$$\begin{aligned} \Delta(T\to 0)/\gamma_\mu &= \frac{26\ [\mu\mathrm{s}^{-1}]}{2\pi \times 13.554\ [\mathrm{MHz/kOe}]} \\ &= 0.305\ [\mathrm{kOe/size\ of\ ordered\ moments}] \end{aligned}$$

The gyromagnetic ratio of the two probe spins are [28, 61]:

$$\begin{aligned} \gamma_\mu &= 2\pi \times 13.554\ [\mathrm{MHz/kOe}] \\ \gamma_{Cu} &= 2\pi \times 1.1285\ [\mathrm{MHz/kOe}] \end{aligned}$$

Using these parameters and the T_1 relaxation formula [34], the scaling factor of the muon/^{63}Cu T_1 relaxation rates is estimated as:

$$\begin{aligned} &\frac{T_1^{-1}(\mu)}{T_1^{-1}(^{63}\mathrm{Cu})} \\ &= \frac{\gamma_\mu^2(\Delta/\gamma_\mu)^2(\gamma_e\hbar)^2\int_{-\infty}^{\infty} < S(0)S(t) > e^{-i\gamma_\mu H_I t}dt}{\gamma_{Cu}^2 A^2(\gamma_e\hbar)^2\int_{-\infty}^{\infty} < S(0)S(t) > e^{-i\gamma_{Cu} H_I t}dt} \\ &\approx \left(\frac{\Delta/\gamma_\mu}{A_{ab}}\right)^2\left(\frac{\gamma_\mu}{\gamma_{Cu}}\right)^2 \\ &= 5.6\times 10^{-3} \end{aligned} \tag{38}$$

Since the ^{63}Cu T_1 relaxation rate in the 2-leg ladder system is $\lesssim 4\times 10^2\ [\mathrm{sec}^{-1}]$ (Fig.28), the corresponding muon spin relaxation rate should be $\sim 2\times 10^{-6}\ [\mu\mathrm{s}^{-1}]$ at room temperature, and smaller at lower temperatures (see the right axis of Fig.28). These relaxation rates are too small for the μSR time window, and therefore, the magnetic excited states do not contribute to the muon spin relaxation.

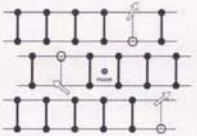

Figure 34:
Possible muon spin relaxation mechanism. The unpaired spins associated with the defects may cause muon spin relaxation.

Then, what would be a relevant relaxation mechanism for the muon spins? One possible scenario is that the muons detect the unpaired spins which are related to vacancies and defects in the system (Fig.34). From susceptibility measurements, the amount of native unpaired moments has been estimated as ~0.26 at.% of the copper ions [51]. The idea of the relaxation from the unpaired moments qualitatively explains the general temperature and longitudinal field dependence of the muon relaxation rate; since the couplings between the unpaired spins are presumably small, these spins should remain paramagnetic down to the milli-Kelvin regime, giving a temperature-independent relaxation rate ($T \lesssim 40$ K in Fig.33). At higher temperatures, the unpaired spins may have additional fluctuations related to the magnetic excited states; in this situation, the muon spin relaxation rate should decrease, and respond less to the longitudinal fields (see data at $T \gtrsim 40$ K in Fig.33), reflecting more dynamic local fields.

As shown in the inset of Fig.33, we analyzed the LF dependence of muon spin relaxation rate $\lambda(T\to 0)$ with the T_1 relaxation formula in dilute spin systems (eq.33). The resulting Lorentzian field width (a) and the field fluctuation rate (ν) are shown in Table 4. In the same table, estimates of these parameters are given, which are based on the unpaired spin concentration from the susceptibility measurements (see the caption of Table 4 for detail.) Although the quantitative agreement between the estimates and the experimental results is poor, it is worth while to point out that the unpaired spins assumed here will induce a muon spin relaxation rate ($\lambda = 4a^2/\nu \approx 5.7\times 10^{-3}\ \mu\mathrm{s}^{-1}$) which is in the time range of μSR measurements. Therefore, the scenario of muon spin relaxation from the unpaired spins is better than that from the excited states. See the concluding remark at Chapter 7 for more discussions.

Table 4: The parameters in the T_1 relaxation fit (2-leg ladder, 20 mK)

Parameter	Experiment	Estimate (native spins)
$a\ (\mu s^{-1})$	3.1(1)	0.085[a]
ν (MHz)	51(6)	5.08[b]

[a] An estimate using eq.26. For the calculation, the hypothetical Gaussian width (Δ_{100K}) with all the spin-cites filled with static moments was taken as the Gaussian width observed in the ordered 3-leg ladder system ($\Delta(T\to 0) \approx 26\ \mu\mathrm{s}^{-1}$; see Fig.29b). The unpaired spin concentration ($c = 0.26\%$) has been estimated from the susceptibility measurements [51]. [b] The dipolar fluctuation rate of the unpaired spins, which is $\sim 60\ (\approx \sqrt{10/3}/2\pi \times \gamma_e/\gamma_\mu)$ times larger than the Lorentzian width (a). See the discussion in Chapter 5 for more details of the estimation procedure.

4.4 Summary

From the μSR measurements of the spin-ladder material $Sr_{n-1}Cu_{n+1}O_{2n}$, we observed static magnetic order for the 3-leg ladder system at $T\sim 52$ K, while, in the 2-leg ladder system, no magnetic order was present down to 20 mK. Our results support the theoretical expectations of the magnetic ground states of the ladder systems, namely, a non-magnetic ground state for the 2-leg ladder system, and a magnetic ordered state for the 3-leg ladder system.

5 Haldane system†

This chapter contains our μSR and susceptibility measurements for the Haldane material, Y_2BaNiO_5. First, in the nominally pure system, the absence of magnetic order was confirmed with the ZF/LF-μSR measurements down to 100 mK. Second, the effects of charge doping ($Y^{3+}\rightarrow Ca^{2+}$) and vacancy doping ($Ni^{2+}\rightarrow Mg^{2+}$) were investigated. The charge doped system exhibited a spin-glass like behavior in the susceptibility, while our μSR measurements revealed unconventional spin dynamics in the milli-Kelvin regime. In the vacancy doped systems, the non-magnetic ground state survives.

5.1 Introduction

5.1.1 Haldane's prediction

The antiferromagnetic Heisenberg model, which assumes an isotropic interaction between neighboring spins, is the most fundamental model of localized antiferromagnetic spin systems. Its Hamiltonian is written as:

$$\mathcal{H} = \sum_{<i,j>} \boldsymbol{S}_i \cdot \boldsymbol{S}_j \qquad (39)$$

where $< i, j >$ represents all the nearest neighboring spin pairs.

In classical mechanics, the spin $\boldsymbol{S}_i$ is a three dimensional vector (S_i^x, S_i^y, S_i^z) with a fixed length $|\boldsymbol{S}_i|$=S. If the lattice structure is decomposed into two sublattices without frustration, the ground state of the classical Heisenberg model is the Néel state, in which all the spins on one sublattice point in one direction, and all the spins on the other sublattice point in the opposite direction.

In quantum mechanics, the spin $\boldsymbol{S}_i$ is represented by a set of three operators, which satisfies the commutation rules of angular momenta. The Heisenberg Hamiltonian is then rewritten as follows, using the raising and lowering operators of the spins (S_i^+, S_i^-):

$$\mathcal{H} = \sum_{<i,j>} \left(\frac{1}{2}(S_i^+ S_j^- + S_i^- S_j^+) + S_i^z S_j^z \right) \qquad (40)$$

It is easy to show that the Néel state is *not* an eigenstate of this Hamiltonian, because of the spin-flip terms $S_i^+ S_j^-$ and $S_i^- S_j^+$. In order to obtain the ground state rigorously, one has to treat the Hamiltonian as a quantum mechanical operator.

In the investigations of the antiferromagnetic Heisenberg model, the one-dimensional chain of S=1/2 spins was the first system to be solved exactly. Based on an *ansatz*, all the eigenstates were obtained by H. A. Bethe in 1931 [11]. Bethe's ground state is (1) a many-body spin singlet, and has (2) no energy-gap to the excited states and (3) the spin correlations decay slowly as a power-law of distance. The lowest triplet excitation of the S=1/2 system was rigorously expressed by J. des Cloizeaux and J. J. Pearson, as $\epsilon(k) = \pi/2\,|J||\sin(k)|$ [13], where k is the momentum along the chain. Since this excitation curve has the same shape as the classical spin wave dispersion $\epsilon(k) = |J||\sin(k)|$, it was implied that the behavior of the Heisenberg model with larger S smoothly converges to the classical case.

Contrary to this expectation, F. D. M. Haldane conjectured in 1983 [22, 23] that the ground state of the Heisenberg model strongly depends on the value of S. He predicted that half-odd-integer spin systems preserve the features of the S=1/2 spin-chain, but *integer* spin chains have the following features:

(1) The ground state is unique.

(2) There exists a large energy gap (Haldane gap) between the ground state and the excited states.

(3) The spin correlation function quickly decays as an exponential function.

Among Haldane's conjectures about the integer spin systems, the existence of the gap (2) is most surprising, because it seems always to be possible to make low energy excitations, such as spin-waves, for rotationally invariant Hamiltonians like the Heisenberg model (eq.39). Actually, the absence of the spin-gap had been proved in the 'Lieb-Shultz-Mattis theorem' [62] for the S=1/2 Heisenberg model. This theorem was extended to larger spin values S, but the gapless feature was proved only for the half-odd-integer spin systems [8] (see section A.1). Namely, the extended Lieb-Shultz-Mattis theorem could not eliminate the possibility of the Haldane gap.

Although there has been no rigorous proof of Haldane's conjectures for the integer-spin Heisenberg model, there is an antiferromagnetic Hamiltonian describing an S=1 spin chain, which was rigorously proved to have the features of the Haldane system.

5.1.2 The Valence-Bond-Solid Hamiltonian

In 1987, I. Affleck, T. Kennedy, E. H. Lieb and H. Tasaki proposed a Hamiltonian for S=1 spins [24]:

$$\mathcal{H}_{\rm VBS} = \sum_i \left(\boldsymbol{S}_i \cdot \boldsymbol{S}_{i+1} + \frac{1}{3}(\boldsymbol{S}_i \cdot \boldsymbol{S}_{i+1})^2 \right) \qquad (41)$$

which is the antiferromagnetic Heisenberg model modified by a biquadratic second term. The authors of Ref. [24, 25] rigorously obtained the ground state, which has an exponentially-decaying correlation function and a finite energy gap to the excited states. The exact ground state, which is known as 'Valence Bond Solid state', is constructed as follows:

†Most of the contents of this chapter have been published as K. Kojima *et al.*, Phys. Rev. Lett. **74**, 3471 (1995) and K. Kojima *et al.*, J. Mag. Mag. Matrs. **140-144**, 1657 (1994)

(1) decompose the S=1 spins at each site into two S=1/2 spins (Fig.35a)

(2) make singlet bonds between adjacent S=1/2 spins (Fig.35b)

(3) symmetrize the two S=1/2's on each site to restore the S=1 degrees of freedom (Fig.35c).

The VBS ground state is non-magnetic singlet in nature, as it is built from many singlet pairs. From numerical calculations of the VBS Hamiltonian (eq.41) with arbitrary magnitudes of the biquadratic term ($1/3\rightarrow\beta$), it has been shown that the non-magnetic ground state of the pure Heisenberg model ($\beta = 0$) belongs to the same category as the VBS ground state [63, 64].

Another characteristic of the VBS state appears when a spin site is substituted with a foreign ion (Fig.35d). The foreign ion breaks two singlet pairs, and introduces two S=1/2 paramagnetic spins. The S=1/2 degrees of freedom have actually been observed in electron spin resonance (ESR) measurements of a Haldane material NENP (see section 5.1.4).

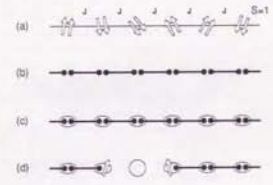

Figure 35:
(a) S=1 antiferromagnetic spin chain. Each S=1 spin is decomposed into two S=1/2 spins. (b) Singlet pairing of the adjacent S=1/2 spins. (c) The Valence Bond Solid (VBS) state. The two S=1/2 spins on each lattice point are symmetrized to restore S=1. (d) The VBS state doped with a foreign ion.

5.1.3 Physical Hamiltonians

Since real materials may not realize the ideal Heisenberg model, more general spin Hamiltonians have been investigated, mainly with numerical simulations [65, 66, 67, 68]. From these works, a phase diagram has been obtained for the Hamiltonian with the XXZ-type interaction and a uniaxial single ion anisotropy D:

$$\mathcal{H} = \sum_i \left((S_i^x S_{i+1}^x + S_i^y S_{i+1}^y + \lambda S_i^z S_{i+1}^z) + D(S_i^z)^2 \right) \qquad (42)$$

The phase diagram is shown in Fig.36 [68]. It has been found that the Haldane phase (H) exist in a relatively large parameter region, which includes the pure Heisenberg model ($\lambda = 1$, $D = 0$).

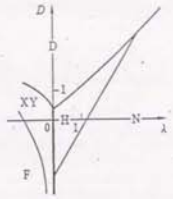

Figure 36:
Phase diagram of the Hamiltonian eq.42 is shown (cite from [68]). The symbols are: (H) Haldane phase, (N) Néel ordered phase, (XY) XY phase, (F) Ferromagnetic phase and (D) large-D phase.

The effect of the inter-chain interactions has also been investigated [69, 70, 71]. Fig.37 shows the phase diagram [71] obtained from a numerical simulation of the Hamiltonian:

$$\mathcal{H} = \sum_i (\boldsymbol{S}_i \cdot \boldsymbol{S}_{i+1} + D(S_i^z)^2) + J' \sum_{\langle i,j \rangle} \boldsymbol{S}_i \cdot \boldsymbol{S}_j \qquad (43)$$

where $\langle i, j \rangle$ denotes the nearest inter-chain neighboring pair. It has been found that the Haldane phase (H) survives in the presence of the inter-chain interaction (J'), if the single ion anisotropy (D) is small.

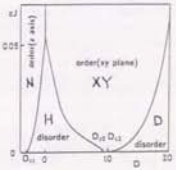

Figure 37:
Phase diagram of the Hamiltonian (eq.43) is shown (cite from [71]). The symbols are: (H) Haldane phase, (N) Néel ordered phase, (XY) XY phase, and (D) large-D phase.

The above introduced theoretical works all supported Haldane's conjecture. The next section introduces previous experimental results of several S=1 spin systems.

which were studied to test Haldane's conjecture in real materials.

5.1.4 Experimental evidence for Haldane's conjecture

The first material investigated to test Haldane's conjecture was a hexagonal ABX_3-type material $CsNiCl_3$. With inelastic neutron scattering measurements [72, 73, 74], an energy gap was observed above the Néel temperature T_N=4.9 K. The authors identified the observed energy gap as the Haldane gap, but the existence of 3D Néel order made a clear conclusion difficult.

Another model material $Ni(C_5H_8N_8)_2NO_2(ClO_4)$ (NENP) was reported by J. P. Renard *et al.* in 1987 [75]. Since the absence of Néel order was reported down to 1.2 K in the first paper [75], various measurements have been performed on this compound, most of which looked for the Haldane gap.

Susceptibility [75, 76, 77, 78]

The temperature dependence of the magnetic susceptibility (χ) was well described by the thermal excitation over an energy gap ($\chi \approx \exp(-E_g/kT)$; $E_g \approx 17$ K). Avenel *et al.* [78] measured χ down to 0.3 mK and confirmed the absence of a magnetic order to the milli-Kelvin regime.

High-field magnetization [79, 80]

The magnetization of NENP at 1.3 K was small and almost field independent up to a critical field $H_c \sim 9.5$ T, and above H_c, linearly increased. This phenomenon was attributed to the crossover in the field between the singlet ground state and one of the triplet excited states. The Haldane gap ($E_g \approx 17$ K) and the single ion anisotropy ($D \approx 16$ K) were obtained from the critical field and its crystalline axis dependence.

Neutron scattering measurements [75, 76, 81, 82, 83]

The first report [75] presents two energy gaps at $k = \pi$ ($E_g^{xy} \approx 1.1$ meV and $E_g^z \approx 2.5$ meV).

The work by Regnault *et al.* [82] is very detailed; the high energy-resolution measurements resolved the lower energy gap (E_g^{xy}) to two gaps ($E_g^y \approx 1.05$ meV and $E_g^x \approx 1.23$ meV); magnetic fields (up to 10 T) shifted the gap energies, as expected for a triplet state; a Lorentzian and/or square-root Lorentzian correlation function was observed with the finite correlation length ($\xi_{xy}/d \approx 8$ and $\xi_z/d \approx 4$). They concluded that the observed gaps were well understood as the Haldane gap of an anisotropic S=1 spin chain.

Nuclear magnetic resonance (NMR) [84, 85, 86, 87]

The temperature dependence of the proton T_1 relaxation rate was also well described by excitations over an energy gap, as $T_1^{-1} \propto \exp(-E_g/kT)$ [85, 86, 87]. Fujiwara *et al.* [87] reported that the field dependence of the gap (E_g) agreed well with that of the gap observed in the neutron scattering measurements [82]. Below 4 K, the T_1 relaxation rate took a maximum at around the critical field ($H_c \sim 9.5$ T). This is because the external field brought the first excited state to the zero-energy, maximizing the spectral density responsible for the T_1 relaxation of the proton nuclear spins [87]. In magnetic fields below ~ 3 T, the field suppressed the T_1 relaxation rate. In this regime, it has been found that Zn doping to NENP enhances the T_1 relaxation rate, suggesting a contribution of doping induced unpaired spins [88].

Electron spin resonance (ESR) [89, 90, 91, 92, 93]

The ESR technique experimentally confirmed the Valence Bond Solid picture of the Haldane ground state [89, 90]. In a Cu doped NENP, Hagiwara *et al.* [89] observed the ESR signal from the 'three S=1/2 spin cluster', which corresponds to one Cu^{2+} atomic moment and the two 'chain-end S=1/2 spins' (see Fig.35d). A similar experiment confirmed the chain-end S=1/2 spins with a non-magnetic ion (Zn, Cd and Hg) doping to NENP [90].

Another ESR measurement observed a transition within the triplet excited states [91, 93]. Date and Kindo [91] proposed, from the sign of the single ion anisotropy parameter D, that the excited state of NENP is a local excitation which runs quickly along the chain.

Muon spin relaxation (μSR) [94, 95]

As introduced in Chapter 1, μSR is sensitive to dilute and/or small static moments. In the measurements of NENP, there were no static fields observed down to 20 mK, supporting the non-magnetic ground state [94]. Similar measurements have been performed on other Haldane materials, such as $AgVP_2S_6$ [95], TMNIN [96] and NINO [96], and none of these measurements have detected any static order down to the milli-Kelvin regime.

As listed above, most of the experimental results on NENP supported (1) existence of the Haldane gap, and (2) a singlet ground state described by the Valence Bond Solid picture.

One interesting question regarding the Haldane ground state is what happens to the gap and the ground state, when *charge* is doped to the Haldane system. Since

there have been discussions that high-T_c superconductivity may be realized when a spin-gap system is doped with charge, charge doping to the Haldane system is an interesting process from this point of view. Unfortunately, the Haldane material NENP does not allow charge doping. But recently, a charge-dopable Haldane compound (Y_2BaNiO_5) has been discovered, which is introduced in the next section.

5.2 Haldane material Y_2BaNiO_5

In Fig.38, we show the crystal structure of the inorganic Haldane material Y_2BaNiO_5 [97]. The structure is characterized by chains of compressed NiO_6 octahedra, which are separated by non-magnetic Y^{3+} and Ba^{2+} ions. The shortened Ni-O bonds along the chain (a-axis) lead to a relatively large super-exchange interaction $J \approx 285 \sim 340$ K, as estimated from the magnetic susceptibility [98, 99]. The magnitude of the Haldane gap has been obtained as $E_g \sim 100$ K with susceptibility [100, 101, 99] and inelastic neutron scattering measurements [102, 103].

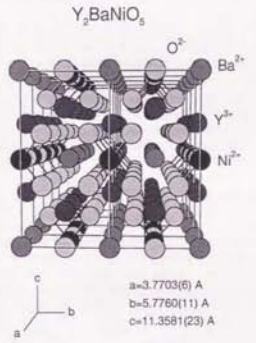

Figure 38:
The crystal structure of Y_2BaNiO_5. $4 \times 2 \times 1$ unit cells are shown. The chain direction is the a-axis.

One valuable feature of this material is that both off-chain charge doping ($Y^{3+} \rightarrow Ca^{2+}$) and on-chain vacancy doping ($Ni^{2+} \rightarrow Zn^{2+}$, Mg^{2+}) is possible [98, 104, 103]. Since charge-doping to the Haldane ground state is a unique feature, some previous measurements have been aimed to clarify the behavior of the doped charge.

DiTusa *et al.* [103] measured resistivity (ρ), X-ray absorption spectroscopy (XAS), and inelastic neutron scattering (NIS) of the Ca/Zn-doped systems, and found the following features:

(1) the doped holes did not induce a clean metallic behavior, but a localized state with hopping (ρ).

(2) the doped holes locate mainly at the $2p_z$ orbital of the oxygen ion, which has a lobe in the chain direction (XAS).

(3) charge doping induces a density of states within the Haldane gap (NIS). With vacancy doping ($Ni^{2+} \rightarrow Zn^{2+}$) such 'in-gap states' were absent.

The result (3) implies that hole-doping strongly perturbs the non-magnetic ground state, while vacancy-doping preserves the non-magnetic ground state.

Quantitatively, vacancy doped Y_2BaNiO_5 has shown a mysterious response. Ramirez *et al.* [104] measured specific heat of the vacancy-doped compounds ($Ni^{2+} \rightarrow Zn^{2+}$) and found that the number of doping-induced spins does not follow the Valence Bond Solid state scenario; the VBS picture predicts the creation of two S=1/2 spins for each vacancy (see Fig.35d), but the Zn-doped Y_2BaNiO_5 system exhibited one S=1 spin for *two* Zn ions. To understand this phenomenon, Ramirez *et al.* suggest a heuristic 'singlet-triplet model', which assumes that half of the broken chains form a triplet S=1 and the other half, a singlet S=0. Neither the origin of the couplings between the chain-end spins nor the local structure of the doping-induced spins is clear at the present stage.

To investigate the ground state properties and dynamics of spin systems, μSR is a powerful technique as introduced in the previous chapter. The following presents μSR results of the nominally pure/doped Y_2BaNiO_5, as well as their susceptibility data in low magnetic fields. For our measurements, polycrystalline specimens of nominally pure Y_2BaNiO_5, Ca doped systems [$(Y_{2-x}Ca_x)BaNiO_5$; x=4.5, 9.5, 14.9 and 30.5%] and Mg doped systems [$Y_2Ba(Ni_{1-y}Mg_y)O_5$; y=1.7 and 4.1%] were prepared at the University of Tokyo, Superconductivity Laboratory, using a standard solid state reaction described below [105]:

- Stoichiometric mixtures of Y_2O_3, $BaCO_3$, NiO plus $CaCO_3$ and/or $MgCO_3$ were prepared.
- The mixture was baked in air at 1050°C for 10 hours.
- After being pressed into a pellet, the sample was baked in air at 1250°C for 10 hours.
- In order to reduce excess oxygen, the sample was annealed in an Ar atmosphere at 1200°C for 10 hours.

Powder X-ray analysis of the samples did not detect any impurity phases. The Ca and Mg concentrations (x and y) were determined with the atomic light-absorption method, which was commercially available (Robertson Microlit Laboratory, NJ, USA).

5.2.1 Susceptibility measurements

In Fig. 39, we show the DC magnetic susceptibilities of our specimens. The increase of susceptibility at low temperatures indicates the creation of paramagnetic moments; their numbers are related to the doping concentrations (x and y). The number of paramagnetic moments created from doping is discussed later.

One significant difference between charge doping and vacancy doping appeared as a spin-glass like behavior for the charge doped systems (x=9.5, 14.9% and 30.5%). From the cusp of the zero-field-cooling (ZFC) susceptibilities, the glass temperatures (T_g) were determined as 2.5, 2.9 and 3.0 K for the x=9.5, 14.9 and 30.5 % systems, respectively. The spin-glass like behavior indicates that the doped hole destroy the non-magnetic ground state.

The vacancy doped systems (y=1.7 and 4.1%) remain paramagnetic down to 2 K. As presented in the next section, the absence of a magnetic order was confirmed to the milli-Kelvin regime.

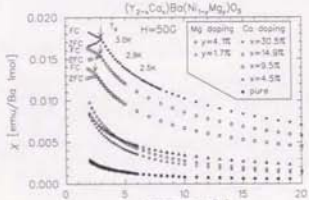

Figure 39:
Magnetic susceptibilities of $(Y_{2-x}Ca_x)Ba(Ni_{1-y}Mg_y)O_5$ (x=y=0, x=4.5, 9.5, 14.9, 30.5% and y=1.7, 4.1%).

One possible reason for the different magnetic behaviors of the charge/vacancy doped systems may be the existence/absence of an interaction across the doping site; although we do not know the local structure of the doping-induced paramagnetic moments, the interaction across a non-magnetic Mg^{2+} ion is probably negligible. Therefore, the broken chains of the vacancy doped system are isolated from each other, leaving no chance for magnetic order. In the charge doped system, on the other hand, there should be a super-exchange coupling (J') across the doping site, Ni^{2+}-O^{-}-Ni^{2+} (or Ni^{2+}-Ni^{3+}-Ni^{2+}), as was the case in an analogous system (Cu doped NENP) [89]. The existence of the interaction between the chain segments may allow the unpaired spins to freeze at $kT \lesssim J'$, if there is a strong coupling within the broken chain segments. The failure of the simple VBS picture to describe the number of unpaired spins in the Zn-doped systems [104] seems to support the existence of strong coupling within the broken chains. To estimate the magnitude of J' is difficult; if one uses J' in Cu doped NENP ($\approx$0.7~0.9 K), and assumes a scaling with the magnitude of Haldane gap (E_g), J' in our system falls on the order of a few Kelvin, which is consistent with the cusp temperatures of the Ca doped systems.

5.2.2 μSR measurements

Fig. 40a shows the μSR spectra of the nominally pure (x=y=0) system. There was slow relaxation in zero-field (ZF, 2.8 K), but the relaxation did not disappear in an external longitudinal field (LF=100 G). This LF measurement proves that the relaxation is in the fast fluctuation regime; if the slow relaxation in zero-field were due to a static random field distribution, it should have been decoupled in a small LF~5 G (see section 3.4). In the nominally pure system, we have confirmed the absence of static order down to 100 mK.

The slow relaxation of the muon spin follows a square-root exponential function ($P_a(t) \approx \exp(-\sqrt{\lambda t})$; solid lines in Fig.40a), which is characteristic of dilute spin systems in a paramagnetic state (see section 3.2). As discussed later, the slow T_1 relaxation is most likely caused by native unpaired spins in the sample.

In Fig. 40b, we compare μSR spectra from the pure, charge doped (Ca: x=4.5 and 9.5%) and vacancy doped (Mg: y=4.1%) systems in the milli-Kelvin regime. In the Ca doped, x = 9.5% sample, there is fast muon spin relaxation, reflecting the spin-glass behavior in the susceptibility. In the Mg doped y = 4.1% sample, muon spin relaxation is even *slower* than in the nominally pure system, which suggests an absence of static order in the Mg doped systems. This point was also confirmed with longitudinal field decoupling measurements (Fig.42).

In order to obtain the muon spin relaxation rate (λ), we analyzed the spectra with a phenomenological stretched exponential function, $\exp(-(\lambda t)^{\beta})$, which describes paramagnetic relaxation with $\beta = 0.5 \sim 1$ (see Chapter 3), as well as the slow fluctuation regime of dilute spin systems ($\beta \sim 1$) and the dense spin systems ($\beta \sim 2$). One problem of this universal relaxation function is that it often shows correlations between β and λ, when the relaxation rate (λ) is small. Therefore, it is safer to fix β for the analysis of the fast fluctuation regime, in order to obtain the appropriate temperature and/or field dependence of the relaxation rate (λ).

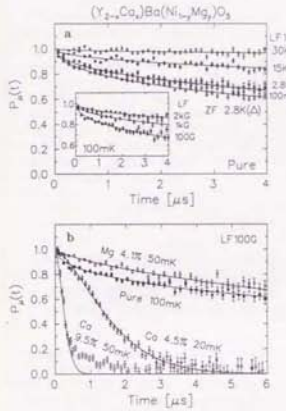

Figure 40:
(a) μSR spectra of the nominally pure Y_2BaNiO_5. The solid line is the fit with the square-root exponential function. (b) LF=100 G μSR spectra are compared at $T \leq$100 mK. The solid lines are the fit with the stretched exponential functions.

For the analysis of the nominally pure sample, we fixed as β = 0.5, namely, to the square-root exponential function. The overall fit was good, as shown in Fig.40a. In the Mg-doped systems, the μSR spectra do not exhibit the fast front-end (Fig.40b), suggesting $\beta > 0.5$. We fixed β to 0.72 (Mg 1.7%) and 0.77 (Mg 4.1%) which is the average of β, obtained from a preceding analysis without constraints on β. For the Ca-doped systems at $T > 6$ K, we adopted β=0.5. Below 6 K, we were able to obtain β and λ independently. It was found that β of the Ca-doped systems approaches $1.5 \sim 2$ in the milli-Kelvin regime. In Fig.41, relaxation rates (λ) for the LF=100 G measurements (and for the pure sample, the results of higher LF measurements as well) are shown, as a function of temperature.

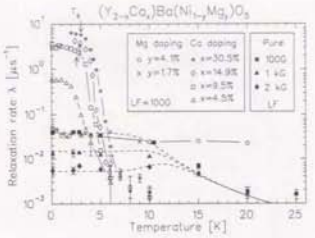

Figure 41:
Temperature dependence of muon spin relaxation rate (λ). For the doped samples, the results from LF=100 G measurements are shown; for the nominally pure sample, the data in higher LF's are shown as well. The solid lines (for the doped systems) and the dashed lines (for the pure system) are guides to the eyes.

Nominally pure and the vacancy doped systems

For the pure and vacancy-doped systems, the relaxation rate (λ) at $T \lesssim$ 10 K is temperature independent (Fig.41); this is a characteristic of paramagnetic relaxation. As shown in Fig.42a,b, we also performed longitudinal field (LF) decoupling measurements in the milli-Kelvin regime, and proved the dynamic nature of the relaxation. The LF measurements confirm the absence of a static order in the vacancy doped system.

As shown in Fig.42c, we have analyzed the LF dependence of the relaxation rate λ using the T_1 formula for dilute spin systems (eq.33). The resulting Lorentzian field width (a) and field fluctuation rate (ν) are shown in Table 5. It was suggested that vacancy-doping results in faster field fluctuations (ν) and a larger field width (a) than the nominally pure system shows. Qualitatively, this result may be understood, if muons detect the dipolar fields from unpaired spins in the sample: as susceptibility has indicated, the number of unpaired spins increases upon doping. Therefore, the doped system should exhibit a larger field-width (a) at muon location, if the muons detect the dipolar fields from the doping induced moments. If the interactions between these unpaired spins are also dipolar interactions, the field fluctuation rate (ν) should increase upon doping, as has been observed in the Mg doped systems. A more quantitative discussion, which leads to the estimates shown in Table 5, is given later.

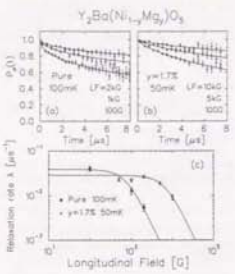

Figure 42:
The LF-μSR spectra of (a) the nominally pure sample and (b) the Mg doped $y = 1.7\%$ doped system. The solid lines are the fit to the stretched exponential functions, $P_x(t) = \exp(-(\lambda t)^\beta)$ with (a) $\beta = 0.5$ and (b) $\beta = 0.72$. (c) The relaxation rate (λ) as a function of the longitudinal fields applied. The solid lines are the analysis with the T_1 relaxation theory (eq.33).

Table 5: Results from the T_1 relaxation analysis

Sample	Parameter	Experiment	Estimate[a]
Pure	α (μs^{-1})	0.74(4)	$0.3 \sim 3$
	ν (MHz)	72(12)	$18 \sim 180$
Mg 1.7%	α (μs^{-1})	2.0(2)	$0.8 \sim 6$
	ν (MHz)	600(100)	$50 \sim 360$

[a] see the discussion later.

Charge doped systems

In the Ca doped systems, a sharp increase of the relaxation rate (λ) was observed as the temperature approached T_g from the paramagnetic side (Fig.41). The increase of the relaxation rate probably reflects the critical slowing down of the moments, as has been observed typically in spin glass systems [7]. In the Ca doped $x = 4.5\%$ sample, the temperature dependence of λ suggests a glass temperature $T_g \sim 1.5$ K, which was below the temperature of our SQUID magnetometer.

In order to investigate field fluctuations in the charge doped system, we performed longitudinal field measurements. The results are shown in Fig. 43. The zero-field (ZF) spectrum exhibited a Gaussian decay, which seemed to be the Gaussian Kubo-Toyabe function in the slow fluctuation regime (see section 3.1). However, the LF dependence of the relaxation didn't follow the predictions of the Gaussian Kubo-Toyabe theory. If the

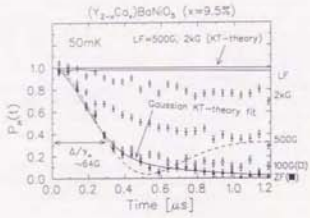

Figure 43:
LF-μSR spectra in the Ca doped $x = 9.5\%$ sample at 50 mK. The solid line on the zero-field (ZF) data is the fit with a dynamical Gaussian Kubo-Toyabe function. The broken line is the Kubo-Toyabe function in static case.

Gaussian behavior in the zero-field were due to almost static Gaussian field distribution, the relaxation should have been decoupled in a LF~200 G, while in fact, the relaxation was present up to LF=2 kG. There are two unconventional behaviors presented in this result:

(1) The weak LF dependence of the relaxation suggests persistent dynamics in the spin system, even though the temperature ($T = 50$ mK) is well below the glass temperature ($T/T_g \approx 0.02$).

(2) There has been no theories which allow the coexistence of the zero-field *Gaussian* decay and fast field fluctuations. In the framework of the conventional Kubo-Toyabe theory, fast fluctuation induces either an exponential function (dense spin system) or a square-root exponential function (dilute spin system), but never a Gaussian decay (see Chapter 3).

This result is further investigated in the next section.

5.2.3 Discussion

Unconventional dynamics in the charge doped systems

In the milli-Kelvin regime of the charge doped systems, we observed a Gaussian relaxation which showed much weaker LF decoupling than the Gaussian Kubo-Toyabe theory predicts. One idea to explain the unconventional Gaussian relaxation is to introduce dilution of the local field in a *time-wise* manner [106]. As has been presented in Chapter 3, conventional Kubo-Toyabe theory assumes that the local fields exist at all times, fluctuating with a time independent fluctuation

rate (ν). For the corresponding Gaussian Kubo-Toyabe function in the slow fluctuation regime, the zero-field relaxation rate (Δ) reflects the Gaussian field width, and the decoupling longitudinal field is comparable to that width ($H_{LF} \sim \Delta/\gamma_\mu$; see section 3.1). Now, suppose the local field is almost static during a certain fraction of time ($0 < f \leq 1$), and fast fluctuating otherwise (Fig.44). If the muon spin relaxation occurs only during the slow fluctuation time, a Gaussian relaxation rate may be observed, but with a diluted relaxation rate as $\Delta \to f \cdot \Delta$. Even in this unconventional situation, the decoupling field H_{LF} will remain comparable to the instantaneous internal-field width Δ/γ_μ, because the decoupling happens as the competition between the external longitudinal field H_{LF} and the internal random fields Δ/γ_μ. Therefore, in this hypothetical situation, the decoupling may happen at much larger longitudinal fields than the zero-field relaxation rate suggests.

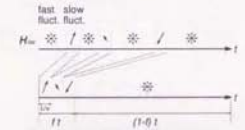

Figure 44:
Hypothetical field dynamics which has slow fluctuations randomly appearing in the quickly fluctuating majority.

Taking into account the slow paramagnetic relaxation caused during the fast fluctuation time, the muon spin relaxation due to this unconventional field fluctuations may be expressed as [106]:

$$G^f(t) = G^{\mathrm{DGKT}}(ft, \Delta, H_{LF}, \nu) \times \exp(-(\lambda t(1-f))^\beta) \quad (44)$$

where G^{DGKT} is the dynamical Gaussian Kubo-Toyabe function (see section 3.1), which originates from the slow fluctuation time, and the stretched-exponential part from fast fluctuation time. We have analyzed our μSR spectra with this hypothetical relaxation function; Fig.45 shows the fits to the data from the Ca doped $x = 9.5\%$ sample. The overall longitudinal field dependence is described by mainly adjusting the time-fraction parameter $f \sim 0.2$.

Using the same hypothetical relaxation function (eq.44), we have analyzed the spectra from other Ca-doped systems (x=4.5, 14.9 and 30.5%). The fraction parameter (f) and the instantaneous Gaussian width (Δ) are shown in Fig.46. It was found that the Gaussian width

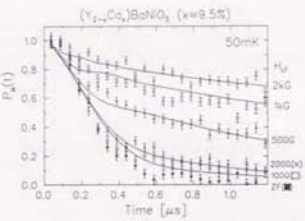

Figure 45:
The same LF-μSR data with Fig.43. The solid lines are the fit with the hypothetical relaxation function (eq.44) to the LF=100, 200, 500, 1k and 2kG data.

(Δ) is almost independent of the Ca concentrations (x), while the fraction parameter (f) reflects the concentrations: a smaller Ca concentration results in a smaller fraction parameter (f), indicating more unconventional fluctuations (note that regular Markoffian spin fluctuations are described with $f = 1$). The indifference of the Gaussian width (Δ) to the charge concentrations suggests that the muon spin relaxation mechanism is common to all the charge doped systems, but how frequently the relaxation is caused ($\approx f$) is determined by the charge concentration.

One possible description of the relaxation mechanism is that the doped hole, which takes a localized state with hopping [103], occasionally comes close to the muon site and induces muon spin relaxation. When the charge is far away, the muon relaxation should be small and dynamic, because the majority of the spins on the chain may stay in the non-magnetic ground state.

Phenomenologically, the magnetic behavior of the charge doped Haldane material $(Y_{2-x}Ca_x)BaNiO_5$ is very similar to that of the Kagomé-lattice compound $(SrCr_zGa_{(12-z)}O_{19})$, a geometrically frustrated antiferromagnet of Cr moments (S=3/2). The susceptibility measurements of the Kagomé-lattice system [107, 108, 109] have revealed the existence of a small portion of unpaired spins ($\sim$ 5% of the total Cr ions for the $z = 8$ sample), which exhibit a spin-glass-like history dependence below $T_g \sim 3.5$ K. The unpaired moments observed in the susceptibilities are probably caused by Ga substitutions to the Cr sites, which are inevitable in this series of Kagomé compounds [109]. The ZF-μSR spectrum of the z=8 Kagomé material approaches a Gaussian shape as $T \to 0$ [106], while LF-μSR measurements at 100 mK suggest fast field fluctuations

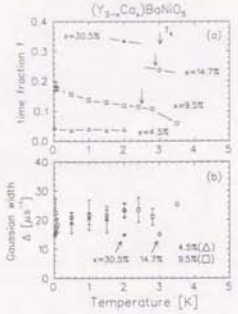

Figure 46:
(a) The fraction parameter (f) and (b) the instantaneous Gaussian width (Δ) obtained from the analysis using the hypothetical relaxation function (eq.44).

[95, 106, 110]. Neutron scattering measurements of the z=7.1 Kagomé compound [111] have also suggested persistent dynamics below the cusp temperature; a large fraction ($\sim$ 80%) of the scattering intensity was found to remain in the inelastic channel at $T/T_g \sim 0.5$.

Theoretically, the S=1/2 Kagomé-lattice system may have a ground state composed of many singlet pairs [112], as expressed by the resonating valence bond (RVB) state. In this situation, the unpaired spins created by non-magnetic ion doping still have the ability to migrate spatially, because the surrounding spins have a large number of combinations for their singlet pairings. In the charge doped Haldane system, the doped charge may also move, with the surrounding spins in the singlet state. Considering these similarities, the persistent dynamics below the spin-glass like cusp temperature, as well as the hardly decoupled Gaussian relaxation of μSR spectra may be common signatures for migrating unpaired spins in singlet ground state materials.

Paramagnetic fluctuations in the pure and Mg doped systems

From the longitudinal field (LF) dependence of the muon spin relaxation rate (λ), it was shown that the nominally pure and the vacancy doped systems stay paramagnetic down to the milli-Kelvin regime (Fig.42). The doping dependence of the Lorentzian width (a) and the field fluctuation rate (ν) qualitatively suggests that muons are detecting the dipolar fields from the unpaired spins (see Table 5). In this section, a more quantitative discussion is given.

In order to estimate the numbers of unpaired spins, we analyzed the paramagnetic region of the susceptibilities with the Curie-Weiss law $\chi(T) \approx C/(T+Tw)$, a model which assumes that all the doping effect is a creation of local moments. The results are shown in Fig.47.

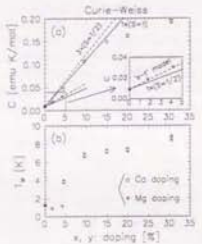

Figure 47:
The doping concentration (x, y) dependence of (a) the Curie constant (C) and (b) the Weiss temperature (Tw).

In the vacancy doped systems, the Mg concentration (y) dependence of the Curie constant (C) is consistent with the heuristic 'singlet-triplet' model, which assumes that *two* Mg^{2+} ions effectively create one S=1 spin [104]. In the charge doped systems, one Ca ion seems to create $\sim 1 \times S$=1 spin, or $\sim 3 \times S$=1/2 spins. Since susceptibility has no information about the local structure of the unpaired spins, it is not possible to distinguish these two situations. For simplicity, we assume hereafter that $\sim 1 \times S$=1 effective spins are created for one Ca ion, and $0.5 \times S$=1 spins for one Mg ion.

It is known that the paramagnetic moments of the nominally pure Y_2BaNiO_5 are created by excess oxygen, which works as a hole-dopant [105]. The Curie constant of the nominally pure specimen corresponds to the native charge concentration of $c_0 \sim 0.6$ at.%, which has been estimated by extending the Ca concentration dependence of the Curie constant (Fig.47a) to the negative x side.

In order to estimated the Lorentzian field width (a) generated from the unpaired spins, we utilized the procedure developed for analysis of the dilute spin-glass alloys [7]:

(1) obtain the hypothetical Gaussian field width ($\Delta^{ZF}_{100\%}$) for the situation in which all the spin sites are filled up with randomly oriented moments. In zero external field, this Gaussian width ($\Delta^{ZF}_{100\%}$) is expressed as [6]:

$$(\Delta^{ZF}_{100\%})^2 = \frac{2}{3}S(S+1)\gamma_\mu^2(\hbar\gamma_e)^2\sum_i r_i^{-6} \quad (45)$$

where, S is the size of the spins at each site, $\gamma_\mu(\gamma_e)$ is the muon(electron) gyromagnetic ratio. ($\hbar\gamma_e \equiv g\mu_B$, where g is the g-factor and μ_B is the electron Bohr magneton.)

(2) using eq.26, obtain the Lorentzian width (a) from the hypothetical Gaussian width.

Since we do not know the muon site in Y_2BaNiO_5, we assumed locations shown in Fig.48. These sites assumed are all $\sim$ 1Å away from a oxygen ion, where a muon usually resides in oxides [113, 114, 115, 116, 117]. We numerically performed the dipolar sum (eq.45), assuming that the g-factor is 2 for the doping induced S=1 spins. The results ($\Delta^{ZF}_{100\%}$) are shown in Fig.48.

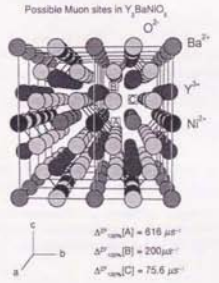

Figure 48:
Possible muon sites in Y_2BaNiO_5. The Gaussian widths were calculated for these three sites, using eq.45.

If an external field is applied to a paramagnetic spin system, the electron moments undergo Larmor precession. Since the gyromagnetic ratio of muon and electron differ by two orders of magnitude, the precessing electron spin component becomes invisible to a muon. Namely, only the secular part of the dipolar field contributes to muon spin relaxation in longitudinal field measurements. For paramagnetic T_1 relaxation, the secular contribution is 3/10 of the zero-field T_1 relaxation rate (the 10/3-effect [9, 10]; see section A.2). Therefore, the hypothetical Gaussian width appropriate to the longitudinal field measurements ($\Delta^{LF}_{100\%}$) becomes:

$$\Delta^{LF}_{100\%} = \sqrt{3/10}\,\Delta^{ZF}_{100\%} \quad (46)$$

Using the Gaussian width $\Delta^{LF}_{100\%}$, the estimated unpaired spin concentration $c = c_0 + 0.5y$ (y is the Mg concentration) and eq.26, the Lorentzian field widths (a) were estimated as shown in Table 5. Although the ambiguity from the muon site is large, the experimental data is within the range of the estimated magnitude.

If the fluctuations of the unpaired spins are governed by their dipolar interactions, the fluctuation rate (ν) should scale with the Lorentzian width (a). The ratio ν/a will be the order of the ratio of the electron/muon gyromagnetic factors ($\nu/a \approx \gamma_e/\gamma_\mu \times \sqrt{10/3}/2\pi \approx$ 60), where the factor $\sqrt{10/3}$ comes from the fact that an electron moment detects the entire spin of other electrons, and the factor 2π corrects the units (a in rad/sec and ν in Hz). The fluctuation rates estimated as above are shown in Table 5. The experimental results again are in the same order of magnitudes with these estimates.

The above estimates of the field width (a) and the fluctuation rate (ν) in the nominally pure and Mg-doped systems supports the scenario in which the muon detects the dipolar fields of the unpaired spins in these systems.

5.3 Summary

We have investigated charge/vacancy-doped Haldane systems with magnetic susceptibility and μSR. The nominally pure sample does not show magnetic order down to 100 mK, supporting the singlet nature of the Haldane ground state. In the vacancy-doped systems, unpaired spins were created because of the doping, but they remained paramagnetic down to T=50 mK. In these two non-magnetic systems, muons are most likely detecting the dipolar fields from the unpaired spins.

In the charge-doped Haldane compounds, the susceptibility exhibited a spin-glass like history dependence below T_g=1.5~3 K. However, μSR has revealed persistent spin dynamics down to 50 mK, which is well below the glass temperature T_g. It was also found that the spin fluctuations of the charge-doped systems in the milli-Kelvin regime follow an unconventional, non-Markoffian processes.

6 Spin-Peierls system††

This chapter presents our μSR results of the spin-Peierls material $CuGeO_3$ and its Zn/Si doped compounds. In the nominally pure system, the absence of static moments was confirmed down to 50 mK, supporting the non-magnetic nature of the spin-Peierls ground state. In the Zn-doped systems $(Cu_{1-x}Zn_x)GeO_3$ (x=2, 4 and 8%) and a Si-doped system $Cu(Ge_{1-y}Si_y)O_3$ (x = 2 %), static order was observed below the Néel temperatures which have been reported previously. In the Zn-doped systems, the characteristic magnitude of the local field (Δ) suggests that the size of the ordered moments takes a maximum at the Zn concentration which gives the maximum Néel temperature.

6.1 Introduction

6.1.1 Theories

The spin-Peierls transition, which was proposed for an antiferromagnetic S=1/2 spin chain [14, 15, 16], is characterized by two features: (1) alternating deformation of the lattice along the chain direction, and (2) singlet pair formations of the two S=1/2 spins on the shortened link (Fig.49b). Although the lattice dimerization (1) increases the elastic energy, the transition may still be possible if the singlet pair formation (2) compensates the energy increase. In order to estimate the conditions for spin Peierls transition, a quantum mechanical treatment of the spin system is necessary, because singlet-pair formations are involved in the transition mechanism.

Figure 49:
(a) An S=1/2 spin chain with a uniform antiferromagnetic interaction J. (b) The lattice dimerized state below the spin Peierls transition temperature T_{SP}.

A Hamiltonian of a one-dimensional spin chain which allows lattice deformation can be expressed as:

$$\mathcal{H} = \sum_i J(i,i+1)\boldsymbol{S}_i \cdot \boldsymbol{S}_{i+1} + \frac{K}{2}\sum_i (u_i - u_{i+1})^2 \quad (47)$$

where $J(i,i+1)$ is the antiferromagnetic interaction between the spins on the i-th and the $(i+1)$-th site, K is the spring constant of the lattice, and u_i is the displacement of the lattice point i. The first term of this Hamiltonian describes the spin system and the second term, the elastic energy of the lattice system. Under a lattice deformation along the chain, the antiferromagnetic coupling $J(i,i+1)$ is expanded as

$$\begin{aligned} J(i,i+1) &= J + (u_{i+1}-u_i)\frac{\partial J(i,i+1]}{\partial(u_{i+1}-u_i)} + \cdots \\ &= J + \frac{\lambda J}{2a}(u_i - u_{i+1}) \\ &= J(1 \pm \delta)\begin{cases} \text{shortened link} \\ \text{stretched link} \end{cases} \end{aligned} \quad (48)$$

where λ is a spin-lattice coupling constant and a is the lattice spacing. The last equation holds for the lattice dimerized state (displacement u) with $\delta = \lambda u/2a$. Using eq.48 the Hamiltonian (eq.47) is rewritten as:

$$\mathcal{H} = \sum_i \{J\boldsymbol{S}_i \cdot \boldsymbol{S}_{i+1} + \frac{\lambda J}{2a}(u_i - u_{i+1})\boldsymbol{S}_i \cdot \boldsymbol{S}_{i+1} + \frac{K}{2}(u_i - u_{i+1})^2\} \quad (49)$$

where, the second term gives a spin-lattice coupling.

Analytical approaches to the spin Peierls problem have been unsuccessful; one popular way to solve the problem is as follows:

(1) map the spin Hamiltonian to a fermion system using the Jordan-Wigner transformation [118]

(2) solve the fermion system, using various approximation techniques developed for fermion systems

(3) obtain the phonon features, with perturbation treatments of the fermion-phonon coupling, which arose from the spin-lattice coupling (the second term of eq.49).

Since step (2) involves the quantum mechanics of the spin system, this part is the most crucial to this theoretical approach; indeed, the spin-Peierls transition temperature strongly depends on this part.

Bulaevskii [119] and Pytte [120] adopted the Hartree approximation for step (2) and calculated the phonon frequency (ω) above the spin Peierls transition temperature. Their result is:

$$\omega^2 = \omega_0^2\left(1 - c_1\eta'\ln\frac{c_2 J}{kT}\right) \quad (50)$$

where, ω_0 is the bare phonon frequency, $\eta' = \lambda^2 J/Ka^2$ is a dimensionless spin-lattice coupling parameter and the constants are $c_1 \approx 0.51$ and $c_2 \approx 1.4$. A softening of phonons is predicted, as the result of fermion-phonon coupling. From the temperature which gives a zero phonon frequency, the spin Peierls transition temperature T_{SP} has been estimated as:

$$kT_{SP} \approx c_2 J \exp\left(-\frac{1}{c_1\eta'}\right) \quad (51)$$

Since the Hartree approximation drops the exchange interaction between two fermions, it may not adequately include quantum fluctuations. In fact, a quantum mechanical treatment introduced below gives an enhanced spin Peierls transition temperature.

Cross and Fisher [121] approximated the mapped fermion system with an exactly soluble model (Tomonaga-Luttinger model [122, 123]), preserving the physical features around the Fermi surface. This approximation, which was first introduced by Luther and Peschel [124], well describes the low temperature behavior of the original fermion system, because that behavior is determined by features around the Fermi surface. Since the treatment after the approximation is exact, quantum mechanical effects should be included correctly in the results. Cross and Fisher obtained the phonon frequency above T_{SP} as:

$$\omega^2 = \omega_0^2\left(1 - 0.8\,\eta'\frac{J}{kT}\right) \quad (52)$$

which gives the spin Peierls transition temperature as:

$$kT_{SP} \approx 0.8\,\eta' J \quad (53)$$

Cross and Fisher's T_{SP} is higher than that from the Hartree approximation (eq.51); the spin Peierls state is preferred in a more quantum mechanical treatment. This behavior is opposite to that of Néel temperature which usually decreases with more quantum mechanical treatments. The difference probably originates from the classical nature of the Néel state and the quantum mechanical singlet nature of the spin Peierls ground state.

In 1980, Nakano and Fukuyama [125, 126] formulated Cross and Fisher's approach using a phase variable:

$$\mathcal{H} = \int dx\{A(\nabla\theta(x))^2 + Cp^2(x) - B\sin\theta(x) - D\cos 2\theta(x) + \frac{2K}{a}u^2\} \quad (54)$$

where x is the position on the chain, $\theta(x)$ is the phase variable and $p(x)$ is its momentum; $\theta(x)$ and $p(x)$ satisfy the canonical relation:

$$[\theta(x), p(x')] = i\delta(x - x') \quad (55)$$

For a dimerized Heisenberg chain, the coefficients take the following values:

$$A = \frac{1}{8}Ja \quad B = \frac{J\lambda_0}{a^2} \quad C = \frac{\pi^2}{2}Ja \quad D = \frac{\pi^2}{8a}J \quad (56)$$

Using the phase variable $\theta(x)$, the z-component of a spin is expressed as:

$$S^z(x) = \frac{1}{a}\cos\left(\frac{\pi}{a}x + \theta(x)\right) + \frac{1}{2\pi}\nabla\theta(x) \quad (57)$$

As shown in eq.57, the Néel state ($[\theta(x) = 0]$ and the singlet state ($[\theta(x) = \pi/2]$ are both expressed equally in this 'phase Hamiltonian' (eq.54). It has been shown that this formalism gives the same result as Cross and Fisher's approach, but more easily and intuitively [125, 126]. Using the phase Hamiltonian approach, the effects of inter-chain interactions (J') and external magnetic field (H) have been investigated [17, 18]. The results are summarized as follows:

(1) In zero-field, the ground state is either the Néel state or spin-Peierls state, depending on the magnitude of the inter-chain interaction. The phase boundary $j'/\eta = \sqrt{(1-d)/(1+d)}$ is first order, where $j' = zJ'/\pi^2 J$ is a normalized inter-chain interaction, $\eta = \eta'/4\pi^2$ is a dimensionless spin-lattice coupling parameter and $d = a^2 D/2\pi^2 A$.

(2) The ground state in finite magnetic field was obtained, as shown in Fig.50. The spin-Peierls phase (SP) makes a first order transition to a magnetic phase (M*) at a critical field (h_{c1}). There is a spin-flop phase (SF) in the large j' region, but experimentally the SP→SF transition may be difficult to observe, because of the narrow parameter range (B on the j'/η-axis) as the condition.

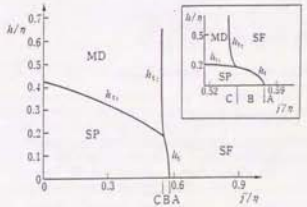

Figure 50:
Theoretical ground state phase diagram in magnetic field. The spin-Peierls phase makes a first order transition to a magnetic phase (M*). Cite from Ref. [18]

††Unpublished work under collaboration, K. Kojima *et al.* unpublished.

6.1.2 Organic spin Peierls materials

The spin Peierls transition was observed experimentally in the 1970's, with organic materials such as, TTF-CuBDT, TTF-AuBDT [127, 128] and MEM-$(TCNQ)_2$ [129]. These materials show a structural transition at relatively high temperatures (T_L=240 K for TTF-CuBDT and 340 K for MEM-$(TCNQ)_2$), so that a one dimensional chain structure is prepared. The S=1/2 spins are held by a lone-pair on a molecule (TTF^+ and $(TCNQ)_2^-$).

In these materials, the spin Peierls transition was identified with an exponential drop of susceptibility below T_{SP} (11 K for TTF-CuBDT [127, 128] and 18 K for MEM-$(TCNQ)_2$ [129]). Contrary to an antiferromagnetic Néel order, the drop of susceptibility is isotropic, suggesting a spin singlet formation. In the following, other experimental signatures of spin Peierls transition are introduced.

Structural investigations [130, 131]

Since the spin Peierls transition involves a lattice deformation, lattice structures and phonons also reflect the onset of the transition. X-ray and neutron scattering measurements [130, 131] observed the superlattice reflections below T_{SP}, supporting the dimerization of the lattice. It was found, though, that the superlattice reflections do not necessarily appear along the chain direction; in TTF-CuBDT, the lattice also deforms perpendicular to the chain at the same time as the dimerization takes place [130].

Another finding of these scattering measurements is the existence of soft phonons at the superlattice Bragg point. These soft phonons were observed well above T_{SP}, at temperatures close to the structural transition temperature T_L; therefore, this mode is probably a feature of the lattice system, not being induced by the spin Peierls behavior. The existence of the soft phonon mode probably helps the spin Peierls transition, because the lattice dimerization corresponds to the freezing of this mode [132].

High-field measurements [133, 134, 135, 136, 137, 138]

Since the first excited state of the spin Peierls phase is the triplet state, one can close the spin Peierls energy gap by applying a large magnetic field. Experimentally, high-field magnetization measurements [133, 134, 135] have detected this signature. At $T < T_{SP}$, the magnetization $M(H)$ remained small up to a critical field (H_c), and above H_c, it linearly increased. This experimental result indicates that one branch of the triplet states crosses levels with the singlet ground state at the critical field H_c.

High-field magnetization measurements have provided the phase diagram of spin Peierls materials as shown in Fig.51. It was found that the phase boundaries fall on universal curves, if temperature (T) and magnetic field (H) were normalized with $T_{SP}(H=0)$, which is the spin-Peierls transition temperature in zero-field [135]. From the hysteresis of magnetization [135], the phase boundary between the spin-Peierls phase (SP) and the magnetic phase (M*) was found to be first-order. The phase boundary between the uniform phase (U) and other phases (SP and M*) is second order. This boundary is well described with a theoretical curve [140] obtained from Cross and Fisher's approach.

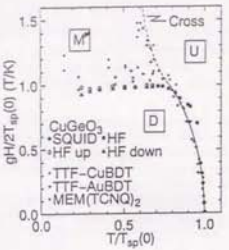

Figure 51:
Phase diagram of spin Peierls systems. Temperature (T) and magnetic field (H) are normalized with $T_{SP}(H=0)$. Cite from Ref. [139].

As a microscopic structure of the M* phase, a localized spin state (spin soliton) has been proposed theoretically [126]. If this localized spin state is realized, the local field at a certain position of the crystalline unit cell should have a relatively broad distribution, because the spin soliton is spatially inhomogeneous. From an investigation of the ^{1}H- and ^{19}F-NMR lineshape [136] and ESR line-shift [137], the existence of spin solitons was experimentally suggested in the M* phase of TTF-AuBDT.

Theoretically, the spin soliton is accompanied by incommensurate lattice modulations; in the vicinity of a spin soliton, the lattice dimerization should be lifted. Recently, Kiryukhin *et al.* performed high-resolution X-ray diffraction measurements on TTF-CuBDT, and found the incommensurate modulations of the lattice appearing in the M* phase [138].

As introduced above, the spin Peierls transition can be investigated with variety of experimental techniques, because the transition involves both the spin systems and the lattice system. Therefore, when a new spin Peierls material $CuGeO_3$ was discovered in 1993 [141], there was a surge of experiments on this material. The next section introduces these experiments, along with our μSR results.

6.2 Spin-Peierls material $CuGeO_3$

The first spin Peierls materials were all organic. This may be attributed to the characteristics of organic materials that (1) the lattice is soft and its deformation is relatively easy and (2) the distance between the spin-chains is relatively large, so that they are magnetically well isolated from each other. As an *inorganic* material, $CuGeO_3$ was the first material identified to exhibit a spin Peierls transition [141].

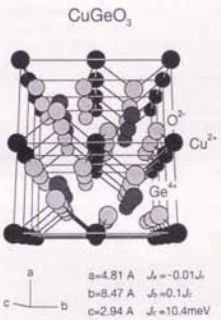

Figure 52:
Crystal structure of $CuGeO_3$. In the c-axis direction, CuO_2 chains are present. The lattice parameters are cited from Ref. [142]; the in-chain magnetic coupling parameters are from Ref. [143].

The crystal structure of $CuGeO_3$ is shown in Fig.52. A Cu^{2+} ion (S=1/2) is surrounded by six O^{2-} ions, which form a distorted CuO_6 octahedron. Cu^{2+} ions are bridged with four closer O^{2-} ions, making a CuO_2 chain (ribbon) in the c-axis direction. These chains are supported with Ge^{4+} ions, which locate at the tetrahedral site surrounded by four O^{2-} ions. Reflectivity and photoemission measurements [144] have shown that the $p-d$ hybridization of the CuO_2 chain is small. Hence the localized-moment picture of the Cu^{2+} spins should be good in $CuGeO_3$.

In the first report, Hase *et al.* [141] presented (1) an isotropic drop of susceptibility at T_{SP}=14 K and (2) the field dependence of $T_{SP}(H) \propto H^2$, as signatures of the spin Peierls transition in $CuGeO_3$. Since then, there have been many experiments performed on this material, and some of them report typical signatures of spin Peierls transition, as reviewed in the following.

6.2.1 Previous measurements

Superlattice reflections [145, 146, 147]

Superlattice reflections for lattice dimerization were found at $h/2, k, l/2$ (h, k, l all odd) with electron diffraction (Kamimura *et al.* [145]) and X-ray measurements (Pouget *et al.* [146]). Almost at the same time, Hirota *et al.* confirmed with neutron scattering measurements that even-number k's are also allowed [147].

Softening of the lattice [148, 149, 150, 151, 152]

Poirier *et al.* investigated elastic constants with ultrasonic velocity measurements. They observed a softening of the lattice in the chain direction, starting at $\sim$ 3 K above T_{SP} [148]. This softening may be induced by the spin Peierls transition.

In contrast, neutron scattering measurements [149] have found a soft phonon mode *perpendicular* to the chain (b-axis direction). In addition, X-ray diffraction measurements [150] found a large contraction of the b-axis lattice parameter at T_{SP}. Neutron scattering measurements under pressure [151] showed a pronounced decrease of the b-axis lattice parameter.

Chen *et al.* observed diffuse scattering below $\sim$100 K with electron diffraction measurements [152]. They proposed a twisting mode of the CuO_2 ribbons to explain their results.

Structural signature of SP→M* transition [153]

Kiryukhin *et al.* observed the SP→M* transition with high-resolution X-ray measurements; the superlattice Bragg reflection split at the SP − M* phase boundary, indicating an incommensurate modulation of the lattice dimerized state in the M* phase [153].

Magnetic phase diagram [139, 148]

Hase *et al.* performed magnetization measurements and obtained the H–T phase diagram (Fig.51). They found that the phase boundaries follow the universal curve of the previous organic spin Peierls systems [139]. The

$H-T$ phase diagram has also been reported from ultrasonic measurements [148].

Spin Peierls gap [143, 154]

Nishi *et al.* observed the spin Peierls energy gap with inelastic neutron scattering measurements [143]. From the dispersion curve of the triplet excited state, the in-chain (J_c) and the inter-chain (J_a and J_b) magnetic coupling parameters were also obtained (shown in Fig.52). Fujita *et al.* performed neutron scattering measurements in magnetic fields up to 6 T [154]. They found the excited state split into three branches, indicating its triplet nature.

Spin relaxation measurements [155, 156, 157]

Oseroff *et al.* measured the EPR signal from Cu^{2+} ions, and found a decrease of signal intensity below T_{SP} [155]. Brill *et al.* performed high-field ESR measurements and identified singlet-triplet and triplet-triplet transitions [156]. Itoh *et al.* performed ^{63,65}Cu-NMR and NQR measurements [157], and found a drop of the ^{63}Cu nuclear T_1 relaxation rate below T_{SP}.

As shown above, most of the previous measurements of $CuGeO_3$ support the identification of a spin Peierls transition at $T_{SP} \approx 14$ K.

6.2.2 Non-magnetic ion doping

One interesting feature of $CuGeO_3$ is that non-magnetic ion doping on the chain ($Cu^{2+} \rightarrow Zn^{2+}$) and out of the chain ($Ge^{4+} \rightarrow Si^{4+}$) is possible. It has been shown that these two kinds of doping lead to a Néel ordered ground state.

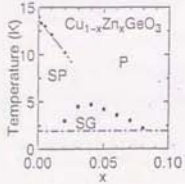

Figure 53:
Zn-concentration (x) verses temperature (T) phase diagram of $(Cu_{1-x}Zn_x)GeO_3$. Cite from Ref. [158]. The spin-glass phase (SG) was later proposed to be a Néel ordered phase.

Hase *et al.* measured magnetic susceptibility of the Zn-doped compounds $(Cu_{1-x}Zn_x)GeO_3$, and found that (1) the spin Peierls transition disappears at $x \sim 2$ % and (2) a new cusp appears in the Zn concentration range of $2 \lesssim x \lesssim 8$ % [158]. The cusp temperature takes a maximum at $x \sim 4$ %. A magnetic phase diagram was obtained as shown in Fig.53.

Oseroff *et al.* measured the specific heat (C_p) of Zn, Ni and Mn-doped $CuGeO_3$ and found a peak at the cusp temperature [159]. Since a peak in the specific heat should be absent for the spin-glass transition [160], but present for Néel order, they proposed a Néel ordered ground state for the doped materials.

Recent neutron scattering measurements of single crystalline $(Cu_{1-x}Zn_x)GeO_3$ ($x = 3.4$ %) showed the existence of antiferromagnetic Bragg reflections [161]; this result directly indicates the Néel order. The size of the ordered moments was obtained as $\sim 0.2\ \mu_B$, which is less than half of what was observed in a Néel ordered spin chain ($0.49\ \mu_B$ for $KCuF_3$ [162]).

Si-doped systems $Cu(Ge_{1-y}Si_y)O_3$ were investigated by Renard *et al.* with susceptibility and ^{63}Cu-NMR measurements [163]. The spin Peierls transition disappeared at Si concentration $y \sim 1$ % and a Néel ground state appeared at $0.5 \lesssim y \lesssim 5$ %. The phase diagram for the Si-doped compounds is similar to that of the Zn-doped systems (Fig.53), with the T_N-maximum concentration shifted from $x = 4$% to $y = 2$% for the Si doping.

Poirier *et al.* measured elastic constants in high magnetic fields and obtained an $H-T$ phase diagram for a Si 0.7% doped system [164]. They found that the overall structure of the $H-T$ phase diagram (Fig.54) was similar to the general phase diagram of spin Peierls systems (Fig.51), except that the spin Peierls phase (SP) is split to a SP-phase and a Néel ordered phase (AF).

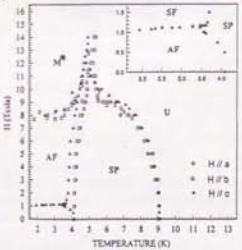

Figure 54:
$H-T$ phase diagram of $Cu(Ge_{1-y}Si_y)O_3$ (y=0.7%). Cite from Ref. [164].

Since a magnetic ordered phase is expected from previous measurements, μSR is a good probe for further investigations of the Zn/Si-doped systems. Previously, Tchernyshyov *et al.* [165] and García-Muñoz *et al.* [166] performed μSR measurements on Zn 4% samples and found a spin-glass-like muon spin relaxation. In the next section, more extensive μSR studies of Zn/Si-doped systems $[(Cu_{1-x}Zn_x)(Ge_{1-y}Si_y)O_3$: $x = 2, 4, 8$ %, and $y = 2$%], are presented in addition to the μSR results from the nominally pure $CuGeO_3$.

6.2.3 μSR measurements

For our μSR measurements, polycrystalline pellets of $(Cu_{1-x}Zn_x)GeO_3$ ($x = 0, 2, 4$ and 8 %) were prepared at the Department of Applied Physics, the University of Tokyo, using the solid state reactions, starting from a stoichiometric mixture of CuO, GeO_2 and, for the Zn-doped compounds, ZnO [167]. Powder X-ray measurements could not detect any impurity phase.

Nominally pure $CuGeO_3$

In Fig.55, μSR spectra of the nominally pure system are shown. There was slow relaxation observed below $T \sim 3$ K, but, as shown by the longitudinal field (LF) measurements in the inset, the relaxation is in the fast fluctuation regime; in the LF measurements, the relaxation was present up to LF$\sim$ 200 G, while the zero-field relaxation rate corresponds to $\delta H \sim 6$ G, if it were caused by static field distribution. (See section 3.4 for μSR spectroscopic technique.) Our μSR measurements of the nominally pure $CuGeO_3$ confirmed the absence of static order down to 50 mK.

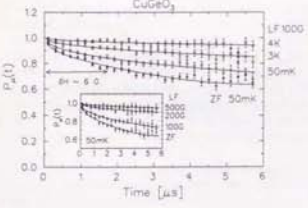

Figure 55:
μSR spectra of the nominally pure $CuGeO_3$. The inset is longitudinal field decoupling measurements to investigate field fluctuations. The solid lines are fits with square-root exponential function, which is appropriate for paramagnetic dilute spin systems (see section 3.2 in Chapter 3).

Zn-doped systems

In Fig.56, zero-field μSR spectra of the Zn-doped compounds are shown. Contrary to the pure system, we observed Gaussian-like muon spin relaxation, suggesting that static local fields are induced by Zn doping. In the ordered phase ($T < T_N$), we confirmed that the spectra converges to the 1/3 of the full amplitude; the existence of the '1/3-component' is an unambiguous signature of static freezing of moments, as has been explained in Chapter 3.

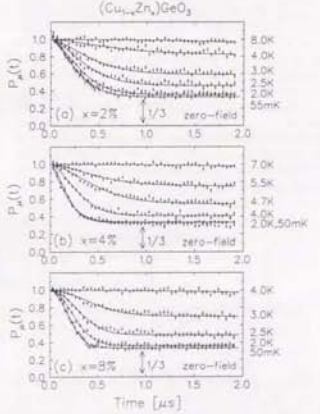

Figure 56:
Zero-field μSR spectra of $(Cu_{1-x}Zn_x)GeO_3$, with Zn concentration $x = 2$ % (a), 4 %(b) and 8 % (c). The solid lines are the phenomenological fits described in the text.

In order to estimate the characteristic field distribution width (Δ/γ_μ), we phenomenologically analyzed the spectra with a stretched exponential function, $P_\mu(t) = \exp(-(\Delta t)^\beta)$. Since the stretching power β represents the shape of the field distribution, we assumed that it is temperature independent; we obtained β from the lowest temperature data and fixed it all through the fit ($\beta = 1.53, 1.61$ and 2.00 for the $x = 2, 4$ and 8 % sample, respectively.) Near the Néel temperature, the relaxation amplitude (or ordered volume fraction) decreased as the temperature go through the transition temperature; this result suggests a distribution of T_N.

We introduced a paramagnetic volume fraction ($f_{\rm para}$), and analyzed the spectra with the functional form of:

$$P_\mu(t) = f_{\rm para} + (1 - f_{\rm para})\{1/3 + 2/3\exp(-(\Delta t)^\beta)\} \quad (58)$$

where the first term represents the muons which land in the paramagnetic volume fraction and the second term, in the ordered fraction. The fits are shown in Fig.56 as the solid lines.

In Fig.57, we show the field width (Δ) and the paramagnetic volume fraction ($f_{\rm para}$) as a function of temperature. The field width (Δ) saturates at low temperatures, being consistent with the static order. In the inset of Fig.57a, the saturation magnitude of the field width [$\Delta(T \to 0)$] are plotted as a function of the Zn concentration (x). It was found that $\Delta(T \to 0)$ mimics the Zn concentration (x) dependence of $T_{\rm N}$ (Fig.53).

The temperature dependence of the paramagnetic fraction ($f_{\rm para}$) suggests a distribution of Néel temperatures; with an assumption of Gaussian distribution to $T_{\rm N}$ ($\approx \exp((T_{\rm N} - \bar{T}_{\rm N})^2/2\delta T_{\rm N}^2)$), the average Néel temperature $\bar{T}_{\rm N}$ and the spread $\delta T_{\rm N}$ have been deduced as shown in Fig.57b.

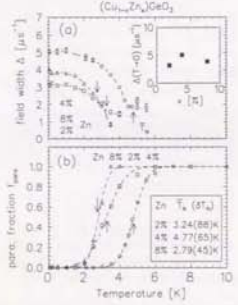

Figure 57:
Temperature dependence of (a) the static field width (Δ) and (b) the paramagnetic fraction ($f_{\rm para}$). The inset of (a) is Zn concentration (x) dependence of the saturated relaxation rate $\Delta(T \to 0)$. The arrows are placed at the average Néel temperatures $\bar{T}_{\rm N}$. The dashed curves in (b) are Gaussian analysis of the distribution in $T_{\rm N}$.

In Fig.58, results of longitudinal field (LF) decoupling measurements are shown. The spectra exhibited the characteristics of static relaxation, namely, time independent muon spin polarization at $t \gtrsim 3/\Delta$ and the decoupling field comparable to the field distribution width (Δ/γ_μ). The solid lines in Fig.58 are static Gaussian Kubo-Toyabe function (eq.19), using the field-width parameter (Δ) obtained from the stretched exponential fit shown in Fig.56b. In small LF's, the Gaussian Kubo-Toyabe function described the recovery at long times relatively well; the deviation at higher LF's may suggest that there exists a larger local field component than true Gaussian distribution assumes.

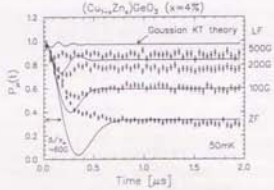

Figure 58:
LF decoupling measurements of the Zn 4% sample at 50 mK. The solid lines are the Gaussian Kubo-Toyabe function (eq.19 in section 3.1).

Si-doped system

Recent technical development at TRIUMF made it possible to measure small specimens, such as $\sim$ 5 mm $\times$ 5 mm single crystal. We measured such single crystals of $Cu(Ge_{1-y}Si_y)O_3$ (y = 2 %), using the newly developed 'low background apparatus', which has an additional particle counter (veto-counter) on the beam path, behind the sample. If a muon misses the sample and hits the veto-counter, it makes a rejection signal so that this event is thrown away. This way, background-free measurements of small crystals has become possible.

A single crystal of Si-doped system $Cu(Ge_{1-y}Si_y)O_3$ (y = 2 %) was synthesized at Laboratoire de Chimie des Solides, Université Paris-Sud (Orsay, France), using the floating zone method. A single crystalline rod ($\phi \sim 3$ mm; long-axis = c-axis) was cleaved to a thickness of $\sim$ 1 mm and tiled, so that the surface area across the muon beam becomes large. We used three such sliced pieces for our measurements.

In Fig.59, μSR spectra of the Si 2% doped system are shown. A spontaneous muon spin precession was observed, indicating the Néel order of the moments.

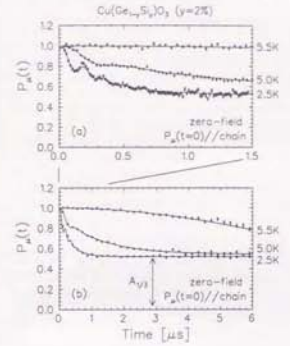

Figure 59:
(a) Zero-field μSR spectra of the Si 2% doped crystal, and (b) the same spectra with longer time range. The solid lines are the fit with the function described in the text (eq.59). The line drawn on the 5.5 K data is a fit with Gaussian Kubo-Toyabe function from nuclear dipolar fields.

We analyzed the spectra with the functional form:

$$P_\mu(t) = A_{1/3} + A_{2/3}^{\rm osc}\exp(-\Delta^{\rm osc}t)\cos(2\pi ft + \phi) + A_{2/3}^{\rm relax}\exp(-\Delta t) \quad (59)$$

$$\text{with } A_{1/3} + A_{2/3}^{\rm osc} + A_{2/3}^{\rm relax} = 1$$

The first term of eq.59 corresponds to the '1/3-component' in polycrystalline measurements; in a single crystal, the direction of the local field depends on the crystal orientation (see Fig.15 in Chapter 3), so that the muon spin component which does not show a precession could be any amplitude ($A_{1/3} \equiv \cos^2\theta$ defined in Fig.15 of Chapter 3). The time-dependent part of the muon spin polarization seems to have two sub-components; one precession signal (the second term of eq.59) and relaxation (the third term).

In Fig.60, we show the precession frequency (f) and the relaxation rate (Δ) as a function of temperature. It was found that relaxation rate (Δ) scales with the precession frequency (f), as shown in the inset of Fig.60. Since the frequency (f) is proportional to the size of the ordered moments, this scaling result indicates that the relaxation (the third term of eq.59) is caused by a distributed local field which reflects the moment size.

A power-law fit ($\approx (T_{\rm N} - T)^\beta$) to the frequency ($f$) and the relaxation rate (Δ) found $T_{\rm N}$ = 5.02(2) K and β = 0.24(2). The exponent (β) is consistent with that of the antiferromagnetic Bragg peak intensity observed in $(Cu_{1-x}Zn_x)GeO_3$ [161].

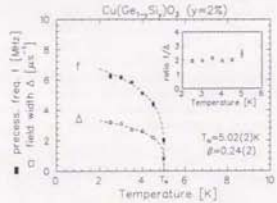

Figure 60:
Temperature dependence of the precession frequency (f) and the relaxation rate (Δ). The dashed line is a power-law fit described in the text. The inset is the ratio f/Δ, which was found to be temperature independent.

6.2.4 Discussion

Absence of precession in the Zn-doped samples

In the Si-doped system, antiferromagnetic order was clearly exhibited as the spontaneous muon precession (Fig.59). In the Zn-doped systems, Néel order was not clear, although an existence of a static order below $T_{\rm N}$ was presented from the '1/3-component' (Fig.56) and the decoupling behaviors in longitudinal-fields (Fig.58). The absence of muon spin precession suggests that our Zn-doped sample has more randomness than the Si-doped crystal.

One apparent randomness of the Zn-doped samples appeared as the distribution of the Néel temperatures (Fig.57). The spread of $T_{\rm N}$, which probably originates from inhomogeneity of the sample, may have smeared out the μSR spectral structures, as discussed in the following.

We may suppose that the spread of $T_{\rm N}$ was caused by an inhomogeneity of the Zn concentration (x). Using the x–T phase diagram shown in Fig.53, the distribution of the Néel temperatures ($\delta T_{\rm N}$) may be mapped to a fluctuation of the Zn concentrations. The result yields $\delta x \sim$ 0.5, 1 and 0.5 % for the x = 2, 4 and 8 % systems, respectively. These variations of the Zn concentrations may be mapped to the spread of the field-width $\delta\Delta$ using the inset of Fig.57; the result becomes

$\delta\Delta/\Delta = 0.16, 0.2$ and 0.04 for the $x = 2, 4$ and 8 % samples, respectively. The above-mentioned spreads are all Gaussian standard deviation.

The μSR spectrum with the spread of internal fields can be obtained from a convolution:

$$P_\mu(t) = \int_0^\infty df \int_0^\infty d\Delta \, \frac{1}{\sqrt{2\pi}\delta f} e^{-\frac{(f-f_0)^2}{2\delta f^2}} \frac{1}{\sqrt{2\pi}\delta\Delta} e^{-\frac{(\Delta-\bar{\Delta})^2}{2\delta\Delta^2}} \times P_\mu^{\rm ideal}(t; f, \Delta) \times (\text{normalizing factor}) \tag{60}$$

where, we assumed the ideal muon relaxation $P_\mu^{\rm ideal}(t; f, \Delta)$ to be the relaxation observed in the Si 2% single crystal (eq.59). In the small inhomogeneity limit ($\delta f/f, \delta\Delta/\Delta \ll 1$), the integral is approximately performed as:

$$P_\mu(t) \approx A_{1/3} + A_{2/3}^{\rm osc} \exp(-(\Delta^{\rm osc} + \pi\delta f)t)\cos(2\pi\bar{f}t + \phi) + A_{2/3}^{\rm relax} \exp(-\bar{\Delta}t) \tag{61}$$

where the precession suffers extra damping as $\Delta^{\rm osc} \to \Delta^{\rm osc} + \pi\,\delta f$, due to the distribution of the frequencies.

In Fig.61, we show a simulated μSR spectrum for the Zn 4% doped system ($\delta f/f \approx \delta\Delta/\Delta = 0.2$), obtained from a numerical integration of eq.60. The precession became less obvious than the Si-doped crystal; this result implies that the macroscopic sample inhomogeneity may be one of the reasons for the absence of muon spin precession in the Zn-doped systems.

The effects of more microscopic randomness, such as substitutions to the spin site with the non-magnetic Zn ions, are not clear at the present stage.

Doping dependence of the size of moment

In the discussion above, the absence of muon spin precession in the Zn doped system was attributed to the macroscopic sample inhomogeneity. This discussion, at the same time, expects a muon spin relaxation in the Zn doped system with its rate mostly determined by the average relaxation rate $\bar{\Delta}$. Contrary to the precession, this relaxation rate is robust to the sample inhomogeneity, as shown in Fig.61. Since in the Si-doped crystal the relaxation rate Δ was found to be proportional to the size of moments (Fig.60), the relaxation rates measured in the Zn-doped samples should also reflect the average size of the ordered moments.

As shown in the inset of Fig.57, the saturated relaxation rate $[\Delta(T\to 0)]$ takes a maximum at the optimum doping concentration. The increase of $\Delta(T\to 0)$ in the Zn 'under-doped' regime indicates a creation of static moments upon doping, being consistent with the suppression of $T_{\rm SP}$ and the enhancement of $T_{\rm N}$ (Fig.53). The decrease of $\Delta(T\to 0)$ in the Zn 'over-doped' regime

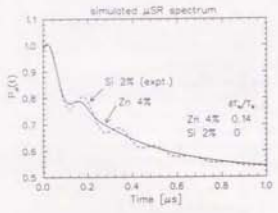

Figure 61:
A simulated μSR spectra for the Zn 4% system. Muon spin precession in our Zn-doped samples should be suppressed because of the trivial sample inhomogeneity. See the text for the simulation procedure.

is partly attributed to trivial dilution of moments due to the Zn substitutions; even if the size of ordered moments doesn't change upon Zn doping, the muon relaxation rate should decrease as $\Delta(x) \sim \Delta_0(1-x)$, simply because of the decrease in the number of spins. Still, the experimental result suggests more pronounced decrease; the relaxation rate decreased by ~ 20 % [$\Delta(T\to 0) \sim 5 \to 4\,\mu{\rm s}^{-1}$] in the change of Zn concentration $x = 4 \to 8$ %. This result suggests that the ordered moments shrinks in the Zn over-doped regime.

6.3 Summary

We have presented with μSR that the Zn/Si-doped $CuGeO_3$ exhibits static order. In the Si-doped $Cu(Ge_{1-y}Si_y)O_3$ crystal (y=2%), Néel order was clearly observed with spontaneous muon spin precession. The critical exponent (β) of the order parameter was found to be the same with the previously-reported value for a Zn-doped crystal, suggesting a universal ordering mechanism between the Si and Zn doping.

In the μSR measurements of the Zn-doped polycrystalline pellets, Néel order was not clear, probably due to a macroscopic sample inhomogeneity. From the static muon spin relaxation rate, the size of the ordered moments were proposed to mimic the Zn concentration dependence of the Néel temperatures.

7 Concluding remarks

In this thesis work, I have presented μSR investigations of several many-body singlet ground state materials, and studied their response to vacancy/charge doping. Since the spin singlet is a most apparent quantum mechanical state of a spin system, this thesis work was intended to detect how quantum mechanics are realized in macroscopic spin systems. I also presented how quantum mechanical ground states are destroyed upon the perturbations due to doping.

The spin ladder materials $Sr_{n-1}Cu_{n+1}O_{2n}$, which alternate between a classical and quantum mechanical ground state were presented first. The experimental results supported the theoretical predictions about the ground state structures; the spin-gapped, non-magnetic ground state for the 2-leg ladder system, and a gap-less, ordered ground state for the 3-leg system.

The Haldane material Y_2BaNiO_5 was confirmed to take the non-magnetic ground state. With the Mg doping to the Cu site, this ground state was found to be stable against the vacancy doping on the spin chain. If positive charge is introduced to the chain, though, the non-magnetic ground state was strongly perturbed; on a *macroscopic* time scale, the system exhibited a spin-glass like signature, such as history dependent susceptibilities. On the other hand, on a *microscopic* time scale, however, the spins kept fluctuating down to milli-Kelvin regime in a unconventional way. If one calls a fluctuating spin ground state a 'spin liquid', the charge doped Haldane system may be called as a 'viscous' spin liquid.

The spin Peierls material $CuGeO_3$ exhibited a non-magnetic ground state. But, with a small amount of non-magnetic perturbation, a classical ground state was induced to appear; well defined Néel order was confirmed with a spontaneous muon spin precession in a Si-doped single crystal.

The experimental results presented in this thesis may be summarized as in the next table:

Table 6: The ground state of spin systems

system	pure	doping	
		vacancy	charge
3-leg ladder	Néel/SG	?	?
2-leg ladder	non-mag.	?	?
Haldane	non-mag.	non-mag.	*viscous* liquid
spin Peierls	non-mag.	Néel order	?

In all of the singlet ground state materials investigated, the non-magnetic ground state was realized in the pure systems, and it induced muon spin relaxation in the fast fluctuation regime. But, when vacancy and/or charge is doped, the response to these perturbations seems to reflect the characters of the individual spin systems. For example, with a small amount of vacancy introduced to the chain, the spin Peierls material $(Cu_{1-x}Zn_x)GeO_3$ exhibited bulk Néel order, while the Haldane material $Y_2Ba(Ni_{1-y}Mg_y)O_5$ preserved the singlet ground state. The contrasting response to the vacancy doping may reflect the difference in the ground state structures; it seems that the ground state constituent of isolated singlet pairs are unstable against vacancy doping. To test this hypothesis, μSR investigations of the Zn-doped 2-leg ladder materials $Sr(Cu_{1-x}Zn_x)_2O_3$ is underway.

The experimental results presented in this thesis may be summarized in the next figure:

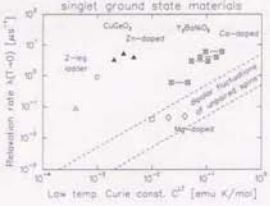

Figure 62:
Muon spin relaxation rate in the ground state $\lambda(T\to 0)$, as a function of low temperature Curie constant $C^{\rm LT}$. The open symbols correspond to relaxation in fast fluctuation regime; the closed symbols, to the static relaxation. The symbols with a cross inside indicates unconventionally dynamic relaxation. The dashed lines are the estimate of the paramagnetic relaxation rate due to doping induced unpaired moments. (see the second subsection of section 5.2.3.)

In this plot, the horizontal axis represents characteristic magnitude of perturbations to the system; if a singlet ground state is doped with vacancy and/or charge, the dopant creates unpaired spins which manifest themselves as the low temperature Curie term. The vertical axis reflects how the singlet ground state is perturbed upon doping; if majority of the moments remain singlet and muons detect the dipolar fields from the doping induced local moments, the plot should fall in the region of dashed lines. The pure/vacancy doped Haldane system $Y_2Ba(Ni_{1-y}Mg_y)O_5$ seems to realize this situation. If the system shows bulk magnetic order, the relaxation becomes static (closed symbols) with a saturated relaxation rate, as the Zn doped $CuGeO_3$ exhibited.

One interesting question is why the pure $CuGeO_3$ and the 2-leg ladder system $SrCu_2O_3$ doesn't fall in the dashed-line region. There may be two explanations; (1) the native unpaired spins are already correlated and their fluctuation rate (ν) becomes slow, and (2) muon itself works as an impurity to the system, and creates unpaired spins around it; namely, the dipolar field width (a) at the muon site becomes larger than that from the native unpaired spins observed in susceptibility. In the 2-leg ladder system, the enhanced dipolar field widths (a) estimated from the longitudinal field measurements (Table 4 in Chapter 4) seem to suggest a possibility of the latter case, namely, a muon-impurity effect.

Among all the results presented in this thesis, the most interesting one is the unconventional spin dynamics of the charge doped Haldane system. Since this problem involves two degrees of freedom, namely, the 'spin' and the 'charge', theoretical understanding may be challenging. But this system should contain interesting dynamical features inside.

Acknowledgments

The author would like to express sincere thanks to Professor Yasutomo J. Uemura, who, not only introduced me μSR investigations of the spin systems in this thesis, but also gave me precious hints through the discussions. I learned from him that *qualitative* understanding of a physical system is much more important than quantitative discussions. I would also like to thank Professor Graeme M. Luke, who carefully read my thesis manuscript and gave me relevant remarks, which improved the physics and the logics in this thesis.

I would also like to express a sincere gratitude to Professor Kanetada Nagamine, who introduced me the μSR technique five years ago. At KEK/UTMSL muon facility, I learned from him that muon is effective not only as a microscopic probes to spin systems, but also in wider fields, such as nuclear, atomic and geophysical researches. At KEK/UTMSL muon facility, Professor Kusuo Nishiyama educated me on the technical aspects of μSR measurements, as well as theoretical basics of spin relaxation in solids. I would like to thank him for these points.

The measurements presented in this thesis is based on collaborations. The group lead by Professor Shinichi Uchida at the University of Tokyo provided the specimen of $(Y_{2-x}Ca_x)Ba(Ni_{1-y}Mg_y)O_5$. I would like to express special thanks to two Professors Shinichi Uchida and Hidenori Takagi, as well as to their students Mr. Kenjirou Kiyono and Mr. Shigeki Miyasaka, for giving us the opportunity to measure their specimens.

The spin ladder materials $Sr_{n-1}Cu_{n+1}O_{2n}$ were provided from the group lead by Professor Mikio Takano at Kyoto University. I would like to express sincere thanks to him and Dr. Masaki Azuma for preparing the specimens, which took their several weeks to accumulate the amount necessary for the μSR measurements. Also, I would like to thank Professor Takano for having invited me to an informal meeting at his group in February of 1995. The discussions at the meeting was quite educational for me.

The group lead by Professor Kunimitsu Uchinokura at the University of Tokyo provided us the spin Peierls materials $(Cu_{1-x}Zn_x)GeO_3$. I would like to thank him, Dr. Masashi Hase and Mr. Yoshitaka Sasago for their sample preparations. It should be mentioned that they kindly invented a new sinter technique of the powder samples, so that our measurements using the dilution refrigerator became possible. For the $Cu(Ge_{1-y}Si_y)O_3$ crystals, we owe to the group lead by Professor A. Revcolevschi at Université Paris-Sud. I would like to thank them for the collaboration.

Being a beam experiment, the μSR measurements themselves involved many collaborators. I would like to thank the former members of the Columbia University μSR group, Drs. Liang Ping Le, Amit Keren and Weidong Wu, as well as the current members, Ben Nachumi, Oleg Tchernyshyov, Mike Larkin and Jack Merrin for taking the shift works during the beam time. Among them, I would also like to thank especially Ben Nachumi and Mike Larkin for their critical reading of and comments to this thesis. I also would like to thank to the exciting discussions with the TRIUMF people, Professors Jess Brewer and Rob Kiefl, Drs. Syd Kreitzman, Kim Chow, Bessam Hitti, Andrew MacFarlane and Sarah Dunsiger. Some of the measurements in this thesis became possible owing to the recent technical developments at TRIUMF, which are contribution of these TRIUMF people and the μSR technician/engineers Kieth Hoyle, Curtis Ballard and Mel Good, as well as other technical staffs of TRIUMF.

This thesis is dedicated to my fiancée Chisato Mochizuki,
who encouraged me with her love, across the time-difference and the pacific ocean.

A Appendix

A.1 Extended Lieb-Shultz-Mattis Theorem [8]

This theorem claims that there is no gap between the ground state and the excited states, if the ground state of the one-dimensional Heisenberg model is unique and the the spin is half-odd-integer. The idea of the following proof is (1) to make a state with an energy that approaches the ground state energy as the lattice size $L \to \infty$, and then (2) to confirms that this state is orthogonal to the ground state [8].

The underlying spin system is a one-dimensional Heisenberg model, with an even number of spins $2L$ and a cyclic boundary condition ($\boldsymbol{S}_{-L} \equiv \boldsymbol{S}_L$). A low-lying state |twist> is prepared by introducing a 2π twist over an odd number of spins ($2r+1$) in the ground state |0>, as shown in Fig.63.

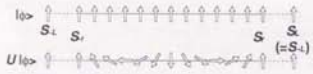

Figure 63:
A schematic view of the twisting operation.

The low-lying state is mathematically expressed as:

$$|\text{twist}> \;=\; U|0> \qquad (62)$$

where

$$U \;=\; \exp\left(\sum_{j=-r}^{r} i\theta_j S_j^z\right), \;\; \theta_j = (\frac{j}{r}+1)\pi \qquad (63)$$

The energy increase of the twisted state measured from the ground state is

$$\begin{aligned}
\delta E \;&=\; <\text{twist}|\mathcal{H}|\text{twist}> - <0|\mathcal{H}|0> \\
&=\; <0|(\mathcal{U}^{-1}\mathcal{H}\mathcal{U} - \mathcal{H})|0> \\
&=\; \frac{1}{2}J\sum_{j=-r}^{r} <0|\left\{(e^{i\frac{\pi}{r}}-1)S_j^+S_{j+1}^- + h.c.\right\}|0> \\
&=\; \frac{1}{2}J(\cos\frac{\pi}{r}-1)\sum_{j=-r}^{r} <0|S_j^+S_{j+1}^- + h.c.|0> \\
&\sim\; \mathcal{O}(\frac{1}{r^2})\mathcal{O}(r) \\
&=\; \mathcal{O}(\frac{1}{r})
\end{aligned} \qquad (64)$$

Hence, by selecting the twist length $r = L-1$, the energy of the twisted state (δE) becomes infinitesimal small as $L \to \infty$.

This result does not necessarily mean that the system is gapless, because the twisted state |twist> may possibly contain much of the ground state, and the δE may not estimate the energy of the excited states. Only after one proves that the twisted state |twist> is orthogonal to the ground state |0>, can one say that the system does not have a gap. For the half-odd-integer spin system, the proof is as follows.

First, one defines a unitary operator $\mathcal{R}$, which is a combination of space inversion and π-rotation about the y-axis in the spin space:

$$\mathcal{R}(S_j^x, S_j^y, S_j^z)\mathcal{R}^{-1} \;=\; (-S_{-j}^x, S_{-j}^y, -S_{-j}^z) \qquad (65)$$

Since the ground state is unique, and the Heisenberg Hamiltonian is invariant for space inversion and rotation in the spin space, the ground state is transformed to itself:

$$\mathcal{R}|0> \;=\; |0> \qquad (66)$$

On the other hand, the twisted state is transformed as:

$$\begin{aligned}
\mathcal{R}|\text{twist}> \;&=\; \mathcal{R}U\mathcal{R}^{-1}\mathcal{R}|0> \\
&=\; \exp(-\sum_{j=-r}^{r} i\theta_j S_{-j}^z)|0> \\
&=\; \exp(-2\pi i\sum_{j=-r}^{r} S_j^z)|\text{twist}> \\
&=\; \begin{cases} +|\text{twist}> & S : \text{integer} \\ -|\text{twist}> & S : \text{half odd integer} \end{cases}
\end{aligned} \qquad (67)$$

The factor $\exp(-2\pi i\sum S_j^z)$ rotates the $(2r+1)$ spins in the twist by 2π. In the case of half-odd-integer spins, this factor is -1 ($= (-1)^{2r+1}$), and the twisted state |twist> is orthogonal to the ground state |0> ($<0|\text{twist}> = <0|\mathcal{R}^{-1}\mathcal{R}|\text{twist}> = -<0|\text{twist}>$).

For the integer spins, the above argument says nothing about the overlap <twist|0>, and hence, the Lieb-Shultz-Mattis theorem does not exclude the existence of the Haldane gap.

A.2 The 10/3 effect [9, 10]

This section considers nuclear spin relaxation in a paramagnetic localized spin system, with the interaction between the moments described by the dipolar fields.

We assume the Hamiltonian of the spin system to be:

$$\mathcal{H} \;=\; \hbar\gamma_e\sum_i\left(H_0 S_i^z + \sum_j D_{ij}\boldsymbol{S}_i\boldsymbol{S}_j\right) \qquad (68)$$

where, H_0 is the external magnetic field applied in the z-direction, $\boldsymbol{S}_i$ is the spin of the i-th localized electron

and D_{ij} represents the tensor for the dipolar interaction, namely,

$$\begin{aligned}
&D_{ij}\boldsymbol{S}_i\boldsymbol{S}_j \\
&\;=\; \frac{\hbar\gamma_e}{|\boldsymbol{r}_{ij}|^3}\{\boldsymbol{S}_i\cdot\boldsymbol{S}_j - 3(\boldsymbol{S}_i\cdot\boldsymbol{r}_{ij})(\boldsymbol{S}_j\cdot\boldsymbol{r}_{ij})\}
\end{aligned} \qquad (69)$$

where, $\boldsymbol{r}_{ij} = \boldsymbol{r}_j - \boldsymbol{r}_i$ is the distance between the i-th and the j-th electrons and $\boldsymbol{r}_{ij} = \boldsymbol{r}_{ij}/|\boldsymbol{r}_{ij}|$ is the unit vector parallel to the distance.

It is easily shown that the fluctuation rate (ν) of the electron moments doesn't depend on the external field; if one writes the Hamiltonian (eq.68) in the rotating reference frame (RRF) for the electrons, one can eliminate the external field, while the dipolar interaction is expressed as:

$$\begin{aligned}
&\mathcal{H}_D^{RRF} \\
&\;=\; e^{-i\mathcal{H}_0 t/\hbar}(\mathcal{H}_D)e^{+i\mathcal{H}_0 t/\hbar} \\
&\;=\; e^{-i\mathcal{H}_0 t/\hbar}\left(\sum_{ij} D_{ij}\boldsymbol{S}_i\boldsymbol{S}_j\right)e^{+i\mathcal{H}_0 t/\hbar} \\
&\;=\; \sum_{ij} D_{ij}(e^{-i\mathcal{H}_0 t/\hbar}\boldsymbol{S}_i e^{+i\mathcal{H}_0 t/\hbar}) \\
&\qquad\qquad \times (e^{-i\mathcal{H}_0 t/\hbar}\boldsymbol{S}_j e^{+i\mathcal{H}_0 t/\hbar}) \\
&\;=\; \sum_{ij} D_{ij}\boldsymbol{S}_{i,R}\boldsymbol{S}_{j,R}
\end{aligned} \qquad (70)$$

where $\mathcal{H}_0$ is the first term of the Hamiltonian (eq.68) and $\boldsymbol{S}_{i,R}$ the RRF representation of the spin $\boldsymbol{S}_i$. This result indicates that the dipolar interaction between the electrons (namely the associated fluctuation rate ν) doesn't change in RRF, because the interacting two spins $\boldsymbol{S}_j$ and $\boldsymbol{S}_i$ have the same gyromagnetic ratio, and conduct coherent precession in the external field H_0.

To the probe nuclear spin, the Larmor precession of the electron moment in a reasonably large external field H_0 is so fast that its xy components becomes invisible (Fig.64). In this limit, the probe spin detects only the z-component of the electron moments, which changes its length with the dipolar fluctuation rate (ν). In this situation, the T_1 relaxation rate of the probe spin may be reduced by $\sim 1/3$ from that in the zero-field case, because the average size of the z-component squared is 1/3 of the full spin: $< (S^z)^2 >= 1/3\,S^2$. As shown below, the precise factor is 3/10.

Generally, the T_1 relaxation rate of a probe nuclear spin is expressed as [34]:

$$\begin{aligned}
&T_1^{-1} \\
&\;=\; \frac{\gamma_n^2}{2}\int_{-\infty}^{\infty} e^{-i\omega_n\tau}d\tau < H_\mu^x(0)H_\mu^x(t) + H_\mu^y(0)H_\mu^y(t) > \\
&\;=\; \frac{\gamma_n^2}{2}\int_{-\infty}^{\infty} e^{-i\omega_n\tau}d\tau < H_\mu^+(0)H_\mu^-(t) + H_\mu^-(0)H_\mu^+(t) >
\end{aligned}$$

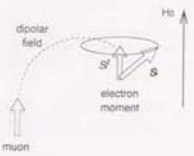

Figure 64:
An electron moment and a muon spin in an external magnetic field (H_0). If the Larmor precession of the electron is fast, muon detects only the z-component of the electron spin S_z'.

where, ω_n is the Larmor precession frequency of the nuclear spin (muon), $H_\mu^a(t)$ ($a = x, y$) is the x, y-component of the fluctuating local fields at the probe spin site and $H_\mu^\pm \equiv H_\mu^x \pm iH_\mu^y$. The bracket $< \cdots >$ denotes the ensemble average. If the muon-electron interaction is the dipolar fields, the local field at the muon site becomes:

$$\begin{aligned}
\boldsymbol{H}_\mu(t) \;&=\; \sum_j D_{\mu j}\boldsymbol{S}_j(t) \\
&=\; \sum_j \frac{\hbar\gamma_e}{r_j^3}\{\boldsymbol{S}_j - 3(\boldsymbol{S}_j\cdot\boldsymbol{r}_j)\boldsymbol{r}_j\}
\end{aligned} \qquad (72)$$

where $\boldsymbol{r}_j$ is the distance between the muon and the j-th electron and $\boldsymbol{r}_j$ is the unit vector parallel to the distance.

To write $H_\mu^\pm(t)$, it is convenient to define $r_j^\pm \equiv r_j^x \pm ir_j^y$, where, r_j^a ($a = x, y$) is the x, y-component of the unit vector $\boldsymbol{r}_j$. The local fields are expressed as:

$$\begin{aligned}
&H_\mu^\pm \\
&\;=\; \sum_j \frac{\hbar\gamma_e}{r_j^3}\{S_j^\pm - 3(\boldsymbol{S}_j\cdot\boldsymbol{r}_j)r_j^\pm\} \\
&\;=\; \sum_j \frac{\hbar\gamma_e}{r_j^3}\{S_j^\pm - 3\left(\frac{1}{2}(S_j^\pm r_j^\mp + S_j^\mp r_j^\pm) + S_j^z r_j^z\right)r_j^\pm\} \\
&\;=\; \sum_j \frac{\hbar\gamma_e}{r_j^3}\{\underbrace{\left(1 - \frac{3}{2}r_j^\mp r_j^\pm\right)}_{A_j^\pm}S_j^\pm + \underbrace{\left(-\frac{3}{2}r_j^\pm r_j^\pm\right)}_{B_j^\pm}S_j^\mp \\
&\qquad\qquad + \underbrace{(-3r_j^z r_j^\pm)}_{C_j^\pm}S_j^z\}
\end{aligned} \qquad (73)$$

Using the rotating reference frame (RRF) for the electrons, the electron spin correlations $< S_j^a(0)S_k^b(t) >$ ($a, b = \pm, z$) are expressed as:

$$(71) \quad < S_j^a(0)S_k^\pm(t) > \;=\; e^{\pm i\omega_0 t} < S_{j,R}^a(0)S_{k,R}^\pm(t) >$$

$$< S^a_{j,R}(0)S^a_{k,R}(t) > \;=\; < S^a_{j,R}(0)S^z_{k,R}(t) > \qquad (74)$$

where ω_0 is the electron Larmor frequency, $S^a_{j,R}(t)$ ($a = \pm, z$) is the electron spins expressed in the RRF. Assuming a Markoffian fluctuation processes, decay of the spin correlation is expressed as

$$\begin{aligned} &< S^z_{j,R}(0)S^b_{k,R}(t) > \\ &= \exp(-\nu t) < S^a_{j,R}(0)S^b_{k,R}(0) > \end{aligned} \qquad (75)$$

where ν is the dipolar fluctuation rate, and $a, b = \pm, z$. In paramagnetic state, there is no correlation between the j-th and the k-th spin, yielding the $t = 0$ correlation functions as:

$$< S^+_{j,R}(0)S^+_{k,R}(0) > \;=\; \frac{2}{3}S(S+1)\delta_{jk} \qquad (76)$$

$$< S^z_{j,R}(0)S^z_{k,R}(0) > \;=\; \frac{1}{3}S(S+1)\delta_{jk} \qquad (77)$$

$$< S^+_{j,R}(0)S^+_{k,R}(0) > \;=\; 0 \qquad (78)$$

$$< S^z_{j,R}(0)S^z_{k,R}(0) > \;=\; 0 \qquad (79)$$

Using the above presented expressions, the field correlation at the probe spin site becomes:

$$\begin{aligned} &< H^+_\mu(0)H^-_\mu(t) > \\ &= \exp(-\nu t) \\ &\quad \times \sum_{jk} \frac{(\hbar\gamma_e)^2}{r_j^3 r_k^3}\{A^0_j A^0_k < S^+_{j,R}(0)S^-_{k,R}(0) > e^{-i\omega_0 t} \\ &\qquad + B^+_j B^-_k < S^-_{j,R}(0)S^+_{k,R}(0) > e^{+i\omega_0 t} \\ &\qquad + C^+_j C^-_k < S^z_{j,R}(0)S^z_{k,R}(0) >\} \\ &= \frac{2}{3}S(S+1)(\hbar\gamma_e)^2 \sum_j r_j^{-6}\exp(-\nu t) \\ &\qquad \times \{(A^0_j)^2 e^{-i\omega_0 t} + (B^+_j B^-_j)e^{+i\omega_0 t} + \frac{1}{2}C^+_j C^-_j\} \end{aligned} \qquad (80)$$

In the same manner, $< H^-_\mu(0)H^+_\mu(t) >$ is calculated, yielding the T_1 relaxation rate as:

$$\begin{aligned} &T_1^{-1} \\ &= \frac{2}{3}S(S+1)\gamma_\mu^2(\hbar\gamma_e)^2 \sum_j r_j^{-6}\int_{-\infty}^{\infty} e^{-i\omega_0 t}dt\exp(-\nu t) \\ &\qquad \times\{((A^0_j)^2 + B^+_j B^-_j)\cos(\omega_0 t) + \frac{1}{2}C^+_j C^-_j\} \end{aligned} \qquad (81)$$

In an isotropic sample, the coefficients are replaced by the angular averages:

$$(A^0_j)^2 \;=\; \left(1 - \frac{3}{2}r^+_j r^-_j\right)^2 \to \frac{1}{5} \qquad (82)$$

$$B^+_j B^-_j \;=\; \left(-\frac{3}{2}r^+_j r^+_j\right)\left(-\frac{3}{2}r^-_j r^-_j\right) \to \frac{6}{5} \qquad (83)$$

$$C^+_j C^-_j \;=\; \frac{1}{2}(-3r^z_j r^-_j)(-3r^z_j r^+_j) \to \frac{6}{5} \qquad (84)$$

Introducing the dipolar field width (Δ) defined in eq.45, the T_1 relaxation yields:

$$\begin{aligned} &T_1^{-1} \\ &= 2\Delta^2 \int_{-\infty}^{\infty} e^{-i\omega_\mu t}dt\exp(-\nu t)\left(\frac{7}{10}\cos(\omega_0 t) + \frac{3}{10}\right) \\ &= \frac{3}{10}\frac{2\Delta^2\nu}{\nu^2 + \omega_\mu^2} \\ &\quad + \frac{7}{20}\left(\frac{2\Delta^2\nu}{\nu^2 + (\omega_0 + \omega_\mu)^2} + \frac{2\Delta^2\nu}{\nu^2 + (\omega_0 - \omega_\mu)^2}\right) \qquad (85) \\ &\to \frac{3}{10} \times \frac{2\Delta^2\nu}{\nu^2 + \omega_\mu^2} \quad \text{(high field limit)} \qquad (86) \end{aligned}$$

Namely, if the Larmor precession of the electron moments are fast, the local field width at the muon site is effectively reduced to $\Delta^{\rm LF} = \sqrt{3/10}\,\Delta^{\rm ZF}$.

A.3 Relaxation function in Néel state with randomness[‡]

In the true Néel state, a muon spin exhibits a Larmor precession. In a randomly frozen spin system, it exhibits the Gaussian Kubo-Toyabe function. In the following, an intermediate situation between these cases is considered.

If a spin system is frozen almost randomly, but having a non-zero sublattice magnetization (Fig.65), the local field at muon site will be a Gaussian distribution around a static field:

$$p(\boldsymbol{H}) \;=\; p_G(\boldsymbol{H} - \boldsymbol{H}_0) \qquad (87)$$

where, $p_G(\boldsymbol{H})$ is the isotropic Gaussian distribution induced by the randomly frozen spin component and $\boldsymbol{H}_0$ is a well defined static field from the Néel ordered component.

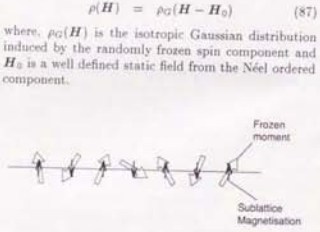

Figure 65:
A Néel order with randomness. Each spin bears a sublattice magnetization, but the remaining spin component is randomly frozen.

Muon spin relaxation in this field distribution is expressed as:

$$G^{\rm GKT+H_0}(t;\Delta,\boldsymbol{H}_0)$$

[‡]This section is based on the author's original work: K. Kojima, *unpublished*.

$$\begin{aligned} &= \int d\boldsymbol{H}_0 \int d\boldsymbol{H}\, p_G(\boldsymbol{H} - \boldsymbol{H}_0)S_\mu(t;\boldsymbol{H}) \\ &= \int d\boldsymbol{H}_0 \int d\boldsymbol{H}\left(\frac{\gamma_\mu}{\sqrt{2\pi}\Delta}\right)^3 \exp\left(-\frac{\gamma_\mu^2(\boldsymbol{H} - \boldsymbol{H}_0)^2}{2\Delta^2}\right) \\ &\quad \times\left(\frac{H_z^2}{H^2} + \frac{H_x^2 + H_y^2}{H^2}\cos\gamma_\mu|\boldsymbol{H}|t\right) \end{aligned} \qquad (88)$$

where the integral about $\boldsymbol{H}_0$ is taken over the sample geometry. In a polycrystalline sample ($|\boldsymbol{H}_0| = H_0$, isotropic) , the integral about $\boldsymbol{H}_0$ is analytically performed, yielding the muon relaxation as:

$$\begin{aligned} &G^{\rm GKT+H_0}(t;\Delta,H_0) \\ &= \int_0^{2\pi} d\phi \int_{-1}^{1} d\cos\theta \int_0^{\infty} H^2 dH \left(\frac{\gamma_\mu}{\sqrt{2\pi}\Delta}\right)^3 \\ &\quad \times\frac{(\Delta/\gamma_\mu)^2}{2HH_0}\left(e^{-\frac{\gamma_\mu^2(H-H_0)^2}{2\Delta^2}} - e^{-\frac{\gamma_\mu^2(H+H_0)^2}{2\Delta^2}}\right) \\ &\quad \times(\cos^2\theta + \sin^2\theta\cos\gamma_\mu Ht) \end{aligned} \qquad (89)$$

Here, the integral over $\boldsymbol{H}$ is expressed in polar coordinate. Since the Gaussian distribution is isotropic, the angular part is easily integrated; it gives the 1/3 and 2/3 components. The integral of the radial part is also performed analytically:

$$\begin{aligned} &G^{\rm GKT+H_0}(t;\Delta,H_0) \\ &= \frac{1}{3} + \frac{2}{3}\int_{-\infty}^{\infty}\frac{\gamma_\mu}{\sqrt{2\pi}\Delta}\frac{HdH}{H_0}e^{-\frac{\gamma_\mu^2(H-H_0)^2}{2\Delta^2}}\cos\gamma_\mu Ht \\ &= \frac{1}{3} + \frac{2}{3}\left(\cos\gamma_\mu H_0 t - \frac{\Delta}{\gamma_\mu H_0}\Delta t\sin\gamma_\mu H_0 t\right) \\ &\quad \times\exp\left(-\frac{1}{2}\Delta^2 t^2\right) \end{aligned} \qquad (90)$$

In the $H_0 \to 0$ limit, this function becomes the Gaussian Kubo-Toyabe function (eq.18), and in the large H_0 limit, it exhibits a damped oscillation with a frequency associated with H_0. In Fig.66, the function obtained $G^{\rm GKT+H_0}(t)$ is drawn for various H_0. A crossover from the Gaussian Kubo-Toyabe behavior to a damped oscillation is shown.

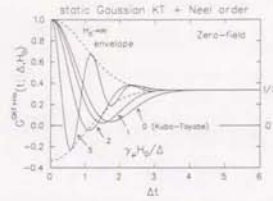

Figure 66:
Behavior of the Gaussian Kubo-Toyabe function with a static local field H_0. The dashed lines are the envelope for the damped oscillation in the large H_0 limit.

References

[1] K. Kojima, A. Keren, G. M. Luke, B. Nachumi, W. D. Wu, Y. J. Uemura, M. Azuma, and M. Takano. *Phys. Rev. Lett.*, **74**, 2812, (1995).

[2] K. Kojima, A. Keren, L. P. Le, G. M. Luke, W. D. Wu, Y. J. Uemura, K. Kiyono, S. Miyasaka, H. Takagi, and S. Uchida. *Phys. Rev. Lett.*, **74**, 3471, (1995).

[3] K. Kojima, A. Keren, L. P. Le, G. M. Luke, W. D. Wu, Y. J. Uemura, K. Kiyono, S. Miyasaka, H. Takagi, and S. Uchida. *J. Mag. Mag. Matrs.*, **140-144**, 1657, (1995).

[4] T. Toyabe. Master's thesis, Univ. of Tokyo, (1966).

[5] R. Kubo and T. Toyabe. In R. Blinc, editor, *Magnetic Resonance and Relaxation*, North-Holland, Amsterdam, (1967).

[6] R. S. Hayano, Y. J. Uemura, J. Imazato, N. Nishida, T. Yamazaki, and R. Kubo. *Phys. Rev. B*, **20**, 850, (1979).

[7] Y. J. Uemura, T. Yamazaki, D. R. Harshman, M. Senba, and E. J. Ansaldo. *Phys. Rev. B*, **31**, 546, (1985).

[8] I. Affleck and E. H. Lieb. *Lett. Math. Phys.*, **12**, 57, (1986).

[9] P. W. Anderson and P. R. Weiss. *Rev. Mod. Phys.*, **25**, 269, (1953).

[10] R. Kubo and K. Tomita. *J. Phys. Soc. Jpn.*, **9**, 888, (1954).

[11] H. A. Bethe. *Z. Phys.*, **71**, 205, (1931).

[12] P. W. Anderson. *Matterials Res. Bull.*, **8**, 153, (1973).

[13] J. des Cloizeaux and J. J. Pearson. *Phys. Rev.*, **128**, 2131, (1962).

[14] H. M. McConnell and R. J. Lynden-Bell. *J. Chem. Phys.*, **36**, 2393, (1963).

[15] D. D. Thomas, H. Keller, and H. M. McConnell. *J. Chem. Phys.*, **39**, 2321, (1962).

[16] D. B. Chesnut. *J. Chem. Phys.*, **46**, 4677, (1966).

[17] S. Inagaki and H. Fukuyama. *J. Phys. Soc. Jpn.*, **52**, 3620, (1983).

[18] S. Inagaki and H. Fukuyama. *J. Phys. Soc. Jpn.*, **53** , 4386, (1984).

[19] T. M. Rice, S. Gopalan, and M. Sigrist. *Europhys. Lett.*, **23**, 445, (1993).

[20] T. Barnes, E. Dagotto, J. Riera, and E. S. Swanson. *Phys. Rev. B*, **47**, 3196, (1993).

[21] S. Gopalan, T. M. Rice, and M. Sigrist. *Phys. Rev. B*, **49**, 8901, (1994).

[22] F. D. M. Haldane. *Phys. Lett.*, **93A**, 464, (1983).

[23] F. D. M. Haldane. *Phys. Rev. Lett.*, **50**, 1153, (1983).

[24] I. Affleck, T. Kennedy, E. H. Lieb, and H. Tasaki. *Phys. Rev. Lett.*, **59**, 799, (1987).

[25] I. Affleck, T. Kennedy, E. H. Lieb, and H. Tasaki. *Commun. Math. Phys.*, **115**, 477, (1988).

[26] S. Knabe. *J. Stat. Phys.*, **52**, 627, (1988).

[27] T. Kennedy, E. H. Lieb, and H. Tasaki. *J. Stat. Phys.*, **53**, 383, (1988).

[28] A. Schenck. *Muon Spin Rotation Spectroscopy*. Adam Hilger Ltd, Bristol and Boston, (1985).

[29] L. B. Okun. *Weak Interactions of Elementary Particles*. Pergamon, Oxford, (1965).

[30] M. Motokawa, H. Nojiri, K. Nishiyama, K. Nagamine, and T. Yosida. *Physica B*, **177**, 389, (1992).

[31] K. Nagamine, Y. Miyake, K. Shimomura, P. Birrer, J. P. Marangos, M. Iwasaki, P. Strasser, and T. Kuga. *Phys. Rev. Lett.*, **74**, 4811, (1995).

[32] S. Chu, A. P. Mills, Jr., A. Yodh, K. Nagamine, Y. Miyake, and T. Kuga. *Phys. Rev. Lett.*, **60**, 101, (1988).

[33] R. F. Kiefl, J. W. Schneider, H. Keller, W. Kündig, W. Odermatt, B. D. Patterson, K. W. Blazey, T. L. Estle, and S. L. Rudaz. *Phys. Rev. B*, **32**, 530, (1985).

[34] C. P. Slichter. *Principles of Magnetic Resonance*. Springer-Verlag, (1990).

[35] R. Kadono *et al.*. *Phys. Rev. B*, **39**, 23, (1989).

[36] R. Kubo. *J. Phys. Soc. Jpn.*, **9**, 935, (1954).

[37] A. Keren. *Phys. Rev. B*, **50**, 10039, (1994).

[38] R. W. Walstedt and L. R. Walker. *Phys. Rev. B*, **9**, 4857, (1974).

[39] R. Kubo. *Hyperfine Interaction*, **8**, 731, (1981).

[40] I. A. Campbell, A. Amato, F. N. Gygax, D. Herlach, A. Schenck, R. Cywinski, and S. H. Kilcoyne. *Phys. Rev. Lett.*, **72**, 1291, (1994).

[41] J. G. Bedonorz and K. A. Müller. *Z. Phys.*, **64**, 189, (1986).

[42] E. H. Lieb and F. Y. Wu. *Phys. Rev. Lett.*, **20**, 1445, (1968).

[43] P. Schlottmann. *Phys. Rev. B*, **36**, 5177, (1987).

[44] E. Dagotto and A. Moreo. *Phys. Rev. B*, **38**, 5087, (1988).

[45] E. Dagotto, J. Riera, and D. Scalapino. *Phys. Rev. B*, **45**, 5744, (1992).

[46] M. Sigrist, T. M. Rice, and F. C. Zhang. *Phys. Rev. B*, **49**, 12058, (1994).

[47] H. Tsunetsugu, M. Troyer, and T. M. Rice. *Phys. Rev. B*, **49**, 16078, (1994).

[48] S. R. White, R. M. Noack, and D. J. Scalapino. *Phys. Rev. Lett.*, **73**, 886, (1994).

[49] Z. Hiroi, M. Azuma, M. Takano, and Y. Bando. *J. of Solid State Chem.*, **95**, 230, (1991).

[50] M. Takano, Z. Hiroi, M. Azuma, and Y. Takeda. *Jpn. J. Appl. Phys. Ser.*, **7**, 3, (1992).

[51] M. Azuma, Z. Hiroi, M. Takano, K. Ishida, and Y. Kitaoka. *Phys. Rev. Lett.*, **73**, 3463, (1994).

[52] K. Ishida *et al.*. *J. Phys. Soc. Jpn.*, **63**, 3222, (1994).

[53] M. Azuma, Z. Hiroi, M. Takano, Y. Bando, and Y. Takeda. *Nature* (London), **356**, 775, (1992).

[54] K. Muraleedharan *et al.*. *Solid State Commun.*, **76**, 727, (1990).

[55] A. Keren, L. P. Le, G. M. Luke, B. J. Sternlieb, W. D. Wu, Y. J. Uemura, S. Tajima, and S. Uchida. *Phys. Rev. B*, **48**, 12926, (1993).

[56] T. Sigrist *et al.*. *Nature* (London), **334**, 231, (1988).

[57] D. Vaknin *et al.*. *Phys. Rev. B*, **39**, 9122, (1989).

[58] A. Keren *et al.*. *J. Mag. Mag. Matrs.*, **140-144**, 1641, (1995).

[59] L. P. Le *et al.*. *Phys. Rev. B*, **48**, 7284, (1993).

[60] H. Fukuyama. *Kotai Butsuri* (in Japanese), **14**, 194, (1979).

[61] R. C. Weast (Editor in Chief). *Handbook of Chemistry and Physics*. CRC Press Inc., Boca Raton, Florida, (1989).

[62] E. H. lieb, T. Shultz, and D. Mattis. *Ann. Phys.*, **16**, 407, (1961).

[63] J. Sólyom. *Phys. Rev. B*, **36**, 8642, (1987).

[64] R. R. O. Singh and M. P. Gelfand. *Phys. Rev. Lett.*, **31**, 2133, (1988).

[65] R. Bottet, R. Jullien, and M. Kolb. *Phys. Rev. B*, **28**, 3914, (1983).

[66] U. Glaus and T. Schneider. *Phys. Rev. B*, **30**, 215, (1984).

[67] H. J. Schultz and T. Ziman. *Phys. Rev. B*, **33**, 6545, (1986).

[68] J. C. Bonner. *J. Appl. Phys.*, **61**, 3941, (1987).

[69] I. Affleck. *Phys. Rev. Lett.*, **62**, 474, (1989).

[70] H. Tasaki. **64**, **64**, 2066, (1990).

[71] T. Sakai and M. Takahashi. *Phys. Rev. B*, **42**, 4537, (1990).

[72] W. J. L. Buyers, R. M. Morra, R. L. Armstrong, M. J. Hogan, P. Gerlach, and K. Hirakawa. *Phys. Rev. Lett.*, **56**, 371, (1986).

[73] M. Steiner, K. Kakurai, J. K. Kjems, D. Petitgrand, and R. Pynn. *J. Appl. Phys.*, **61**, 3953, (1987).

[74] I. A. Zaliznyak, L. P. Regnault, and D. Petitgrand. *Phys. Rev. B*, **50**, 15824, (1994).

[75] J. P. Renard *et al.*. *Europhys. Lett.*, **3**, 945, (1987).

[76] J. P. Renard *et al.*. *J. Appl. Phys.*, **63**, 3538, (1988).

[77] V. Gadet *et al.*. *Phys. Rev. B*, **44**, 705, (1991).

[78] I. Avenel *et al.*. *Phys. Rev. B*, **46**, 8655, (1992).

[79] K. Katsumata, H. Hori, T. Takeuchi, M. Date, A. Yamagishi, and J. P. Renard. *Phys. Rev. Lett.*, **63**, 86, (1989).

[80] Y. Ajiro, T. Goto, H. Kikuchi, T. Sakakibara, and T. Inami. *Phys. Rev. Lett.*, **63**, 1424, (1989).

[81] S. Ma, C. Broholm, D. H. Reich, B. J. Sternlieb, and R. W. Erwin. *Phys. Rev. B*, **69**, 3571, (1992).

[82] L. P. Regnault, I. Zaliznyak, J. P. Renard, and C. Vettier. *Phys. Rev. B*, **50**, 9174, (1994).

[83] S. Ma, D. H. Reich, C. Broholm, B. J. Sternlieb, and R. W. Erwin. *Phys. Rev. B*, **51**, 3289, (1995).

[84] M. Chiba, Y. Ajiro, H. Kikuchi, T. Kubo, and T. Morimoto. *Phys. Rev. B*, **44**, 2838, (1991).

[85] P. Geveau, J. P. Boucher, L. P. Regnault, T. Goto, and J. P. Renard. *J. Appl. Phys.*, **69**, 5956, (1991).

[86] N. Fujiwara, T. Goto, S. Maegawa, and T. Kohmoto. *Phys. Rev. B*, **45**, 7837, (1992).

[87] N Fujiwara, T. Goto, S. Maegawa, and T. Kohmoto. *Phys. Rev. B*, **47**, 11860, (1993).

[88] N. Fujiwara. *Kotai butsuri* (in Japanese), **30**, 755, (1995).

[89] M. Hagiwara, K. Katsumata, Ian Affleck, B. I. Halperin, and J. P. Renard. *Phys. Rev. Lett.*, **65**, 3181, (1990).

[90] S. H. Glarum, S. Geschwind, K. M. Lee, M. L. Kaplan, and J. Michel. *Phys. Rev. Lett.*, **67**, 1614, (1991).

[91] M. Date and K. Kindo. *Phys. Rev. Lett.*, **65**, 1659, (1990).

[92] W. Lu, J. Tuchendler, M. von Ortenberg, and J. P. Renard. *Phys. Rev. Lett.*, **67**, 3716, (1991).

[93] L. C. Brunel, T. Brill, I. Zaliznyak, J. P. Boucher, and J. P. Renard. *Phys. Rev. B*, **69**, 1699, (1992).

[94] B. J. Sternlieb *et al.*. *J. Mag. Mag. Matrs.*, **104-107**, 801, (1992).

[95] Y. J. Uemura *et al.*. *Hyperfine Interactions*, **85**, 133, (1994).

[96] Y. J. Uemura *et al.*, unpublished work.

[97] D. J. Buttrey, J. D. Sullivan, and A. L. Rheingold. *J. Solid. State Chem.*, **88**, 291, (1990).

[98] R. Saez-Ruche *et al.*. *J. Solid State Chem.*, **93**, 461, (1991).

[99] B. Batlogg *et al.*. *Physica*, **B194-196**, 173, (1994).

[100] S-W. Cheong, A. S. Cooper, L. W. Rupp, Jr., and B. Batlogg. *Bull. Am. Phys. Soc.*, **37**, 116, (1992).

[101] J. Darriet and L. P. Regnault. *Solid State Commun.*, **86**, 409, (1993).

[102] J. F. DiTusa *et al.*. *Physica*, **B194-196**, 181, (1994).

[103] J. F. DiTusa, G. Aeppli S-W. Cheong, J.-H. Park, C. Broholm, and C. T. Chen. *Phys. Rev. Lett.*, **73**, 1857, (1994).

[104] A. P. Ramirez, S-W. Cheong, and M. L. Kaplan. *Phys. Rev. Lett.*, **72**, 3108, (1994).

[105] N. Arikawa and K. Kiyono. Master's thesis, Univ. of Tokyo, (1993).

[106] Y. J. Uemura, A. Keren, K. Kojima, L. P. Le, G. M. Luke, W. D. Wu, Y. Ajiro, T. Asano, Y. Kuriyama, M. Mekata, H. Kikuchi, and K. Kakurai. *Phys. Rev. Lett.*, **73**, 3306, (1994).

[107] A. P. Ramirez, G. P. Espinosa, and A. S. Cooper. *Phys. Rev. Lett.*, **64**, 2070, (1990).

[108] A. P. Ramirez, G. P. Espinosa, and A. S. Cooper. *Phys. Rev. B*, **45**, 2505, (1992).

[109] B. Martínez, F. Sandiumenge, A. Rouco, A. Labarta, J. Rodriguez-Carvajal, M. Tovar, M. T. Causa, S. Gali, and X. Obradors. *Phys. Rev. B*, **46**, 10786, (1992).

[110] A. Keren *et al.*. *Hyperfine Interactions*, **85**, 181, (1994).

[111] C. Broholm, G. Aeppli, G. P. Espnosa, and A. S. Cooper. *Phys. Rev. Lett.*, **65**, 3173, (1990).

[112] P. W. Leung and V.Elser. *Phys. Rev. B*, **47**, 5459, (1993).

[113] C. Boekema. *Hyperfine Interaction*, **8**, 609, (1981).

[114] W. A. Dawson *et al.*. *J. Appl. Phys.*, **64**, 5809, (1988).

[115] C. Boekema *et al.*. *J. Mag. Mag. Matrs.*, **36**, 111, (1983).

[116] C. Boekema. *Hyperfine Interaction*, **17**, 305, (1984).

[117] E. Holzschuh *et al.*. *Phys. Rev. B*, **27**, 5294, (1983).

[118] P. Jordan and E. P. Wigner. *Z. Phys.*, **47**, 631, (1928).

[119] L. N. Bulaevskii. *Sov. Phys.-JETP*, **17**, 684, (1963).

[120] E. Pytte. *Phys. Rev. B*, **10**, 4637, (1974).

[121] M. C. Cross and D. S. Fisher. *Phys. Rev. B*, **19**, 402, (1979).

[122] S. Tomonaga. *Prog. Theor.Phys.*, **5**, 342, (1950).

[123] J. M. Luttinger. *J. Math. Phys.*, **4**, 1154, (1963).

[124] A. Luther and I. Peschel. *Phys. Rev. B*, **12**, 3908, (1975).

[125] T. Nakano and H. Fukuyama. *J. Phys. Soc. Jpn.*, **49**, 1679, (1980).

[126] T. Nakano and H. Fukuyama. *J. Phys. Soc. Jpn.*, **50**, 2489, (1981).

[127] J. W. Bray, H. R. Hart, Jr., L. V. Interrante, I. S. Jacobs, J. S. Kasper, G. D. Watkins, S. H. Wei, and J. C. Bonner. *Phys. Rev. Lett.*, **35**, 744, (1975).

[128] I. S. Jacobs, J. W. Bray, H. R. Hart, Jr., L. V. Interrante, J. S. Kasper, G. D. Watkins, D. E. Prober, and J. C. Bonner. *Phys. Rev. B*, **14**, 3036, (1976).

[129] S. Huizinga, J. Kommandeur, G. A. Sawatzky, B. T. Thole, K. Kopinga, W. J. M. de Jonge, and J. Roos. *Phys. Rev. B*, **19**, 4723, (1979).

[130] D. E. Moncton, R. J. Birgeneau, L. V. Interrante, and F. Wudl. *Phys. Rev. Lett.*, **39**, 507, (1977).

[131] B. van Bodegom, B. C. Larsen, and H. A. Mook. *Phys. Rev. B*, **24**, 1520, (1981).

[132] L. N. Bulaevskii. A. I. Buzdin, and D. I. Khomskii. *Solid State Commun.*, **27**, 5, (1978).

[133] J. W. Bray, L. V. Interrante, I. S. Jacobs, D. Bloch, D. E. Moncton, G. Shirane, and J. C. Bonner. *Phys. Rev. B*, **20**, 2067, (1979).

[134] D. Bloch, J. Voiron, J. C. Bonner, J. W. Bray, I. S. Jacobs, and L. V. Interrante. *Phys. Rev. Lett.*, **44**, 294, (1980).

[135] J. A. Northby, H. A. Groenendijk, L. J. de Jongh, and J. C. Bonner. *Phys. Rev. B*, **25**, 3215, (1982).

[136] T. W. Hijmans, H. B. Brom, and L. J. de Jongh. *Phys. Rev. Lett.*, **54**, 1714, (1985).

[137] T. W. Hijmans and W. P. Beyermann. *Phys. Rev. Lett.*, **58**, 2351, (1987).

[138] V. Kiryukhin, B. Keimer, and D. E. Moncton. *Phys. Rev. Lett.*, **74**, 1669, (1995).

[139] M. Hase, I. Terasaki, K. Uchinokura, M. Tokunaga, N. Miura, and H. Obara. *Phys. Rev. B*, **48**, 9616, (1993).

[140] M. C. Cross. *Phys. Rev. B*, **20**, 4606, (1979).

[141] M. Hase, I. Terasaki, and K. Uchinokura. *Phys. Rev. Lett.*, **70**, 3651, (1993).

[142] H. Völlenkle, A. Wittmann, and H. Nowotny. *Monatsh. Chem.*, **98**, 1352, (1967).

[143] M. Nishi, O. Fujita, and J. Akimitsu. *Phys. Rev. B*, **50**, 6508, (1994).

[144] I. Terasaki, R. Itti, N. Koshizuka, M. Hase, I. Tsukada, and K. Uchinokura. *Phys. Rev. B*, **52**, 295, (1995).

[145] O. Kamimura, M. Terauchi, M. Tanaka, O. Fujita, and J. Akimitsu. *J. Phys. Soc. Jpn.*, **63**, 2467, (1994).

[146] J. P. Pouget, L. P. Regnault, M. Ain, B. Hennion, J. P. Renard, P. Vellet, G. Dhalenne, and A. Revcolevschi. *Phys. Rev. Lett.*, **72**, 4037, (1994).

[147] K. Hirota, D. E. Cox, J. E. Lorenzo, G. Shirane, J. M. Tranquada anmd M. Hase, K. Uchinokura, H. Kojima, Y. Shibuya, and I. Tanaka. *Phys. Rev. Lett.*, **73**, 736, (1994).

[148] M. Poirier, M. Castonguay, A. Revcolevschi, and G. Dhalenne. *Phys. Rev. B*, **51**, 6147, (1995).

[149] J. E. Lorenzo, K. Hirota, G. Shirane, J. M. Tranquada, M. Hase, K. Uchinokura, H. Kojima, I. Tanaka, and Y. Shibuya. *Phys. Rev. B*, **50**, 1278, (1994).

[150] Q. J. Harris, Q. Feng, R. J. Birgeneau, K. Hirota, K. Kakurai, J. E. Lorenzo, G. Shirane, M. Hase, K. Uchinokura, H. Kojima, I. Tanaka, and Y. Shibuya. *Phys. Rev. B*, **50**, 12606, (1994).

[151] M. Nishi, O. Fujita, J. Akimitsu, K. Kakurai, and Y. Fujii. *Phys. Rev. B*, **52**, R6959, (1995).

[152] C. H. Chen and S-W.Cheong. *Phys. Rev. B*, **51**, 6777, (1995).

[153] V. Kiryukhin and B. Keimer. *Phys. Rev. B*, **52**, R704, (1995).

[154] O. Fujita, J. Akimitsu, M. Nishi, and K. Kakurai. *Phys. Rev. Lett.*, **74**, 1677, (1995).

[155] S. Oseroff, S-W. Cheong, A. Fondado, B. Aktas, and Z. Fisk. *J. Appl. Phys.*, **75**, 6819, (1994).

[156] T. M. Brill, J. P. Boucher, J. Voiron, G. Dhalenne, A. Revcolevschi, and J. P. Renard. *Phys. Rev. Lett.*, **73**, 1545, (1994).

[157] M. Itoh, S. Hirashima, and K. Motoya. *Phys. Rev. B*, **52**, 3410, (1995).

[158] M. Hase, I. Terasaki, Y. Sasago, K. Uchinokura, and H. Obara. *Phys. Rev. Lett.*, **71**, 4059, (1993).

[159] S. B. Oseroff, S-W. Cheong, B. Aktas, M. F. Hundley, Z. Fisk, and L. W. Rupp, Jr. *Phys. Rev. Lett.*, **74**, 1450, (1995).

[160] L. E. Wenger and P. H. Keesom. *Phys. Rev. B*, **13**, 4053, (1976).

[161] M. Hase, K. Uchinokura, R. J. Birgeneau, K. Hirota, and G. Shirane. preprint, (1995). submitted to J. Phys. Soc. Jpn..

[162] M. T. Hutchings, E. J. Samuelsen, G. Shirane, and K. Hirakawa. *Phys. Rev.*, **188**, 919, (1969).

[163] J.-P. Renard, K. Le Dang, P. Vellet, G. Dhalenne, A. Revcolevschi, and L.-P. Regnault. *Europhys. Lett.*, **30**, 475, (1995).

[164] M. Poirier, R. Beaudry, M. Castonguay, M. L. Plumer, G. Quirion, F. S. Razavi, A. Revcolevschi, and G. Dhalenne. *Phys. Rev. B*, **52**, R6971, (1995).

[165] O. Tchernyshyov *et al.*. *J. Mag. Mag. Matrs.*, **140-144**, 1687, (1995).

[166] J. L. García-Muñoz, M. Suaaidi, and B. Martínez. *Phys. Rev. B*, **52**, 4288, (1995).

[167] M. Hase, Y. Sasago, I. Terasaki, K. Uchinokura, G. Kido, and T. Hamamoto. preprint, (1995). submitted to J. Phys. Soc. Jpn..

共同研究者構成表

主論文第4－6章：　植村 泰朋 教授（米国コロンビア大学 物理学科）
G. M. Luke 助教授（同上）
植村研究室大学院生　A. Keren　（当時）
M. Larkin
L. P. Le　（当時）
J. Merrin
B. Nachumi
W. D. Wu　（当時）

主論文第4章：　高野 幹夫 教授（京都大学 化学研究所）
（スピン梯子系）　高野研究室大学院生　東　正樹　（当時）

主論文第5章：　内田 慎一 教授（東京大学 工学系大学院）
（ハルデン系）　高木 英典 講師（同上；当時）
内田研究室大学院生　清野 賢二郎　（当時）
宮坂 茂樹　（当時）

主論文第6章：　内野倉國光 教授（東京大学 工学部応用物理学科）
（スピンパイエルス系）　内野倉研究室大学院生　長谷 正司（当時）
笹子 佳孝